Summer 2014

Local liquid velocity measurement of trickle bed reactor using digitial industrial X-ray radiography

Khairul Anuar Mohd Salleh

Department: Nuclear Engineering and Radiation Science

LOCAL LIQUID VELOCITY MEASUREMENT OF TRICKLE BED REACTOR USING DIGITAL INDUSTRIAL X-RAY RADIOGRAPHY

by

KHAIRUL ANUAR MOHD SALLEH

A DISSERTATION

Presented to the Faculty of the Graduate School of the

MISSOURI UNIVERSITY OF SCIENCE AND TECHNOLOGY

In Partial Fulfillment of the Requirements for the Degree

DOCTOR OF PHILOSOPHY

in

NUCLEAR ENGINEERING

2014

Approved by
Dr. Hyoung Koo Lee, Co-Advisor
Dr. Muthanna Al-Dahhan, Co-Advisor
Dr. Carlos H. Castano
Dr. Randy H. Moss
Dr. Xin Liu

ABSTRACT

Trickle Bed Reactors (TBRs) are fixed beds of particles in which both liquid and gas flow concurrently downward. They are widely used to produce not only fuels but also lubrication products. The measurement and the knowledge of local liquid velocities (V_{LL}) in TBRs is less which is essential for advancing the understanding of its hydrodynamics and for validation computational fluid dynamics (CFD). Therefore, this work focused on developing a new, non-invasive, statistically reliable technique that can be used to measure local liquid velocity (V_{LL}) in two-dimensions (2-D). This is performed by combining Digital Industrial X-ray Radiography (DIR) and Particle Tracking Velocimetry (PTV) techniques. This work also make possible the development of three-dimensional (3-D) V_{LL} measurements that can be taken in TBRs. Measurements taken through both the combined and the novel technique, once validated, were found to be comparable to another technique (a two-point fiber optical probe) currently being developed at Missouri University of Science and Technology. The results from this study indicate that, for a gas-liquid-solid type bed, the measured V_{LL} can have a maximum range that is between 35 and 51 times that of its superficial liquid velocity (V_{SL}). Without the existence of gas, the measured V_{LL} can have a maximum range that is between 4 and 4.7 times that of its $V_{SL.}$ At a higher V_{SL}, the particle tracer was greatly distributed and became carried away by a high liquid flow rate. Neither the variance nor the range of measured V_{LL} varied for any of the replications, confirming the reproducibility of the experimental measurements used, regardless of the $V_{SL.}$ The liquid's movement inside the pore was consistent with findings from previous studies that used various techniques.

ACKNOWLEDGMENTS

In the name of Allah, the most merciful and beneficial

PhD is indeed a very lonely business, laborious yet interesting work. I have faced the disappointment and the happiness through the journey and never expect to be this far. It requires never ending prayer, hope, time, space, generous ideas, fruitful discussions, and hard work. There are a number of people I would like to thank for supporting me throughout this work. First and foremost, I must thank my advisers, Dr. Hank Lee and Dr. Muthanna Al-Dahhan, for their wonderful mentorship. I am particularly thankful for Dr. Muthanna Al-Dahhan's financial support throughout the experimental work. I am also quite grateful to the Malaysian Nuclear Agency and Malaysian Ministry Of Science, Technology and Innovation (MOSTI). I wish to thank Dr. Abd. Nassir Ibrahim, Dr. Ab. Razak Hamzah, and the rest of Non-Destructive Testing (NDT) group of Malaysian Nuclear Agency for their encouragement. I am greatly appreciative of the time Jason Hagerty spent, helping me develop my algorithm. I also extend my gratitude to Dean Lenz for helping me design, build, and install my setup. I would like to thank Bill Bonzer, Craig Reisner, and Raymond Kendrick for their invaluable time, patience, and kind assistance. I must also thank Greg Castor, the Regional Manager of Foam Fabricators, Inc., El Dorado Springs, Missouri, for providing the study with free EPS beads. Thank you to members of both the Nuclear Engineering and the Chemical Engineering departments for the coffee, encouragement, and brilliant ideas. Thank you Dr. Randy Moss, Dr. Xin Liu, and Dr. Carlos H. Castano for your willingness to be part of my doctoral advisory committee. I am thankful for the prayers and support offered by my Father, Mohd Salleh b. Kassim. I am also thankful for my mother, Allahyarham Kasmah binti Abdullah: if you could see me now, I know you would be so proud. This journey was begun by my sisters and brothers; they paved the way for my success. Most of all, however, I would like to thank my wife, Suhaini Hamdan, for her prayers, love, persistence, support, for all the late nights, long days, and my indistinct thought. I could not have completed this work without you. To my growing kids, Muhammad Irfan Amzar, Muhammad Amru Hakim and Aish Sophia: I hope that our short stay here will benefit all of you. Thank you all.

TABLE OF CONTENTS

LIST OF ILLUSTRATIONS

LIST OF TABLES

NOMENCLATURE

Symbol	Description
$\vec{\nabla} I_k$	Gradient of the intensity calculated from the image at the midpoints between the pixels' centers
$\mathrm{Con}_{\mathrm{subj}}$	Subject contrast
L_{meas}	Measured length of the streamline
L_{ε}	Actual length of the streamline
V_G	Gas velocity
V_L	Liquid velocity
$d_{k,c}$	Distance (d_c) between (x_k, y_k)
ε_{β}	TBR packing porosity
Δt	Time difference
A	Cross sectional area of the reactor
A	Pixel matrices
A-Se	Amorphous selenium
A-Si	Amorphous silicon
B	Pixel matrices
BG(x,y)	Background image represented by Cartesian coordinate
CdTe	Cadmium telluride
D	Diameter
D	Duplex
df	Degree of freedom
e(x)	Edge spread function
eV	Electron volts
F	Focal spot size
f(x,y)	Sample image to be analyzed
h(x,y)	Template image
H_a	Alternative hypothesis
H_o	Null hypothesis
I	Image

$I(x,y)$	Image represented by Cartesian coordinate
$I(x_c,y_c)$	Image center
I_{BG}	Background image
I_{diff}	Image difference
I_t	Image at certain time
$l(x)$	Line spread function
lp/mm	Line pair per millimeter
M	Image size
$MTF_{20\%}$	Transfer function at 20% modulation
N	Image size
N	Noise
O	Object scene
P_R	Calibrated profile
p_r	Probability density function with random variable r
p-value	Probability value
Q	Volumetric flow rate
R	Cross-correlation coefficient
R	Particle radius
Re	Reynolds number
Re_G	Gas's Reynolds number
Re_L	Liquid's Reynolds number
r_n	Pixel level
s_n	histogram stretching
T	Threshold operation
t-test	Student t-test
U_1	Liquid phase
U_2	Gas phase
V_{LL}	Local liquid velocity
$V_{LL\|DIR}$	Local liquid velocity obtained using DIR and PTV technique
$V_{LL\|OPT}$	Local liquid velocity obtained using fiber optic technique
$V_{LL\text{-}Max}$	Maximum local liquid velocity

V_{ML}	Macroscopic interstitial velocity
V_{SG}	Superficial gas velocity
V_{SL}	Superficial liquid velocity
V_{τ}	Velocity based on length calculated from tortuosity value
Z	Atomic numbers
Z	Height
Z/D	Height over diameter ratio
D	Tube diameter
H	Bed height
d	Packing diameter
$g(x,y)$	Threshold image
k	Image lattice midpoint

Greek letters

$I_{\circ}$	Initial intensity
Δ	Difference
∈	Consist of
Å	Angstrom
t	Time
α	Volumetric gas holdup
γ	Gamma-ray
λ	Wavelength
μ	Micro
σ	Standard deviation
Σ	Summation of product
σ^2	Variance
I	Intensity
e	Exponential
x	Thickness
ε	Porosity
θ	Angle of flow path

μ	Absorption coefficients
π	Pi
ρ	Material density
τ	Tortuosity

Subscripts

$_\circ$	Initial or Null
a	Alternative
Diff	Difference
G	Gas
L	Liquid
LL	Local liquid
Min	Minimum
ML	Interstitial macroscopic liquid
SG	Superficial gas
SL	Superficial liquid
Subj	Subject

Abbreviations

2-D	Two dimensional
3-D	Three dimensional
Al_2O_3	Alumina microspheres
CAT	Computer-assisted tomography
CCD	Chip coupled device
CFD	Computational fluid dynamics
CMOS	Complementary metal oxide semiconductor
CR	Computed radiography
CT	Computed tomography
DAQ	Data acquisition
DIR	Digital industrial radiography

DQE	Detective quantum efficiency
EN	European Norm (standard)
EPS	Expanded polystyrene
FPS	Frames per second
H_2O	Liquid – water
IP	Imaging plate
IQI	Image quality indicator
LDV	Laser Doppler Velocimetry
LED	Laser emitting diode
MRI	Magnetic resonance imaging
MSTR	Missouri University of Science & Technology Reactor
MTF	Modulation transfer function
NDT	Non-destructive testing
NIST	National Institute of Standards and Technology
NPS	Noise power spectrum
NPW	Non-pre-wetted
ODD	Object detector distance
OPT	Optical probe technique
PIDV	Particle image displacement velocimetry
PIV	Particle image velocimetry
PMMA	Polymethyl methacrylate
PSF	Point spread function
PTV	Particle tacking velocimetry
PVC	Polyvinyl chloride
RT	Radiography technique
SDD	Source to detector distance
T_{test}	Test tube
TBRs	Trickle bed reactors
WMSs	Wire measure sensors

1. INTRODUCTION

1.1. TRICKLE BED REACTORS (TBRs)

Trickle bed reactors (TBRs), widely known as gas-solid-liquid-type reactors, are fixed beds of particles in which liquid and gas flow concurrently downward. As they move, they contact and react with not only fixed but also structurally randomized solid particles that act as catalysts. TBRs were used to treat organic matters in wastewater streams (Satterfield, 1975). It is one type at multiphase flow systems. They are now widely used to produce not only low-sulfur fuel oils but also fuels and lube products intended for use in extremely cold conditions. They are used for production of high-quality middle-distillate fuels, lubricating oils, and more (Dudukovic, et al., 1999). Industries often use these reactors when the catalyst's activity can be maintained over a long period of time (Dudukovic, 2000). Figure 1.1 illustrates a typical TBR design.

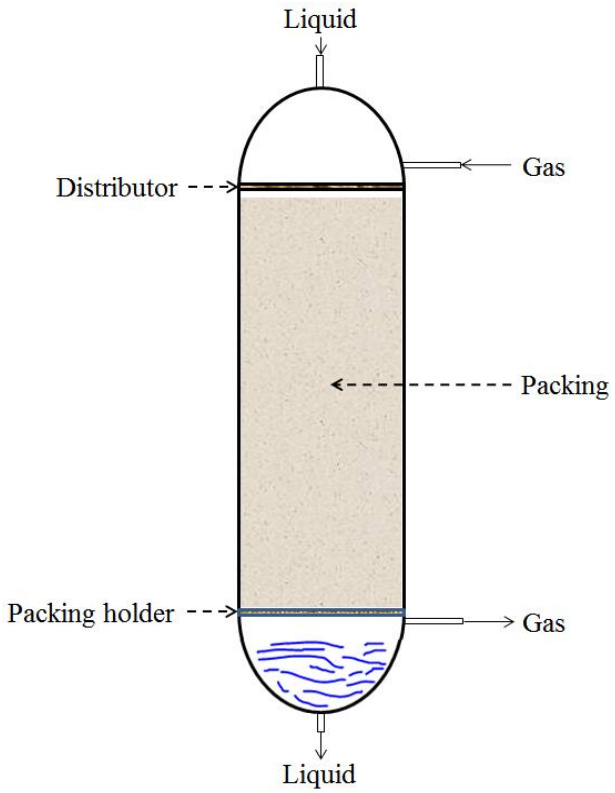

Figure 1.1. Schematic of a trickle bed reactor (TBR) (Al-Dahhan, 1993)

TBRs have a free-volume fraction among the packing (known as porosity) that allows liquid to flow freely between particles. The packing material exists in spherical, cylindrical lumps of irregularly shaped extrudes and granules between 0.1 cm and 3.2 cm (Al-Dahhan, 1993). Compared to other type of reactor, TBRs offer a number of advantages (e.g. they can easily be constructed and are close to plug flow condition). Unfortunately, TBRs present a number of significant drawbacks, such as liquid velocity maldistribution, channeling, and incomplete catalyst wetting (Sie & Krishna, 1998). These drawbacks will in turn affect reactor performance

Table 1.1 lists both the advantages and disadvantages of utilizing TBRs. Low reactor performance represents substantial losses which degrade the quality of the product and burden the consumer.

The TBRs are often designed based on the prediction of specific performance. Two main factors affect this performance: macro scale and micro scale. Macro scale involves the number of complex phenomena that can be observed on a reactor scale. Micro-scale performance can be observed in particle scale.

Table 1.1. Both the advantages and disadvantages of utilizing TBRs

Advantages	Disadvantages
- Liquid flow closed to plug flow - Catalyst / packing are static - Operable at higher temperatures and pressures - Low operating cost and investment - No high power requirement. - Flexible operation	- Maldistribution in liquid velocities - Incomplete catalyst wetting and channeling - Laboratory- to-industrial scaling up process is difficult - Limited to non-viscous fluid - Low reaction rate due to a large catalyst size

The reactor operates in a very specific regime that is determined, primarily by the superficial velocities of gas and liquid, physical properties of liquid and gas phases, and bed characteristics. Distinguishable regimes include trickle flow (continuous gas), pulse flow (partly continuous gas and liquid), dispersed bubble flow (continuous liquid), and spray flow (continuous gas and highly dispersed liquid) (Sie & Krishna, 1998). Each boundary of flow regime is illustrated in Figure 1.2 (a) and (b).

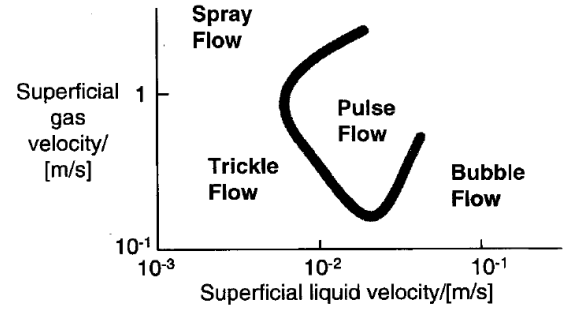

(a)

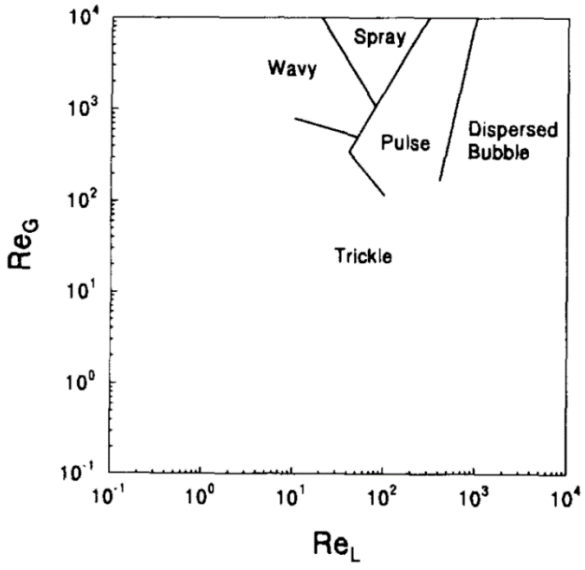

(b)

Figure 1.2. Co-current downward flow regimes: (a) in terms of velocities (Sie & Krishna, 1998) and (b) in terms of Reynolds number (Adapted from Al-Dahhan & Dudukovic (1995))

TBR performance is often dictated by its hydrodynamic states, such as flow distribution, liquid and gas holdup, liquid velocities, and pressure drop. Although a great deal of research has focused on this performance (Merwe, et al., 2007; Boyer & Fanget, 2002; Yamada, et al., 1999; Al-Dahhan, et al., 1997; Schurbet, et al., 2008; Sederman & Gladden, 2001; Chaouki, et al., 1997), the actual condition occurring inside TBRs is still not clearly understood.

Both the formation of hot spots and the reactor performance at different hydrodynamic states as the cause of decreasing reactor productivity have been most frequently studied (Germain, et al., 1974; Jaffe, 1976; Al-Dahhan, 1993; Al-Naimi, et al., 2011). Such studies reveal that the interaction between all three phases (solid-liquid-gas) is difficult to analyze due to the complexities and non-uniform parameters of the packing (e.g., structure, size, shape, and method used).

A better understanding of both the liquid and the gas phases flow conditions in TBRs is key to controlling the throughput's system. This knowledge would allow the transport processes to be quantified, thus allowing overall reactor performance to be enhanced. Understanding the flow conditions helps understanding the transport of heat and mass transfer in TBRs.

Previous studies that include both theoretical and experimental data often treat such TBR system as homogeneous in terms of pore structure and size. This data leads to a misinterpretation of the actual reactor's performance, often ignoring pore complexity while providing only global hydrodynamic values of the flow field. Because both pore structure and size are totally random, flow fields are becoming completely different throughout reactor beds, which the later necessitate of measuring more localized parameters of the reactor.

A study of flow fields requires knowledge of local liquid velocities and hence their measurements. Schubert et al. (2010) suggested that such a measurement technique in a packed bed is still rare, typically existing in one of two ways: either intrusive or non-intrusive.

Intrusive techniques were developed in the early 1960s to measure the local liquid velocity. Unfortunately, most were both expensive and cumbersome (Boyer & Fanget, 2002). One intrusive technique involves using thermal anemometry that was

initially designed to study heat transfer. This technique provides a radial profile of the heat transfer coefficient, indicating liquid velocity at the microscopic level (Marcandelli, et al., 1999). Such an intrusive technique introduces only a point-type measurement limiting information that can be gathered on the entire reactor (Seeger, et al., 2003).

Recently applied intrusive-type measurement techniques utilize both wire mesh sensors (WMSs) (Schubert, et al., 2010) and optical probes. Two-plane sensors made of 16 stainless steel wires (0.2 mm diameter) are installed inside the bed. One of the planes is setup at a known distance on top of the other. The WMSs require a conductive tracer to be injected while the liquid is trickling inside the bed.

Two distinct conductivity values provide different readings (the time of flow for the liquid). Wangjiraniran et al. (2003) studied the intrusive effect on gas–liquid flow, determining that such planes not only deformed but also disturbed the movement of the flow. They concluded that the accuracy of the measurement was due to the intrusive feature that can be approximately identified from the setup itself. As a result, intrusive methods are not the technique of choice when performing the liquid velocity measurement.

1.2. MOTIVATION

A number of studies have attempted to obtain local liquid velocity measurements (V_{LL}) non-intrusively from TBRs and packed beds. The following problems however limit these experiments:

- Front side packing will block the view of any movement occurring behind it (limiting the optical access) in a two-dimensional technique;
- Most TBRs operate effectively when they are opaque (inaccessible to light).

Currently, few techniques to measure V_{LL} and map the liquid flow inside TBRs. This V_{LL} measurement is difficult to perform because it is imperceptible to most instrumentation (Cushman & Moroni, 2001). These measurements are characterized into two major methods: optical and radiation.

1.2.1. Optical Method for V_{LL} Measurement. Laser doppler velocimetry (LDV) is one of the earliest techniques successfully used to measure interstitial velocity within both a packed bed and other mixed phase systems (Northrup, et al., 1993). LDV was introduced and utilized by Johnston and Dybbs (1975) to study the flow process and velocity field inside a bed packed with 1.27 cm diameter Plexiglas spheres. This technique is non-intrusive, producing high resolution result. Unfortunately, LDV has one major disadvantage: it provides only a point velocity measurement.

Thus, it is considered a time-consuming velocity measurement technique. It is unable to record either velocity field temporal or spatial variations. Another technique developed to study interstitial velocity fields and display streamlines in packed beds is particle image displacement velocimetry (PIDV). PIDV, which originated from particle image velocimetry (PIV), is an optical method used to measure fluid velocity by identifying the position over time of small particles introduced to a flow. It represents a quantitative extension of the qualitative flow visualization techniques that have been practiced for several decades (Prasad, 2000). With PIV, quantitative information is extracted from visualized flow images; digital image processing techniques are used for analysis (Lee & Kim, 2003). PIV enables the identification of individual particle images within a higher density of particles. Saleh et al. (1992) applied PIDV to 10 mm Plexiglas beads. Here, the interstitial flow that contained tracers (4 μm aluminum particles) was illuminated with a planar light sheet. Multiple-exposures of corresponding particles point in series were recorded (photographically). The performed measurements were between 25 μm/s and 2.5 mm/s. This technique, however suffered from background noise, producing poor quality data (Saleh, et al., 1992). Northrup et al. (1993) successfully established a better technique by combining particle image velocimetry (PIV) with a refracting index matching technique. They successfully removed the noise to obtain a better resolution. With this improved resolution, Northrup et al. (1993) had more streamlines and vectors.

Particle tacking velocimetry (PTV) is commonly used to observe individual particles within a low number of particle images (low seeding density). Investigators use this method to track these particles and it is the most suitable measurement technique if less number of particles are flowing with liquid (Theunissen, 2003).

Figure 1.3 illustrates the difference between PIV and PTV. In a packed bed, PTV is used to characterize both the velocity distribution and its spatial averaging properties in a full 3-D volume (Peurrung, et al., 1995), a mixture of silicone oil with 6.5 μm fluorescent latex microspheres is used as the liquid and tracing particles. Both bed and the packing were made of Polymethyl methacrylate (PMMA) with 4.5 cm inner diameter and 3.1 mm diameter.

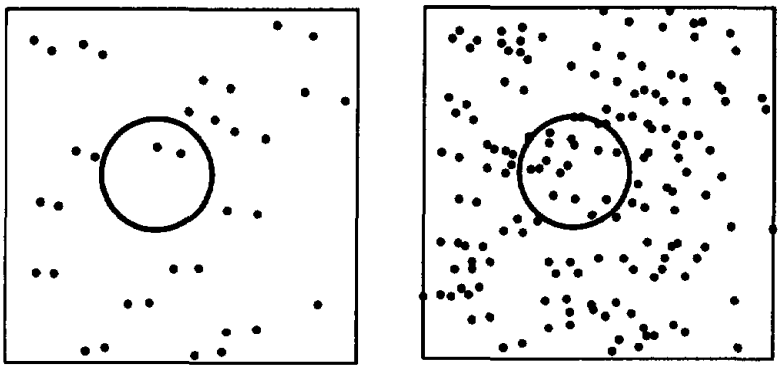

(a) (b)

Figure 1.3. Comparison between (a) particle tracking velocimetry (PTV) and (b) particle image velocimetry (PIV). The circle indicates an interrogation area (Westerweel, 1993)

Peurrung et al. (1995) tracked the individual particles by recording them with a video camera. By applying 3D-PTV, Moroni & Cushman (2001) used two cameras on 1.9 cm Pyrex spherical packing inside a Perspex parallelepiped tank. Two component velocities for packed beds were also studied to characterize pore scale velocity with a single camera (Huang, et al., 2008). Both Moroni & Cushman (2001) and Huang et al. (2008) used statistical base analysis to obtain particle trajectories for velocity components. Seeger et al. (2003) reported that PIV and PTV can only be applied for small solid hold-ups, non-opaque systems and small void fractions. Common corresponding problems do exist between PIV and PTV. These problems typically occur when uneven tracking particles (both non-spherical and non-uniform) are used. Tapia et al. (2006) overcame the problem of physical property difference; Parthasarathy

(2012) introduced the algorithm that has an accuracy of an expected limit for such problem.

1.2.2. Radiation Method in Multiphase Flow Study. Combination of radiography techniques (RT) with X-ray for hydrodynamic study in multiphase flow started in 1950s (Heindel, 2011). This technique made possible live and still visualization as well as quantifiable output without disturbing the ongoing process. The seeded particle absorbs the X-ray radiation which gives intensity difference on the final image.

RT is used in industry to detect sub-surface and internal defects produced from welding, structures, and the discontinuities of processes (Halmshaw, 1991). It is a process of non-destructive testing (NDT) that uses penetrating ionizing radiation (either X-ray or gamma ray) that pass through an object. The image itself is permanently captured by either imaging media or a detector through intensity differences. Several studies using X-ray technology have been conducted on both the fluid dynamic and the multiphase flow of TBRs. Lutran et al. (1991) used X-ray computer-assisted tomography (CAT) for a liquid-solid bed system to not only visualize but also characterize the effect of pre-wetting (non-pre-wetted (NPW) and Kan-Liq) on a liquid-solid system. These pre-wetting techniques, experimentally performed on 6 mm and 3 mm glass beads, determined the effect flow surrounding the packing. The pre-wetting condition pattern creates flows that dominate the bed; NPW will create a filament flow while the Kan-Liq will create film flow (Lutran, et al., 1991). Both X and gamma (γ) ray computed tomography (CT) were also used to study liquid hold-up inside 4.5 cm x 45 cm and 60 cm x 60 cm (diameter x height) trickle beds with glass sphere packing (Kantzas, 1994) and stainless steel Pall rings (Yin, et al., 2002). These liquid hold-up studies are essential because they suggest an effective way to design the liquid distributor and reveal the liquid distribution. Boyer & Fanget (2002) used a γ-ray tomographic system to detect the flow mal-distribution inside a 60 cm diameter bed. The size of the bed, strong attenuation of catalyst, and the liquid made it difficult for the ionization to pass through. Seeger et al. (2001) successfully assessed the 3D velocity of a bubble column's liquid phase using an X-ray-based PTV method. The X-ray tube used was a medical grade system typically used for the flow visualization of human blood

vessels. Particles used were comprised of a lead alloy (2mm length and 0.5mm diameter). The particles were meant to give good X-ray image contrast and were covered with polyurethane foam (2 x 2 x 2 mm^3) for buoyancy purpose. Merwe et al. (2007) also used this technique in trickle bed reactor (catalytic gas-liquid-solid) to not only visualize but also characterize trickle flow in several hydrodynamic states. Lee & Kim (2003) used third generation synchrotron radiation sources to measure the velocity of alumina microspheres (Al_2O_3) with a mean diameter of 3 μm (0.003 mm) inside an opaque tube. The density of the Al_2O_3 was 3.965 g/cm^3. It was injected into a microtube (750μm inner diameter) with a syringe pump at a mean velocity of 0.5 mm/s. Lee & Kim (2003) used glycerin (1.260 g/cm^3) for the working fluid. They also used a mechanical shutter to generate double X-ray pulses for PIV velocity field measurements. Lee et al. (2009) made the tube larger (4mm), and combined the PIV with a medical grade X-ray tube. They also improved the shutter system to capture a better image. The shutter allowed a single X-ray tube to capture both multiple and consecutive 2D X-ray images. From the experiment, they came out with the velocity profile of the travelling liquid.

Nuclear magnetic resonance imaging (MRI) is another non-intrusive flow measurement technique used to study the packed bed. Such a technique is based on the paramagnetic properties of the nuclei (Chaouki, et al., 1997); was successfully used to view liquid flow, measure liquid velocity, understand gas-liquid distribution, study the flow phenomena structure, and investigate the pore's structure (Schubert, et al., 2010; Sankey, et al., 2009; Elkins & Alley, 2007; Sederman & Gladden, 2001). Although MRIs are known to produce accurate results, they are expensive for regular use (Delgado, 2006), and many predict they will not be applicable as an industrial practice in the near future (Boyer & Fanget, 2002; Schubert, et al., 2010). The primary advantages, summarized in Table 1.2, of the radiation method in a multiphase flow include the following (Lee & Kim, 2003; Kertzscher, et al., 2004):

- Allows for the gathering of quantitative information on the entire flow field of flows enclosed by opaque materials
- Exhibits no issues with either reflection or refraction at the phase boundaries

Table 1.2. Summary of V_{LL} measurement using radiation method in other type reactor

Type of Radiation	Type of reactor	Objective	References
X-ray	Liquid-Solid Bed System	Visualization of wetting effect	(Lutran, et al., 1991)
X and Gamma (γ) rays CT	TBR With Glass Spheres Packing And Stainless Steel Pall Rings	CT to study liquid holdup	(Kantzas, 1994; Yin, et al., 2002)
Gamma (γ) rays CT	Liquid-Solid Bed System	Detect flow mal-distribution inside 60 cm diameter bed	(Boyer & Fanget, 2002)
X-ray PTV	Bubble Column	3D velocity of the liquid phased	(Seeger, et al., 2003)
X-ray	TBR	Visualize and characterize trickle flow in several hydrodynamic states	(Merwe, et al., 2007)
MRI	TBR	Liquid flow viewing, liquid velocity measurement, gas-liquid distribution and flow phenomena structure studies and pore structure study	(Sankey, et al., 2009; Sederman & Gladden, 2001)

- Runs without becoming limited by a large void fraction in bubble columns
- Measures all three velocity components for different measurement points in a volume
- Acquires the results of all measurement points simultaneously

A brief summary of the different non-intrusive techniques used for V_{LL} measurement in either a packed bed type reactor or a TBR system is given in Table 1.3.

1.3. SUMMARY AND RESEARCH OBJECTIVES

The preceding discussion suggests that V_{LL} measurements inside TBRs should be taken. It is also clearly indicates that a new method that is comparable to the established technique should exist. Such a technique could be used to validate other experiments. It could also support numerical computing to produce a better reactor design. The intrusive method (as discussed at the end of Subsection 1.1) will create disturbance within the natural flow of the system. Obtaining overall information about the reactor is also difficult with this technique. It is still; however, a method of choice for localized measurements.

Non-intrusive methods can be divided into several other methods: Optical methods (Subsection 1.2.1) and radiation methods (Subsection 1.2.2). Optical methods are often limited to the reactor's opacity. These methods are also sensitive to both the packing structure and noise coming from not only the light diffraction and but also the light deflection. An MRI is the only radiation method able to perform V_{LL} measurements. MRI can also be used to analyze liquid distribution. Other radiation base techniques are primarily used to visualize the trickling flow and perform other hydrodynamic parameters. Therefore, in order to measure the TBRs V_{LL} that offers non-invasive technique, applicable to laboratory scale setup, does not have diffraction and deflection problems and requires bigger interrogation size compared to the point measurement, further investigation and a new technique need to be developed.

Table 1.3. Summary of non-intrusive (both optical and radiation based) local liquid velocity (V_{LL}) measurements performed in a packed bed type reactor

Techniques	Experimental Parameters			Output (local)	References
	V_{meas} (cm/s)	d_p (cm)	Re		
Laser Doppler Velocimetry (LDV)	0.100 ± 0.10	1.27	0.158	Interstitial fluid velocity	(Johnston & Dybbs, 1975)
Particle Image Velocimetry (PIV) -Refractive Index -Florescence	0.0025	1	$1.25x10^{-3}$	2-D velocity fields and streamlines	(Saleh, et al., 1992)
	0.005	1	$3.6x10^{-3}$	Particle streamlines, velocity distribution	(Northrup, et al., 1993)
	0.05 to 1.25	0.47	2 - 500	Velocity field, velocity distribution	(Hassan & Ontiveros, 2008)
	0.4	0.7	28	Velocity field, velocity distribution	(Huang, et al., 2008)
	130	12.4	$2.1614x10^{4}$	Velocity field	(Lee & Lee, 2009)
Particle Tracking Velocimetry (PTV)	0 – 0.0128	0.31	-	Velocity field, velocity distribution	(Peurrung, et al., 1995)
	0.21 -5.51	1.9	0.049 – 0.129	Velocity field, velocity distribution	(Moroni & Cushman, 2001)
Magnetic Resonance Imaging (MRI)*	~ 5 $V_{SL\ for\ air}$ and ~ 50 $V_{SL\ for\ air\ and\ gas}$	0.5	$Re_g = 7.5$ $2.5 < Re_l < 43.2$	Velocity field, velocity distribution	(Sankey, et al., 2009; Sederman & Gladden, 2001)

*The only radiation technique that is applicable for both 2-D and 3-D V_{LL} measurements in TBRs

The completion of this work will add another novel, non-invasive technique to measure the V_{LL} in a TBR. It will also provide a better understanding of the effect of hydrodynamics on TBR performance with various conditions, facilitating both the design and scale-up of these types of reactors. This work will also provide data for benchmarking computational fluid dynamics (CFD) in a three-phase system. As a result, the primary objective of this work is to develop a new, non-invasive technique that uses digital industrial radiography (DIR) to measure the V_{LL} in TBRs.

The specific objectives of this study are to experimentally:

- Investigate, analyze, and evaluate, for the first time, combination of DIR with particle tracking techniques to measure the V_{LL} in a TBR
- Identify the most suitable tracking particles to be used for tracking with a DIR technique
- Identify the type of particle tracking suitable for the setup condition
- Validate the new technique with several approaches
- Identify and evaluate the behavior of the liquid flow located between the packing material
- Evaluate and compare the measured V_{LL} results with additional result obtained from published techniques.

Two small beds (22.5 mm and 40 mm diameter) packed with a low density material will be used for simplicity to gather data. Studies available in published literature will be used for comparison.

1.4. DISSERTATION ORGANIZATION

This dissertation is organized into six main sections. Section 1 introduces a general background of the work that has been conducted. It offers a brief introduction on TBRs: the concept behind TBR technology, work previously conducted on TBRs, and challenges associated with characterizing the TBRs hydrodynamic especially in measuring the V_{LL}. This section contains the motivation, research, a summary of all reviews, and the research objective of this work. Section 2 presents the theories on the

application of DIR, selection of exposure parameters, and particle selection. Concepts of particle identification, particle registration and validation for the developed procedure (particles: identification, registration, and tracking) will also be highlighted in this Section. Section 3 describes the research approaches that were being used in this research. Both methodology and apparatus used in this work are highlighted in this section. Section 4 discusses and highlights the results obtained from both 22.5 mm and 40 mm diameter packed tubes. Comparisons are made between published techniques. Point measurement (optical probe) validation techniques used to validate the measured are also discussed. Finally, Section 6 summarizes the work that has been developed. It also offers suggestions for future study.

2. THEORETICAL BACKGROUND

This section presents the theories of X-ray generation, DIR, PTV, and liquid Tortuosity in randomly packed bed. Approaches to ensure visibility of tracer particle inside TBR will also be highlighted in this section.

2.1. DIGITAL INDUSTRIAL RADIOGRAPHY (DIR) USING X-RAY TECHNOLOGY

Digital industrial radiography (DIR) is an advanced technique that involves computerized methods of investigation. A DIR image can be either directly acquired in digital form or converted into digital form by means of digitizing an analogue medium (e.g., film). Because the image is available as a computer file, it can be archived, copied, and transmitted to different places without any loss of information. It can also be digitally processed to either enhance required features or eliminate interfering ones. The list of available processing procedures is large and includes (Alekseychuk, 2006):

- The functional transformation of intensity (brightness, contrast adjustment, and histogram transformations)
- The filtering of both noise reduction and image sharpening
- Background linearization and elimination
- Image segmentation, object detection, and interpretation

Several DIR modalities have been applied as engineering inspection tools. The modalities are:

- Fluoroscopy system
- Film digitization system
- Computed radiography (CR)
- Flat panels that consist of the following:
    - Amorphous Silicon (A-Si).
    - Amorphous Selenium (A-Se).
    - Complementary metal oxide semiconductor (CMOS).

DIR technology was first developed for lower ionizing radiation within the medical field. When applied to industries in which the penetrating radiation energy is high, the spatial resolution becomes low. This low resolution is the most commonly reported weakness of DIR (Ewert, et al., 2004).

2.1.1. X-Ray as an Ionizing Radiation Source for Industries. X-rays were discovered in 1895 by the German scientist Wilhelm Conrad Roentgen while he was studying the phenomena of electrical discharge through gas (Shultis & Faw, 2002; Tsoulfanidis, 1995).

X-rays are electromagnetic radiation with wavelengths several thousand times smaller than that of light (between 0.0001 Å and 10 Å [1 Å = 10^{-8} cm]). Figure 2.1 illustrates the position of X-rays within the spectrum of electromagnetic radiation.

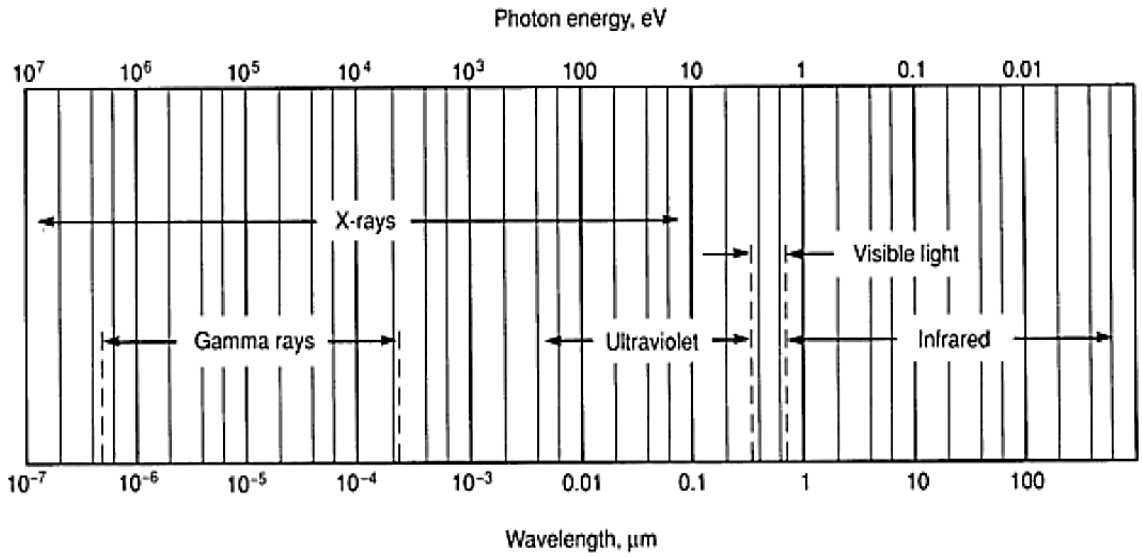

Figure 2.1. Electromagnetic radiation spectra (American Society for Metals, 1997)

There are two types of X-rays: Bremsstrahlung X-rays and characteristic X-rays. Bremsstrahlung (breaking radiation) X-rays are produced when fast moving electrons decelerate. This deceleration process causes electrons to lose their kinetic energy. The energy is converted into X-rays. Characteristic X-rays are produced when electrons are

instantaneously stopped, and all of their energy is converted into maximum X-ray energy. The X-ray spectrum is continuous with a definite minimum wavelength (λ_{min}). Bremsstrahlung X-rays are typically employed to produce images for use in industry (Ahmed, 2007). Using characteristic X-rays, certain material characteristic can be identified by measuring the resulting photon energy.

X-rays are invisible and cannot be felt by human sensors travelling at the speed of light (3 x 10^{10} cm/s). X-rays causes some materials to fluoresce e.g. Sodium Iodide (Tsoulfanidis, 1995) and harmful to living cells. X-rays can penetrate materials. The penetration process depends on the rays energy, material density, and material thickness. Such characteristics are important in acquiring radiographic images.

X-rays travel in a straight line. They can be reflected, refracted, and diffracted. A beam of mono-energetic X-rays obeys the following absorption Beer-Lambert law:

$$I = I_{\circ} e^{-(\mu/\rho)\rho x} \tag{1}$$

where $I_{\circ}$ is the incident intensity, I is the intensity of the X-rays transmitted through a material with x thickness with attenuation coefficient of μ/ρ and density ρ. X-rays are either absorbed or scattered as they pass through material. Equation (1) can be expanded into Equation (2) when used in irradiating multiple types of materials at once. This expanded equation considers various types of a material's property. Here, both $I_{\circ}$ and μ/ρ are a function of the energy, E set on the X-ray.

$$I = \int_0^{E_{max}} I_{\circ}(E) e^{-\sum_{j=1}^{j=n} (\mu(E)/\rho)_j \rho_j x_j} \, dE \tag{2}$$

Equation (2) takes all polychromatic X-ray sources and formed continuous intensity of radiation. Figure 2.2 illustrates samples of four calculated exposure spectra, with a tungsten target, for the same operating voltage but different amounts of beam filtration. Different X-ray beams are generated from different beam filtrations (material with different atomic numbers [Z] and thicknesses [x]). This figure also reveals both the continuous Bremsstrahlung spectrum and the superimposed characteristic X-ray lines. When compared to Al (x = 0.1 mm), higher x and Z values will shift the spectrum towards higher energy because X-rays with low energies are attenuated. At this stage, the X-ray beam is hardened.

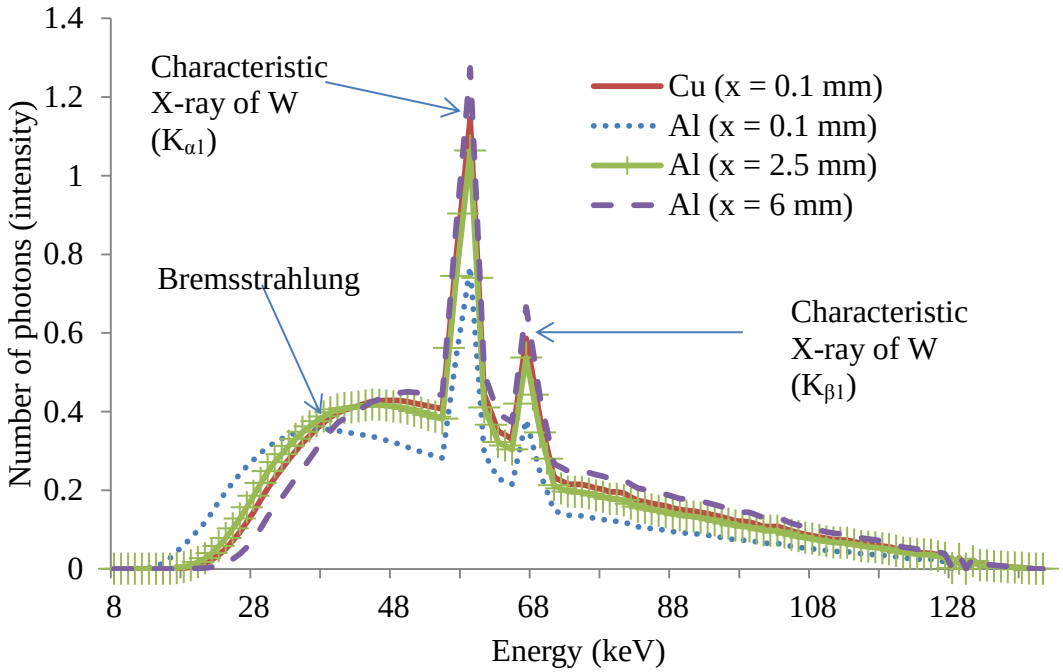

Figure 2.2. Example of photon spectra from X-ray tube (tungsten [W] target) at 140 kV potential with 0.1 mm Cu, 0.1 mm, 2.5 mm, and 6 mm Al filters thickness (Siemens, 2013)

Beam hardening can be utilized to increase X-ray penetrating capabilities. It also produces a better contrast between images, particularly when acquiring images of small objects.

Beam (intensity) produced from the X-ray tube can be represented by $I_{\circ}$ in Equation (2). A typical radiographic setup is illustrated in Figure 2.3. Three basic elements of this setup include the radiation source (X-ray), the detector, and the object under test. When exposed, the digital detector will acquire digital images of the object which are then transmitted to computers to be recorded, interpreted, reported, and archived.

Both X-ray source to detector distance (SDD) and the orientation of an object can influence the quality of the recorded images. Small objects which have same image level as noise level would not be seen with a bad quality image.

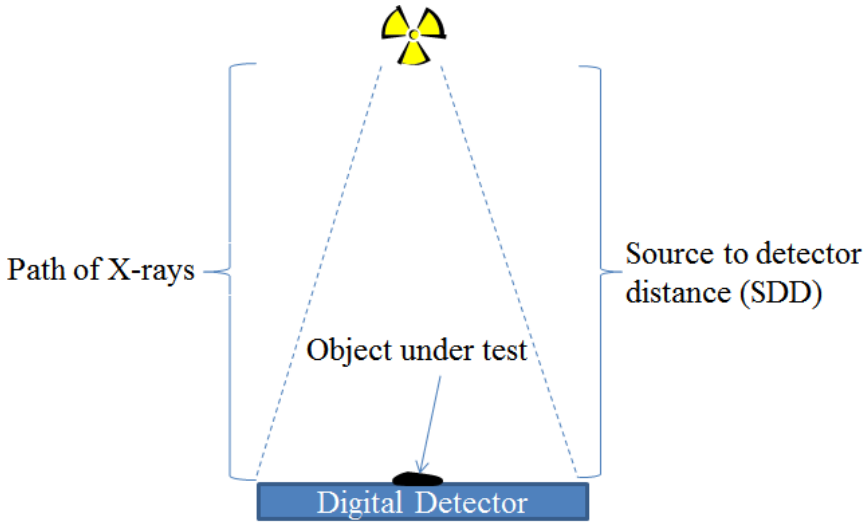

Figure 2.3. Sketch of basic X-ray DIR setup

The minimum SDD (SDD_{min}) is determined from the focal spot size, F and the object to detector distance (ODD).

$$SDD_{min} = ODD(\left({}^{F}/_{0.25}\right) + 1) \tag{3}$$

2.1.2. X-Ray Imaging in A Setup With Non-Homogeneous Material. The Beer-Lambert law in in Equation (1) is used when the attenuation coefficient of the material is assumed to be constant. For either a non-homogenous setup or a test sample, the passing X-ray beam will be attenuated by each different material.

Figure 2.4 illustrates the X-ray beam passing through three different materials with not only different sizes (x), but also different absorption coefficients properties (μ).

If $I_\circ$ is the initial intensity of the X-ray beam, the non-absorbed X-ray entering the second block (I_1) is

$$I_1 = I_\circ e^{-\mu_1 x_1} \tag{4}$$

The remaining intensity (I_1) goes to the second and the third materials with the following equations:

$$I_2 = I_1 e^{-\mu_2 x_2} \tag{5}$$

$$I_3 = I_2 e^{-\mu_3 x_3} \tag{6}$$

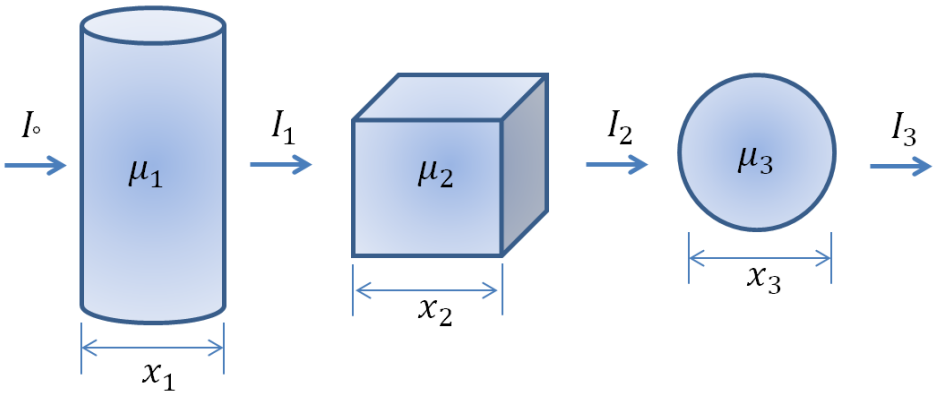

Figure 2.4. Absorption of X-ray beam in three different materials with different size and different absorption coefficients

Once the intensity emerges from the last material, the beam's intensity can be calculated with the following equation as expanded from Equation (1).

$$I_3 = I_\circ e^{-\mu_1 x_1 \times -\mu_2 x_2 \times -\mu_3 x_3} = I_\circ e^{-[\mu_1 x_1 + \mu_2 x_2 + \mu_3 x_3]} = I_\circ e^{-\sum \mu_i x_i} \tag{7}$$

where $i \in [1, 2, 3]$. In general, the total attenuation for the X-ray beam along three or more materials depends on thickness, density and attenuation coefficients. The attenuation coefficient (in Equation 2) is dependent on X-ray energy ($\mu(E)/\rho$). As a result, each material reacts differently to incoming X-ray intensity.

Figure 2.5 illustrates the mass attenuation coefficient $^{\mu}/_{\rho}$ for four materials with corresponding X-ray penetrating energy. Comparing these four materials to one single radiographic image, reveals a good subject contrast between barium titanate and the remaining materials (from 40 keV to 100 keV). The black dashed rectangular shape in Figure 2.5 indicates the chosen energy range.

Contrast is one of the two fundamental aspects in radiographic image quality. It measures the level of brightness between image components that correspond to the object under investigation. The other is basic spatial resolution which will be highlighted in Section 2.1.4.

Subject contrast (Con_{subj}) is determined by the final X-ray intensity to reach the digital detector and is dependent on the energy (Wolbrast, 2005). Equation (8) suggests the subject contrast is (Wolbrast, 2005)

$$Con_{subj} = \log_{10}(e^{-[\mu/\rho]\rho x_1}/e^{-[\mu/\rho]\rho x_2}) \quad (8)$$

$$\log_{10}\left(e^{-\mu(x_1-x_2)}\right) = 0.434\mu(x_1 - x_2) \quad (9)$$

Both Equation (8) and Equation (9) can be used to estimate the subject contrast of a formed image. The results will indicate the most appropriate penetrating energy to be used for the non-homogenous object of interest. If such an object of interest contains different types of materials (different density, ρ), as illustrated in Figure 2.6, then the relative intensity (photon ratio reaching the detector) for 40 keV – 100 keV is revealed as in Figure 2.7.

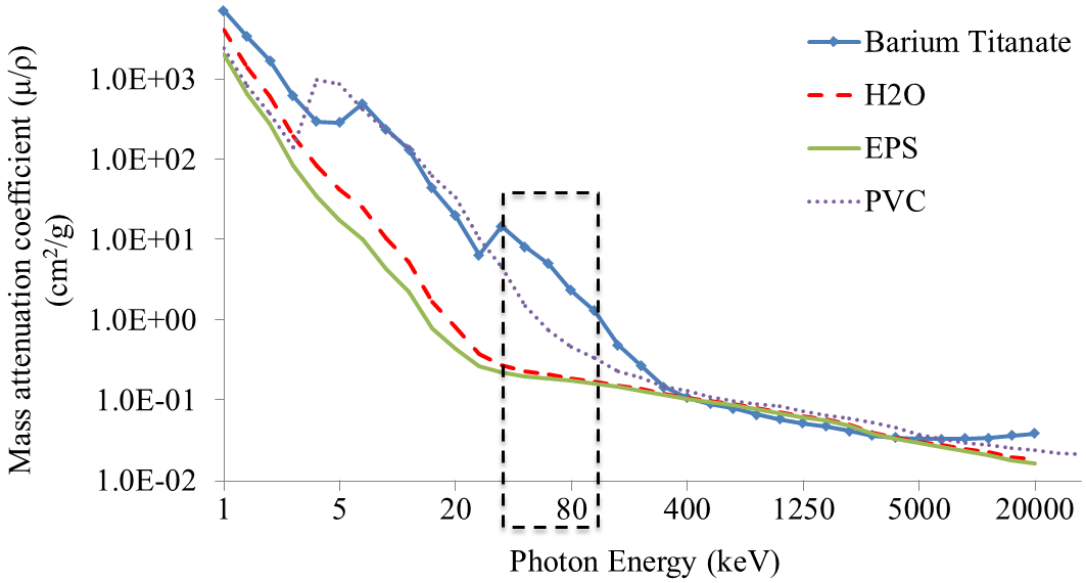

Figure 2.5. Mass attenuation coefficient μ/ρ for H_2O, expanded polystyrene (EPS), polyvinyl chloride (PVC), and barium titanate (NIST, 2011)

The relative intensity increases as the X-ray penetrating energy increases. Higher values indicate more X-ray photons are passing through the non-homogeneous material. The total is calculated with Equation (7). A good contrast between the H_2O

and PVC values with X-ray energies between 40 keV and 70 keV. Most of the X-ray beams are attenuated by H_2O.

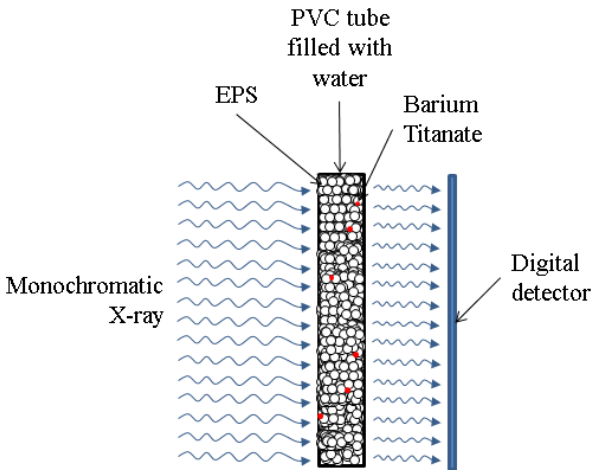

Figure 2.6. Object of interest built with four different materials: (PVC (ρ = 1.18 g/cm^3), Water (ρ = 1 g/cm^3), EPS (ρ = 0.025 g/cm^3), and Barium Titanate (ρ = 4 g/cm^3))

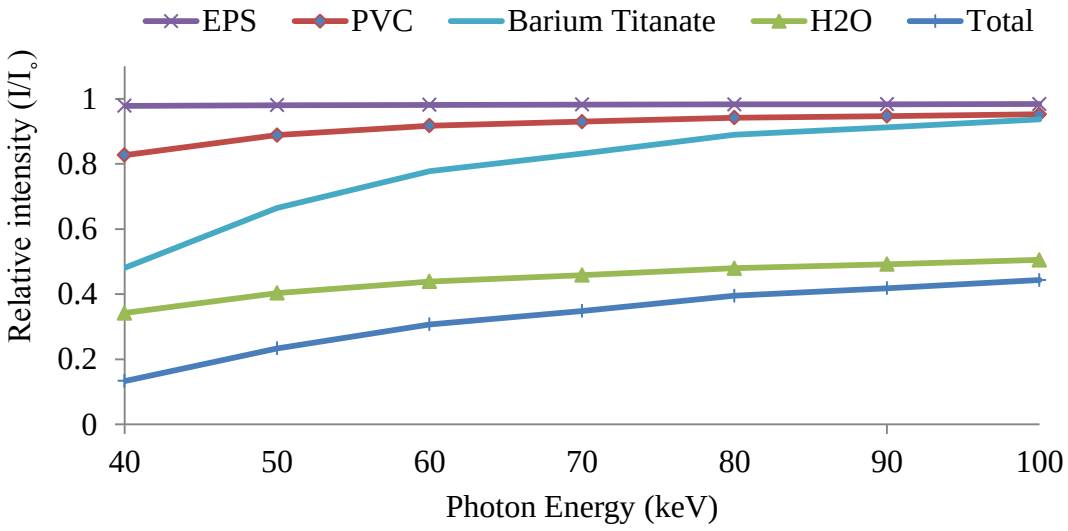

Figure 2.7. Relative intensity ($I/I_\circ$) for four different materials (x_{PVC} = 0.22 cm, x_{H_2O} = 4 cm, x_{EPS} = 4 cm, and $x_{Barium\ Titanate}$ = 0.0125 cm) exposed to monochromatic X-ray energy (40 keV to 100 keV)

2.1.3. X-Ray Digital Industrial Radiography (DIR) Detectors and Images. The basic principle of digital industrial radiography (DIR) detectors involves converting incoming X-rays into electrical charges that computers can read.

A DIR system can provide the implementation of computer image processing techniques, digital archiving, image transmission, and image extraction (Yaffe & Rowlands, 1997). Several DIR modules (or systems) have been used as part of engineering practice (non-destructive testing [NDT]). Figure 2.8 illustrates an overview of current DIR modules.

The film digitization technique has been used in the medical field for a number of years. This technique allows industrial radiographic films to be archived, quantitatively evaluated, processed (image processing), and reconstructed. Phosphorous base imaging plates (IP) (or a computed radiography (CR) system) is a technique that does not utilize radiographic film. Instead, it is exposed analogously to films, and the formed image is read with a laser scanner. The image is then erased, and the IP can be used again. Before the image can be viewed, both systems require a buffer time. This time allows the image to be stored, making it available to be stored read by another media.

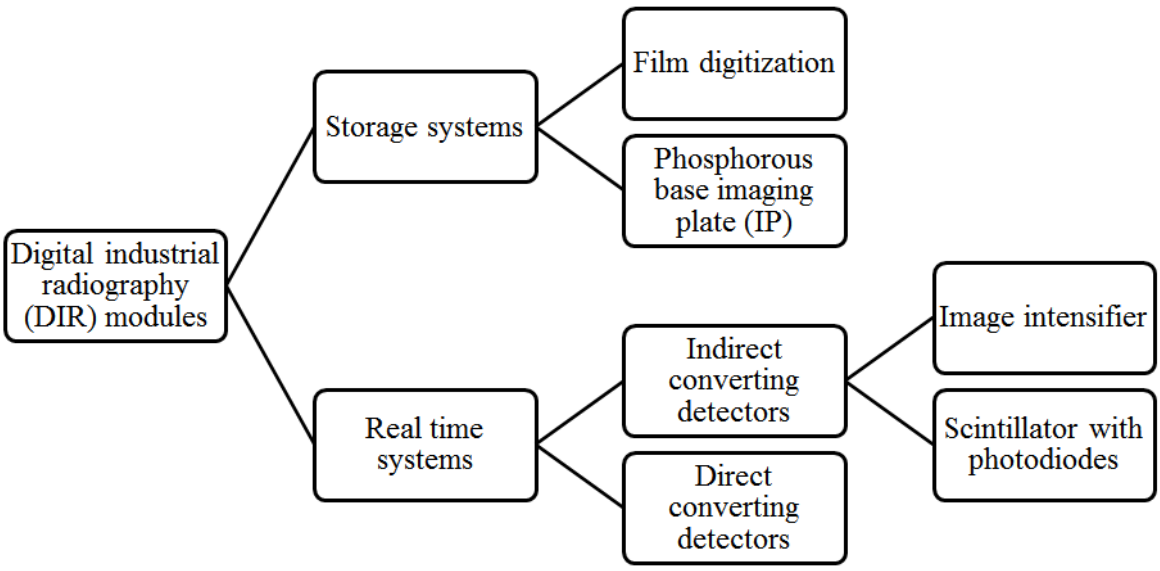

Figure 2.8. Overview of DIR systems currently used in industry

Real time systems (or flat panel technologies), as illustrated in Figure 2.9, allow a user to have a live, direct result for every exposure taken. The modalities are comprised of solid state electronic photodiodes, the same technology applied in a document scanner mechanism (Rowlands & Yorkston, 2000). Indirect DIR modules focus primarily on charge coupled device (CCD) flat panel, amorphous silicon (a-Si) flat panel, and complementary metal oxide semiconductor (CMOS) flat panel systems. Both modules require scintillating material that converts the X-ray into visible light. This visible light is detected by the photodiodes (pixels) and converted into an image that can be viewed on a computer. The light intensity emitted by the scintillating material corresponds to the X-ray intensity reaching the detector.

The direct converting detector converts the X-ray into an electrical charge without an intermediate stage (Rowlands & Yorkston, 2000). The detector typically consists of either amorphous selenium (a-Se) or cadmium telluride (CdTe) photoconductive materials. The X-ray generates electron hole pairs that are transported by the electron field and discharge the selenium layer (Cowen, 1991). Capacitive sensors attached to both sensitive amplifiers and a data acquisition system will read the charges. The charges collected by the pixel represent the acquired radiographic image.

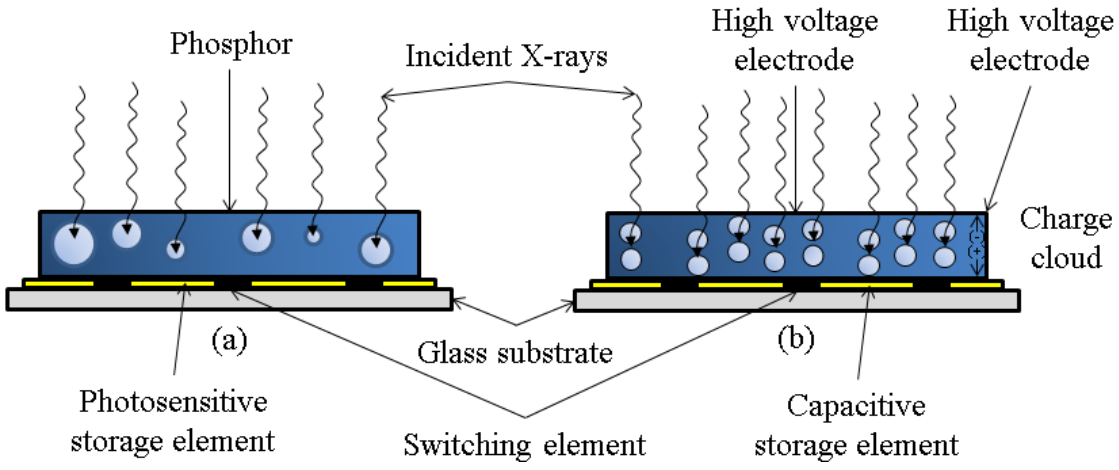

Figure 2.9. Cross-section of two DIR systems: (a) indirect conversion (b) direct conversion (Adapted from Rowlands & Yorkston, 2000)

DIR image formation is largely dependent on how it is first detected (by modules). The basic formation principle however is the same. X-ray radiation is detected, and the corresponding analog voltage signal is both generated and digitized. The image is then processed, stored, and viewed. Figure 2.10 illustrates the typical DIR imaging process procedure.

Mathematically, DIR image formation involves the object scene (*O*), the capturing process which is point spread function (*PSF*) and noise (*N*). The PSF contains all of the system's deterministic spatial-transfer information and is used to characterize the detector (Dobbins III, 2000). Noise is a disturbance caused by both electronics and unwanted X-ray quantum occurred during the exposure. The object function with the noise is convolved with PSF to form a DIR image and represented by Equation (10) (Solomon & Breckon, 2011):

$$Image\ formed = PSF * (O + N) \tag{10}$$

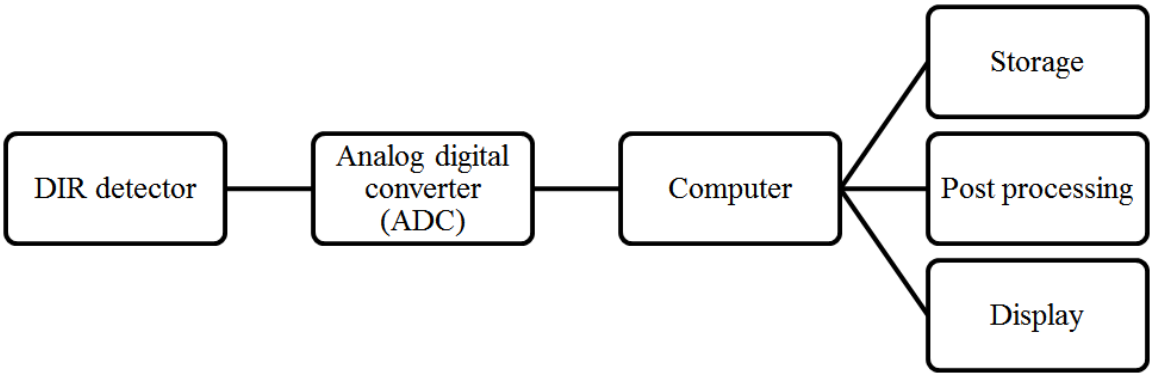

Figure 2.10. Typical procedure for DIR imaging systems

2.1.4. Discerning the Smallest Possible Object. One of the most commonly used quantitative measurement techniques in any digital detection system and practically applicable in DIR is the modulation transfer function (MTF) analysis (also known as basic resolution test).

MTF describes the imaging system's ability to display object contrast as a function of the object's size (Bushberg, et al., 1994). It provides a basic understanding

of how small a resolved DIR object can be. MTF describes the transfer of sinusoidal inputs within a spatial frequency domain. It has a unit of line pairs per spatial dimension, or mm (lp/mm). Mathematically, the basic principle of MTF determination through Fourier analysis is represented as follow (Dainty & Shaw, 1974)

$$MTF = \left|\int_{-\infty}^{\infty} l(x)e^{-2\pi iux}\right| \tag{11}$$

The line spread function (LSF) $l(x)$ can be found with

$$l(x) = \frac{d}{dx}(e(x)) \tag{12}$$

where *e(x)* is the detector's edge spread function (ESF).

Several approaches can be used to measure the MTF. Dobbins III (2000) highlighted three: the square wave method, the edge method, and the slit method.

The basic spatial resolution of a detector can also be analyzed with a duplex wire phantom. Because resolution is defined as the measure of the minimum separation of either two source points or sources, it can also be defined as the closest spacing of two lines that can be distinguished. Double wire image quality identification (IQI) (in accordance with European norm 462-5) is used as a test phantom to determine the image's resolution. Figure 2.11 illustrates a duplex wire between 0.8 line pairs per mm (cycles/mm) and 0.05 cycles/mm. Additional information on the double wire IQI can be found in Appendix A.

Figure 2.11. Double wire IQI

Image resolution is determined when a line pair is resolved (at a particular frequency) if the line pair image contrast exceeds some threshold quantity that is determined by the system's total noise. Hence, the resolving capability of an imaging system depends on contrast as well as noise level.

2.1.5. Scintillator with Complementary Metal–Oxide–Semiconductor (CMOS). Like any other DIR flat panel detector, matrix-oriented complementary metal-oxide-semiconductor (CMOS) photo-diodes, coupled with a scintillator screen, generates an output relative to the X-ray's input intensity.

Figure 2.12 is a schematic of a CMOS flat panel detector. This detector is one of the most inexpensive detectors available for DIR application (Rowlands & Yorkston, 2000). The image quality produced by the CMOS is comparable to the more expensive CCD and does not require an expensive frame grabbing system (Park, et al., 2004). A CMOS base system consumes less power, is portable (Russ, 2002) and is smaller than a-Si. DIR with CMOS technology allows higher resolution DIR imaging.

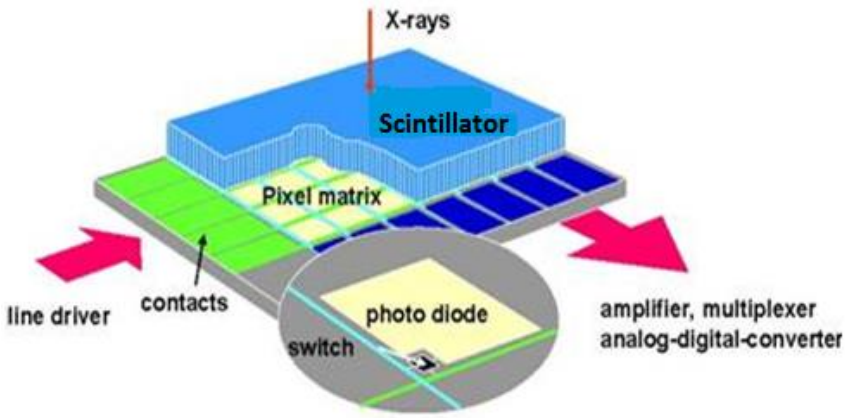

Figure 2.12. Schematic of a CMOS flat-panel detector (Adapted from Samei (2008))

2.2. THEORETICAL LIQUID VELOCITY

The liquid velocity inside a TBR (known as the interstitial velocity) can be theoretically calculated by relating the volumetric flow rate (Q) to the cross sectional

area of the reactor (A). This calculated value is known as the macroscopic interstitial velocity (V_{ML}). It is mathematically represented by Darcy as (Northrup, et al., 1993):

$$V_{ML} = Q/(\varepsilon_\beta A) \tag{13}$$

where ε_β is the TBR packing porosity. This porosity can be estimated with the following equation (Pushnov, 2006):

$$\varepsilon_\beta = (A/(D/d)^n) + B \tag{14}$$

where D is the tube diameter and d is the packing diameter. Equation (14) is valid for $D/d > 2$ and bed height $H > 20d$. The *A*, *B*, and *n* are constants that are dependent on the shape of the packing, as tabulated in Table 2.1. The V_{ML} value can be used to predict the average V_{LL} inside the TBR.

Table 2.1. Constant Values (Pushnov, 2006)

Grain Shapes	Coefficients		
	A	*B*	*n*
Spheres	1.0	0.375	2
Cylinders	0.9198	0.414	2
Irregularly shaped lumps	1.5	0.35	1
Rashing rings	0.349	0.5293	1

The inlet velocity or superficial liquid velocity (V_{SL}) is determined by the adjustment of Equation (13) when $\boldsymbol{\varepsilon_\beta}$ is removed.

The V_{SL} is used to introduce both water and gas. Interstitial flow characteristics can be represented by the Reynolds number (Re).

Both liquid and gas Re (either *L* or *G*) is calculated according to the packing's diameter and the V_{SL}.

$$Re_{L\ or\ G} = \rho_{L\ or\ G} V_{S\ L\ or G} d_{packing}/\mu_{L\ or\ G} \tag{15}$$

where ρ the density of the liquid, d is an average packing diameter, and μ is the dynamic viscosity of the liquid.

2.3. TORTUOSITY OF THE RANDOMLY FIXED BED

Tortuosity (τ) is a factor that characterizes the packing structure of a reactor and can be calculated with the following equation (Mota, et al., 1998; Delgado, 2006; Lanfrey, et al., 2010; Comiti & Renaud, 1989)

$$\tau = L_\varepsilon / L_{meas} \tag{16}$$

where L_ε is the actual length of the streamline in between the particle over the measured length of the streamline (L_{meas}) or particle radius (R). Tortuosity describes pore connectivity and fluid transport in packed bed and varies with particle volume fraction and particle size ratio in the mixture (Delgado, 2006).

Boudreau (1996) suggested both model and correlation of τ to be

$$\tau = \sqrt{1 - \ln \varepsilon^2} \tag{17}$$

Lanfrey et al. (2010) developed theoretical model for τ of a fixed bed that randomly packed with identical particles. They found the τ to be proportional to the packing structure factor and proposed τ to be

$$\tau = 1.23 \frac{(1-\varepsilon)^{4/3}}{\varepsilon \emptyset^2}, (\emptyset = 1 \text{ for spheres}) \tag{18}$$

where ε is the same as ε_β in Equation (14). When compared to experimental data (illustrated in Figure 2.13), Lanfrey et al. (2010) found that their model gives a mean relative error of 12% $\pm$ 10.6% standard deviation and the relative error to experimental results is less than 20% for porosity between 0.36 and 0.45.

The calculation of τ is basically incorporated with the ε of the bed (Boudreau, 1996; Lanfrey, et al., 2010). However, the τ in different flow conditions does exhibit

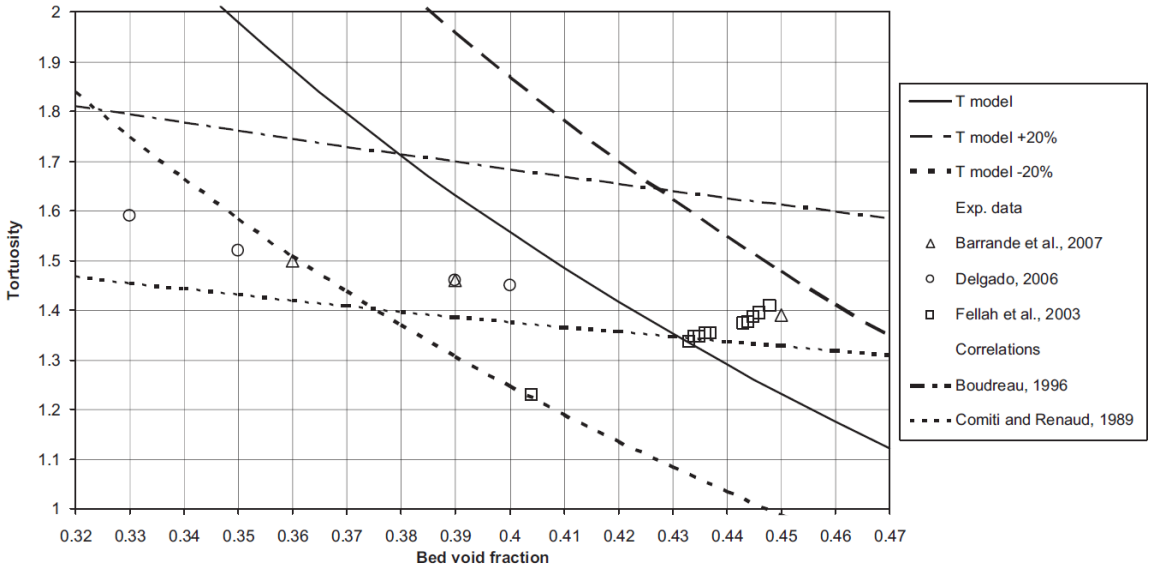

Figure 2.13. Comparison of experimental tortuosity values for beds of spheres (Lanfrey, et al., 2010)

dependency on the V_{SL} and V_{SG} of the system. (Narasimhan, et al., 2002; Boyer, et al., 2007). Narasimhan et al. (2002) suggested such τ as

$$\tau = \cos\theta - \mu \sin\theta \tag{19}$$

where

$$\theta = \frac{\pi}{2}(1 - e^{-K(V_L+V_G)}) \tag{20}$$

and

$$\mu = (k_1 - k_2)/(V_L + V_G) \tag{21}$$

The constants K, k_1 and k_2 were not included in any part of the paper and according to the authors, all constants need to be chosen to predict the τ. Such prediction might give errors and detrimental. Boyer et al., (2007) suggested that the for two phase flow, the τ may be represent by

$$(1\text{-}\alpha)^n \tag{22}$$

where n = -1 for multiphase and α is the volumetric gas holdup of the system. Since the volumetric gas holdup measurement was not covered in this work and selection of constants was thought to be detrimental, the τ will be determined based on the range and work done by Lanfrey et al., (2010).

2.4. PARTICLE TRACKING VELOCIMETRY (PTV)

The particle tracking velocimetry (PTV) method is one of the particle image velocimetry (PIV) modes often to be used in low density images (Adrian, 1991; Theunissen, 2003). It is simple, powerful, and often used in quantitative and qualitative study of flow visualization (Hassan, et al., 1992). PTV allows localized velocity measurements to be performed in either two-dimensional or three-dimensional formats (Ohmi & Li, 2000). This technique requires a smaller particle (known as seeder) to be suspended in the flowing fluid. The liquid movement can be determined over time by measuring the seeder's displacement. The seeder's movement is assumed to follow the liquid's movement.

In general, PTV is performed in two ways: (1) evaluating the particles on images of different exposures, (2) measuring the length of the particle trace formed at one exposure (Liu & Tao, 2007). The first method is often the method used when two or more sequences are overlapped by a known time Δt. Figure 2.14 illustrates a schematic for the PTV measurement technique. Each image is separated by known Δt (which is typically in millisecond).

Typical stage of PTV measurement in any flow study is highlighted in Figure 2.15. The particle detection, isolation, and registration are each known as a pre-processing stage.

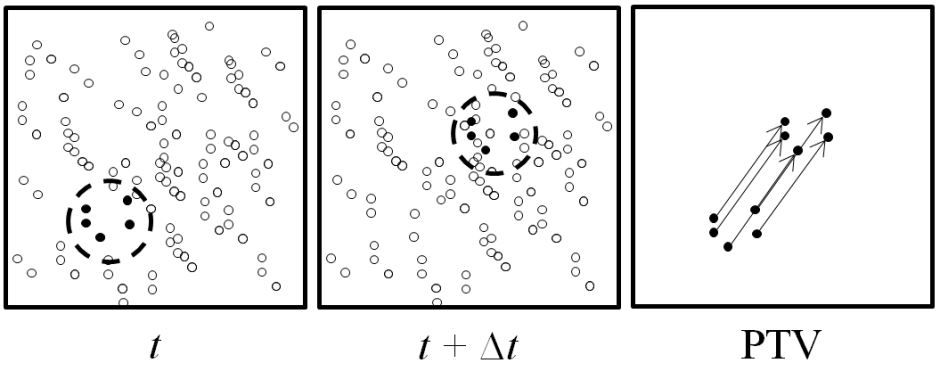

Figure 2.14. Simple schematic that illustrates how a PTV cross-correlates between two images separated by Δ*t*. The displacement of individual particles are measured and registered

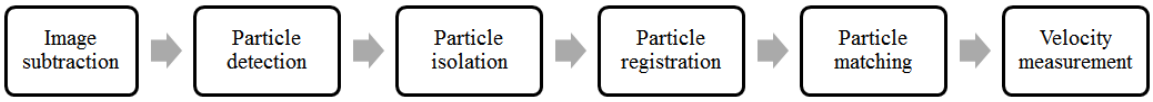

Figure 2.15. Typical stage in performing PTV measurement

2.4.1. Digital PTV. The PTV images formed by any digital means can be presented as *I(x,y)*.

The *I* represents the intensity of any object in the image while the *(x,y)* denotes the object's location (both row and column) within the Cartesian coordinate.

The image produced will contain noise that degrades the transfer function and reduces the object's contrast. Image subtraction will produce a new image with different pixel values as part of the image enhancement technique.

This step is the first step taken to ensure the seeding particle is successfully isolated. If the images *f(x,y)* and *BG(x,y)* have a difference of *g(x,y)*, some of the information in *f(x,y)* that exists in *BG(x,y)* (identical features) will be deleted. Figure 2.16 illustrates a scheme for the subtraction technique in which every new image will be generated when $I_{t=1\ldots n}$ is subtracted from I_{BG}.

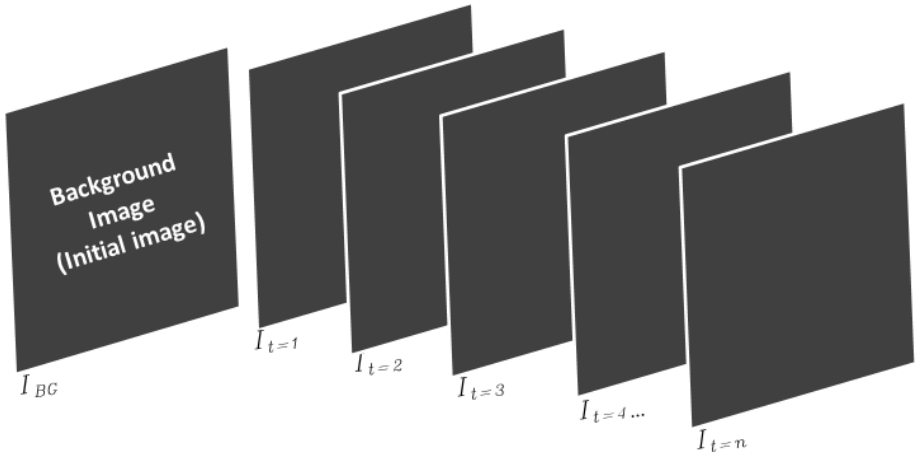

Figure 2.16. The subtraction scheme for multiple images taken at known constant Δt

The image subtraction technique will also, when necessary eliminate the non-moving part. The *BG(x,y)* is also known as the background image and is carefully chosen from among the other images. Because PTV measurements deal primarily with multiple digital image frame sequences, all of the image processing steps are conducted on every image.

Because the seeding particle is relatively smaller than the surrounding objects, the image requires a specific image processing procedure that isolates the particle. The image processing steps used to detect and isolate tracer particles are illustrated in Figure 2.17.

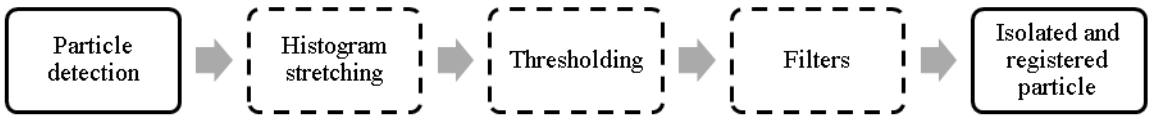

Figure 2.17. Particle detection steps

The histogram stretching (or histogram equalization) procedure enhances all of the intensity values in the image. By doing so, an object with a low contrast value can be visibly seen. Mathematically, histogram stretching (s_n) is represented by the following equation (Gonzalez & Woods, 2002):

$$s_n = T(r_n) = \sum_{j=0}^{n} p_r r_j = \sum_{j=0}^{n} \frac{n_j}{n} \quad (23)$$

$n = 0,1,2,\ldots$ L-1

where r_n is the level of pixels in an input image and p_r is the probability density function with random variable r.

Image thresholding (T) is a technique that segmentizes the seeding particle. It deliberately separates the image into regions of similar attribute and directly differentiates the particle from the noise (Pratt, 1991). This technique is best applied on individual images. Given $f(x,y)$ as an image to be analyzed and T as a threshold operation ($T = T[x,y,p(x,y),f(x,y)]$), the thresholded image $g(x,y)$ can be found from the following:

$$g(x,y) = \begin{cases} 1 \; if \; f(x,y) > T \\ 0 \; if \; f\,(x,y) \leq T \end{cases} \quad (24)$$

From Equation (24), pixels with a level of one correspond with the particle while pixels with 0 values correspond to the background. Global thresholding can be performed for a sequence of images when T depends on the image intensity. Both dynamic and adaptive thresholding are cumbersome to PTV measurements.

Histogram stretching and thresholding processes are each applied after subtraction. These steps are followed by object filtering. Object filtering is spatially used to enhance the particle's appearance; any noise (in terms of blobs) created by the surrounding object is eliminated. The number of pixels representing the seeder must be known, however, before this noise can be removed.

Theoretically, once the size of the pixel is known, either the filter algorithm or the kernels can be designed and then implemented in every image sequence. At this stage, the particle has already been identified and can be tracked according to not only the local intensity but also the center (radially).

2.4.2. Detecting Tracer Particle. Conventionally, each particle is tracked and matched on every image sequence by using a cross-correlation method (Ohmi & Li, 2000).

With the cross-correlation method, image *f(x,y)* can be mathematically matched with a reference image *h(x,y)* (template) using the following equation (Gonzalez & Woods, 2002):

$$f(x,y)\circ h(x,y) = \frac{1}{MN}\sum_{m=0}^{M-1}\sum_{n=0}^{N-1} f*(m,n)h(x+m,y+n) \qquad (25)$$

where both *M* and *N* represent the image's size, ° sign denotes the cross-correlation and $*$ denotes the convolution. If *h(x,y)* finds any correspondence in *f(x,y)*, the correlation between the two will be the highest. The cross-correlation coefficient (*R*) for both images (with *A* and *B* as their pixel matrices) can be mathematically represented by (Brevis, et al., 2011):

$$R = \frac{\sum_M \sum_N (A_{mn}-\bar{A})(B_{mn}-\bar{B})}{\sqrt{(\sum_m \sum_n (A_{mn}-\bar{A})^2)(\sum_m \sum_n (B_{mn}-\bar{B})^2)}} \qquad (26)$$

Additional techniques are often used, such as a combination of the cross-correlation and the relaxation method (Ohmi & Li, 2000), Gaussian fitting with maximum-likelihood estimation (Aguet, et al., 2005), and Gaussian fitting with nonlinear least-squares minimization (Brady, 2006) to track the seeder particle. The most recently introduced technique is based on the geometrical constraint of the particle (i.e. its radial profile) (Parthasarathy, 2012; Ma, et al., 2012). This technique is applied by identifying the Gaussian model on every image and thus detecting the seeder's PSF. The intensity distribution of each particle will provide specific PSFs that are based on their radial symmetry. According to Parthasarathy (2012), the particle's central location $I(x_c,y_c)$ can be localized with the following equation:

$$x_c = \Delta^{-1}\left[\left(\sum_k \frac{m_k w_k (y_k - m_x x_k)}{m_k^2+1}\right)\left(\sum_k \frac{w_k}{m_k^2+1}\right) - \left(\sum_k \frac{m_k w_k}{m_k^2+1}\right)\left(\sum_k \frac{(y_k - m_x x_k) w_k}{m_k^2+1}\right)\right] \qquad (27)$$

$$y_c = \Delta^{-1}\left[\left(\sum_k \frac{m_k w_k (y_k - m_x x_k)}{m_k^2+1}\right)\left(\sum_k \frac{m_k w_k}{m_k^2+1}\right) - \left(\sum_k \frac{m_k^2 w_k}{m_k^2+1}\right)\left(\sum_k \frac{(y_k - m_x x_k) w_k}{m_k^2+1}\right)\right] \qquad (28)$$

where k is the lattice midpoint. Both m_k and w_k are given as:

$$m_k = \frac{(I_{i+1,j+1} - I_{i,j}) + (I_{i,j+1} - I_{i+1,j})}{(I_{i+1,j+1} - I_{i,j}) - (I_{i+1,j})} \tag{29}$$

$$w_k = \frac{\left|\vec{\nabla} I_k\right|^2}{d_{k,c}} \tag{30}$$

where $(I_{i+1,j+1} - I_{i,j}) + (I_{i,j+1} - I_{i+1,j})$ is the Roberts cross-operator for image $I(i,j)$ and $d_{k,c}$ is the distance (d_c) between (x_k, y_k) and the centroid of $\vec{\nabla} I_k$ (the gradient of the intensity calculated from the image at the midpoints between the pixels' centers) (Parthasarathy, 2012). Figure 2.18 illustrates the simplified particle centroid detection that localizes the tracer particle.

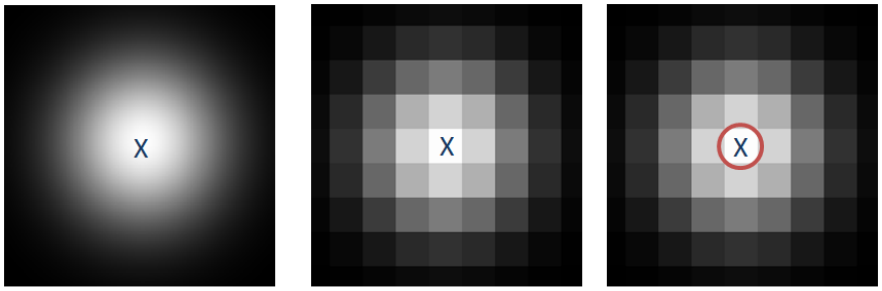

Figure 2.18. Particle detection and localization using radial symmetry approach with: (a) simulated point source (distributed Gaussian) (b) simulated CMOS image of a point source from (a) where the X is the center of the particle (c) red circled X with calculated x_c and y_c (Adapted from (Parthasarathy, 2012))

3. EXPERIMENTAL SETUP AND MEASUREMENT TECHNIQUES

Numerous studies have measured the local liquid velocity (V_{LL}) of trickle bed reactors (TBRs). Most of these studies either obstructed the liquid flow or limited to only point measurement technique. A technique based on the radiation method (e.g. MRIs), offers a non-invasive approach, eliminates optical related problems (diffraction and deflection), is applicable to laboratory scale setups and interrogates a bigger region of interest.

In this section, both the designed experimental setup and the series of experiment used in this study will be explained. Each experiment was replicated three times. Additionally, three different but relevant experiments were designed and performed to validate the results.

3.1. TRICKLE BED REACTOR (TBR)

Trickle bed reactors (TBRs) are multiphase-type reactors in which liquid phases are introduced at the top of the column to flow concurrently down through the packed bed of catalyst.

3.1.1. The Bed Setup. The trickle bed reactor setups utilized in this study consisted of two separate Polyvinyl Chloride (PVC) tubes. One tube had a diameter of 2.25 cm, and the other had a diameter of 4.5 cm; each was 40 cm tall. Theses tubes were packed with 3 mm Expanded Polystyrene (EPS) beads up to 30 cm.

The beads chosen were able to mimic the catalyst packing because they possess both a low atomic number and low a density (approximately 25 kg/m^3) (Basavaraj, et al., 2005). The low density EPS beads allowed more penetrating X-rays to reach the CMOS for a better image contrast. This contrast allowed the tracking particles to be located easily. The 2.25 cm PVC tube was used for the two-phase (solid-liquid) experiments while the 4.5 cm tube was used for the three-phase (solid-liquid-gas) experiments. The beads were soaked with water as part of pre-wetting procedure before they were randomly packed inside the tube to form the bed.

For both tubes, deionized water with a constant temperature (70 (±2) °F) was used for the liquid phase and compressed air (from oil less compressor) was used for the gas phase. Both were maintained at 20 psi. The liquid and gas flow rates were each controlled by needle valves and measured by rotameters (Dwyer Instruments, USA, and Range: 50 ml/min– 500 ml/min). The accuracy is within ± 2%. The experiments were performed in continuous mode as both liquid and gas outputs were channeled to the drain at atmospheric pressure. A syringe injection port was installed between the needle's valve and the liquid inlet (T-Connector). A computer-controlled syringe pump (NE-1000, New Era Pump Systems, USA), set to 10 ml/min, was used to continuously pump the tracer particle mixture into the liquid while the main liquid was moving. The dispensing accuracy is ± 1%. A liquid and gas distributor was placed between not only the fluid and gas inlet but also the packing to ensure a uniform flow occurred inside the bed. Check valves were used to avoid pressure back of the liquid-particle mixture.

Figure 3.1 illustrates the experimental trickle bed reactor setup that was used in this experiment. There was no gas inlet for 2.25 cm diameter PVC tube (solid-liquid experiment).

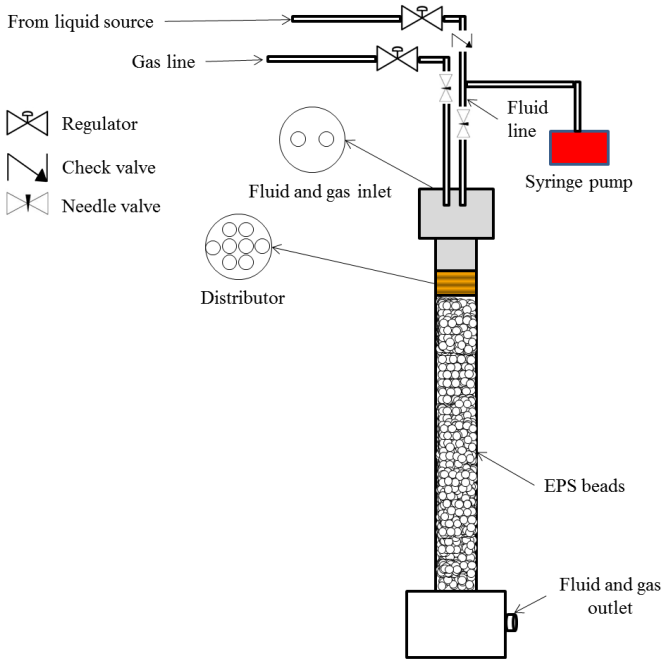

Figure 3.1. Schematic of experimental trickle bed reactor setup

The bed was fully wetted by allowing the maximum liquid mass flow rate to run into the bed. Both soaking and fully wetting procedures were performed to ensure constant liquid channeling pattern.

The theoretical interstitial velocity, tabulated in Table 3.1, was calculated based on Equation 13 where ε_β in Equation 14 was found to be 0.38.

Table 3.1. Calculated theoretical interstitial liquid and gas velocities ($V_{M\ (L\ and\ G)}$)

Tube ID (cm)	Volumetric Flow Rate, *Q* (ml/min)		Macroscopic Interstitial Velocity, $V_{M\ (L\ and\ G)}$ (cm/s)	
	L	G	L	G
2.25	100	Single Phase	1.11	Single Phase
	200		2.21	
	266		2.93	
4.5	130	1000	0.36	2.76
	260		0.72	
	380		1.05	

3.1.2. Reynolds Number and Superficial Liquid Velocity. For 2.25 cm diameter tube, the calculated and applied V_{SL} (cm/s) were 0.42, 0.84 and 1.11. The Re_L were 12.5, 25 and 32.5. For 4.5 cm diameter tube, the calculated and applied V_{SL} (cm/s) were 0.13, 0.27 and 0.39. The Re_L were 4, 8 and 11.5 and Re_G was 2.55.

Table 3.2 simplifies the parameters used in this experiment for both diameters. The V_{SL} is smaller than the V_{ML} because it was calculated according to the cylinder's surface area. Figure 3.2 illustrates that the region of experiments performed was in the trickle flow regime. This flow map was adapted from Al-Dahhan & Dudukovic (1995).

Table 3.2. Parameters applied in this experiment

Tube ID (cm)	Volumetric flow rate, *Q* (ml/min)		Superficial velocities, $V_{S(L \text{ or } G)}$ (cm/s)		Mass flux, ϕ (kg/m^2s)		Reynolds number, $Re_{(L \text{ or } G)}$		Pressure, P (psi)	
	L	G	L	G	L	G	L	G	L	G
2.25	100	Single Phase	0.42	Single Phase	4.2	Single Phase	12.5	Single Phase	20	Single Phase
	200		0.84		8.4		25			
	266		1.11		11.1		32.5			
4.5	130	1000	0.13	1.05	1.3	0.013	4	2.55	20	20
	260		0.27		2.7		8			
	380		0.39		3.9		11.5			

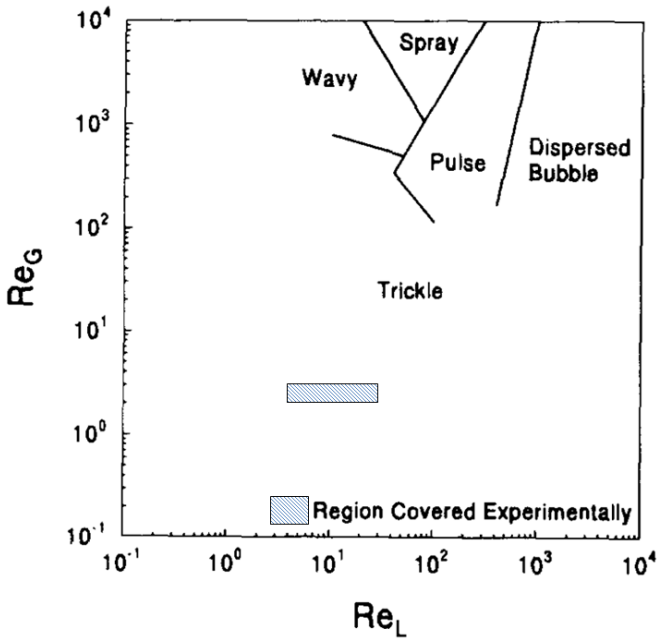

Figure 3.2. Region of trickle flow regime covered experimentally

All of the experiments were replicated four times. For each replication, fresh EPS beads were used as the packing and flow conditions were maintained. The tube was thoroughly washed and dried to ensure that a minimal amount of particle-liquid mixture residue occurred.

3.2. DIGITAL X-RAY INDUSTRIAL RADIOGRAPHY (DIR) SETUP FOR TRACER PARTICLE MEASUREMENT

This experiment utilized both an industrial grade X-ray source and a Complementary Metal Oxide Semiconductor (CMOS) flat panel detector. Both computer controllable X-ray generator and tube (Gulmay, HPX-225-11, UK) with a penetrating energy range between 20 kVp to 225 kVp (interchangeable focal spot size in between 0.4 mm and 1 mm) and current range of 0 mA to 3 mA were used as the X-ray source.

The flat panel X-ray detector (Rad-icon, Shad-o-Box 1024, USA) incorporates a Gd2O2S scintillator screen (Min-R 2190 std.) with a CMOS-type photo diode array. It has an active area of 50 mm x 50 mm with a 48 μm pixel pitch, 2.7 fps (370 ms per frame), a 4000:1 dynamic output, and a maximum allowable penetrating energy of 160 kVp. In this study, the array was protected from ambient light by a carbon-fiber shield.

3.2.1. Spatial Resolution Test. Both spatial resolution properties and noise characterizations of the X-ray detector system were evaluated with the Modulation Transfer Function (MTF) method. MTF measurements were taken prior to performing V_{LL} measurements and performed using the same as those used to determine the V_{LL}.

Each measurement was taken with a double wire IQI (EN 462-5, IE-NDT, England), as illustrated in Figure 2.11. Figure 3.3 (a) shows the radiographic image of this IQI. The spatial resolution measurement was taken when the separation of the wire (representing two intensities: high and low), was near 20%. Figure 3.3 (b) illustrates the plotted profile line. This line reveals a 28% difference between the two peaks (bottom right of Figure 3.3 (b)). The estimated MTF, from the spatial resolution measurement, at 20% of the modulation ($MTF_{20\%}$) was 6.25 lp/mm (11D).

This finding is in agreement with results collected by both Yagi et al. (2004) and Teledyne Rad-icon Imaging Corp (2013). Sinha et al. (2013) found the MTF to be 8 lp/mm and 8.5 lp/mm at $MTF_{10\%}$. All measured $MTF_{20\%}$ values suggest that the setup allows the smallest discernible object to be between 80 μm and 100 μm. Figure 3.4 is an image of the X-ray source used in this study; Figure 3.5 is an image of the CMOS X-ray used.

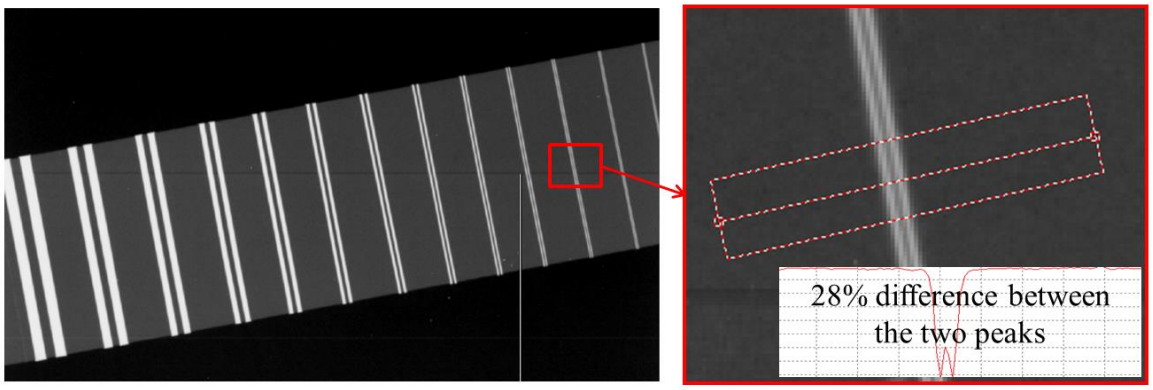

Figure 3.3. Initial steps for MTF measurement: (a) Radiographic image of the IQI (b) Averaged line profile that shows a 28% difference between the high and the low intensities

More detailed, quantitative evaluations on the same detector model, including the Noise Power Spectrum (NPS) and the Detective Quantum Efficiency (DQE), have been published (Sinha, et al., 2013; Yagi, et al., 2004; Teledyne Rad-icon Imaging Corp, 2013).

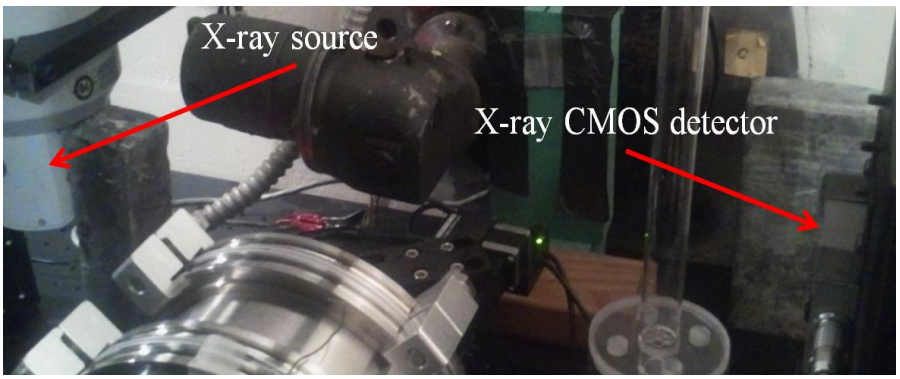

Figure 3.4. X-ray source used in this study

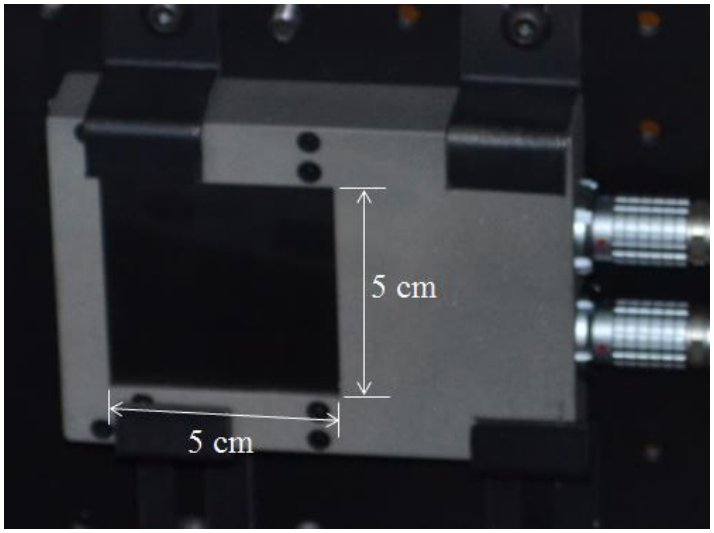

Figure 3.5. CMOS X-ray detector used in this study

3.2.2. Determination of X-Ray Exposure Parameter. The first step taken to determine the exposure parameters was to individually calculate, for all materials, the final X-ray intensity detected by the CMOS.

To do so, each (PVC, tracing particle, EPS beads and water) mass attenuation coefficient (μ/ρ) was identified. The μ/ρ for all materials were then plotted against the corresponding energies. Based on Section 2.1.2 and Figure 2.5, the energy at which this TBR operated most effectively was between 40 keV and 200 keV.

The penetrating energy was reduced according to the $I/I_{\circ}$ ratio, as illustrated in Figure 2.7. From the figure, it suggests that 100% of the X-ray energy was detected by the CMOS when a 4 cm thickness of EPS beads was irradiated. 80% of the initial intensity was detected at a 40 keV X-ray energy for PVC with a 0.22 cm thickness and a 2 cm radius.

In this experiment, the penetrating energy chosen (between 50 keV and 70 keV) was based on information presented in Figure 2.7. This range produced a good radiographic contrast for non-homogenous material (e.g. PVC, EPS beads, Barium Titanate, and water).

In order to validate the calculated final intensity reaching the detector, series of visibility test with X-rays were performed by setting up a 10 cm high and 2.25 cm diameter water filled PVC tube. By using the identified energy range and 2 mA current,

the X-ray beam was later hardened with 2 mm Al thickness, as shown in Figure 2.2. This was done to enhance the image contrast. Figure 3.6 illustrates the packed tube (with tracer particles) that was used to validate the calculated value.

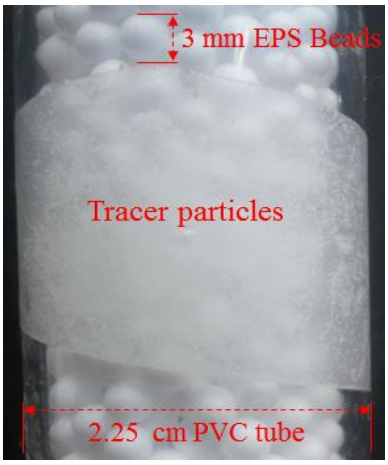

Figure 3.6. 2.25 cm water-filled PVC tube packed with 3mm EPS beads. The tracer particles were 106 μm to 125 μm size

The setup was placed in front of the CMOS detector. The tracing particles were taped and faced the detector. The distance between the X-ray tube and the detector (SDD) was 650 mm. The penetrating energies used were 50 kVp, 60 kVp, and 70 kVp.

Figure 3.7 is a radiographic image obtained from the experiment. The acquired images were not manipulated and it can be seen that the best obtained radiographic image contrast was from 60 kVp exposures.

The image taken at 50 kVp (Figure 3.7 [a]) had a lower overall intensity; distinguishing between the EPS beads, the liquid, and the tracer particles was quite demanding. The small tracking particle size taken at 70 kVp (Figure 3.7 [c]) was almost attenuated, particularly in the tube's mid-section. Figure 3.7 (b) shows the best discernible image between the tracer particles, packing and liquid. This finding gives a practical proof to the calculated $I/I_{\circ}$.

The size range identified in the MTF test (both 80 μm and 100 μm) was also verified. The range was divided into three smaller ranges. From the three radiographic

images (see Figure 3.8), tracer particles within the size range of 106 μm and 125 μm (see Figure 3.8 [c]) offer better acuity.

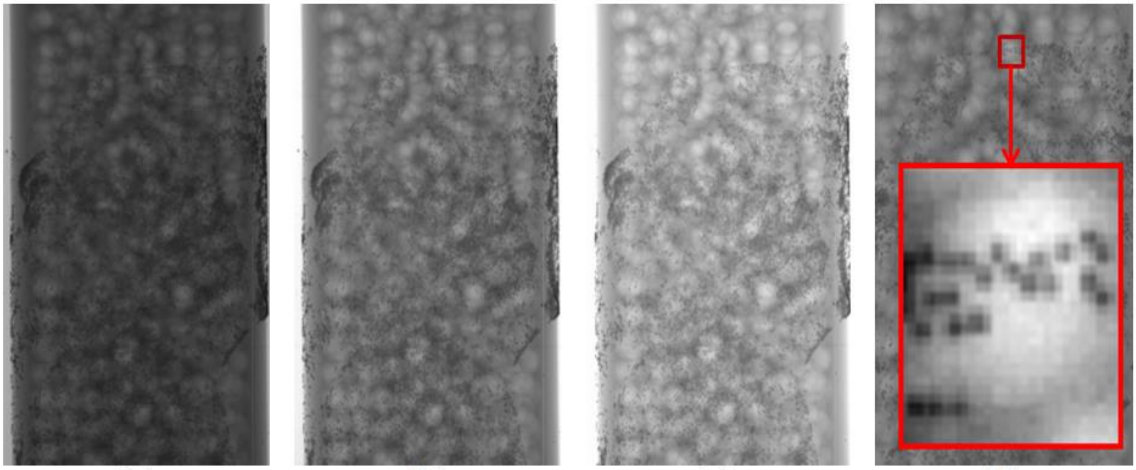

Figure 3.7. X-ray radiographic images for non-homogeneous materials at 2 mA, 650 mm SDD and penetrating energy at (a) 50 kVp (b) 60 kVp (c) 70 kVp (d) Magnified image of identified tracing particle from a 60 kVp radiographic image

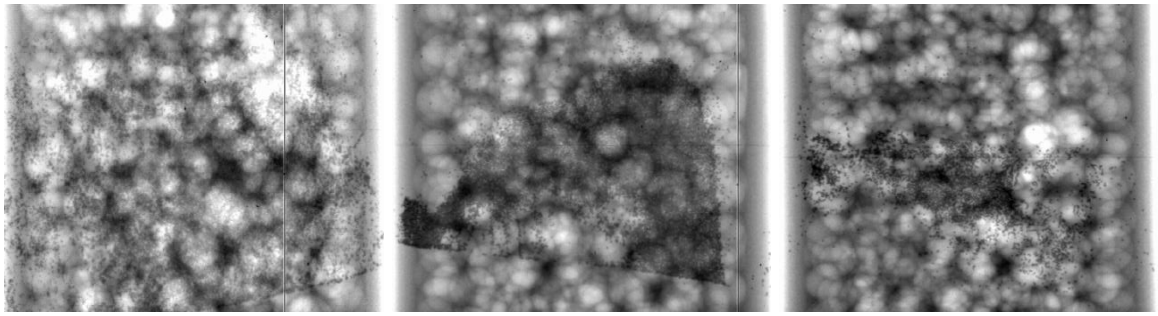

Figure 3.8. Radiographic image (60 kVp, 2 mA, 650 mm SDD) of tracer particles: (a) 75 μm to 90 μm (b) 90 μm to 106 μm (c) 106 μm to 125 μm

3.3. PARTICLE ISOLATION AND TRACKING

The tracer particles used in this experiment were 1.9 refractive index barium titanate beads that were between 106 µm and 125 µm. A visibility assessment was conducted according to not only the energy range but also the spatial resolution. For this novel technique been successful, to have the tracer particles that is able in attenuate X-rays. Particles were tracked using both the procedure and the steps highlighted in Section 0 and Figure 2.17.

Section 2.4.1 and Figure 2.16 revealed that the X-ray radiographic frames needed to be acquired before the PTV measurements could be taken. The procedure was implemented by saving multiple radiographic image frames on the setup as illustrated in Figure 3.9.

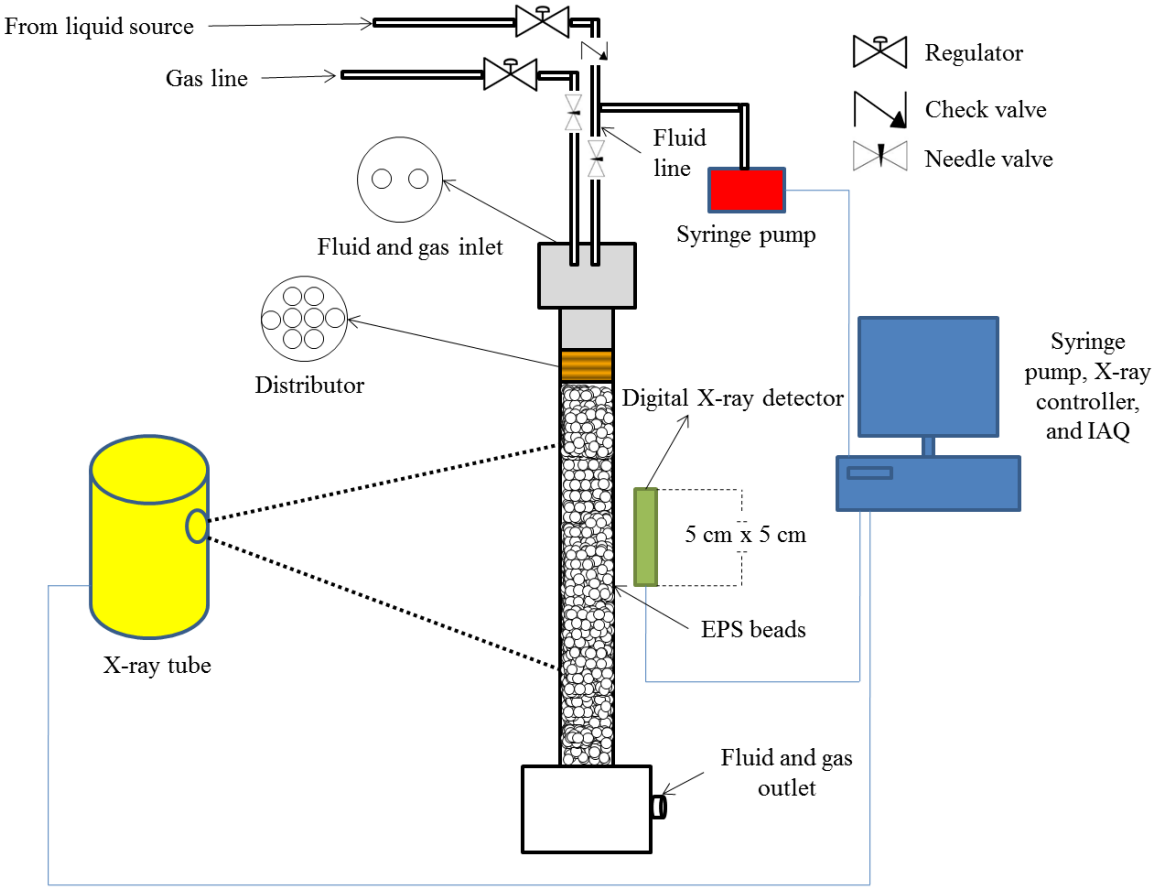

Figure 3.9. The bed setup (with both on X-ray tube and a detector) utilized in this study

The maximum mass flow rate of deionized water was introduced to the bed for 30 minutes before each experiment was performed. The water was then set to the corresponding V_{SL}, so that it could flow through the tube continuously for an additional 15 minutes.

The CMOS detector was set to both its highest frequency (Δt = 370 ms) and a continuous mode to allow the computer to grab all captured radiographic images. The pump (controlled by computer software) was triggered to push all water-tracer particle mixtures into the stream. The recorded images, beginning with the pre-mixture flow, were saved directly into the computer. The image frame was later used as a control image for background (*BG(x,y)*) purposes. Once the syringe pump was triggered, the post-mixture frames were automatically acquired and saved.

Each post-mixture flow frame was subtracted from the pre-mixture flow frame (as shown in Figure 2.16), leaving only flow that contained tracer particle information (I_{diff}). The remaining particles were isolated according to the steps illustrated in Figure 2.17 and Figure 3.10 reveals the simplified procedure for particle isolation used in this experiment.

Figure 3.10 (a) is the background image obtained, and Figure 3.10 (b) is one of the initial images that contain tracer particles in it. Figure 3.10 (b) illustrates the I_{diff}. The I_{diff} histogram was stretched before global thresholding was applied. Large blobs (caused by the water) were removed with area filtering and specific thresholding. Area filter was applied to remove the remaining blob.

The isolated particle was then tracked with a radial symmetry from a particle intensity distribution (described in Section 0) to provide the location of each unique particle in every image sequence. This tracking procedure was then used to provide a path line of the moving particles. Each distance was divided with 370 ms to obtain the velocity of each particle.

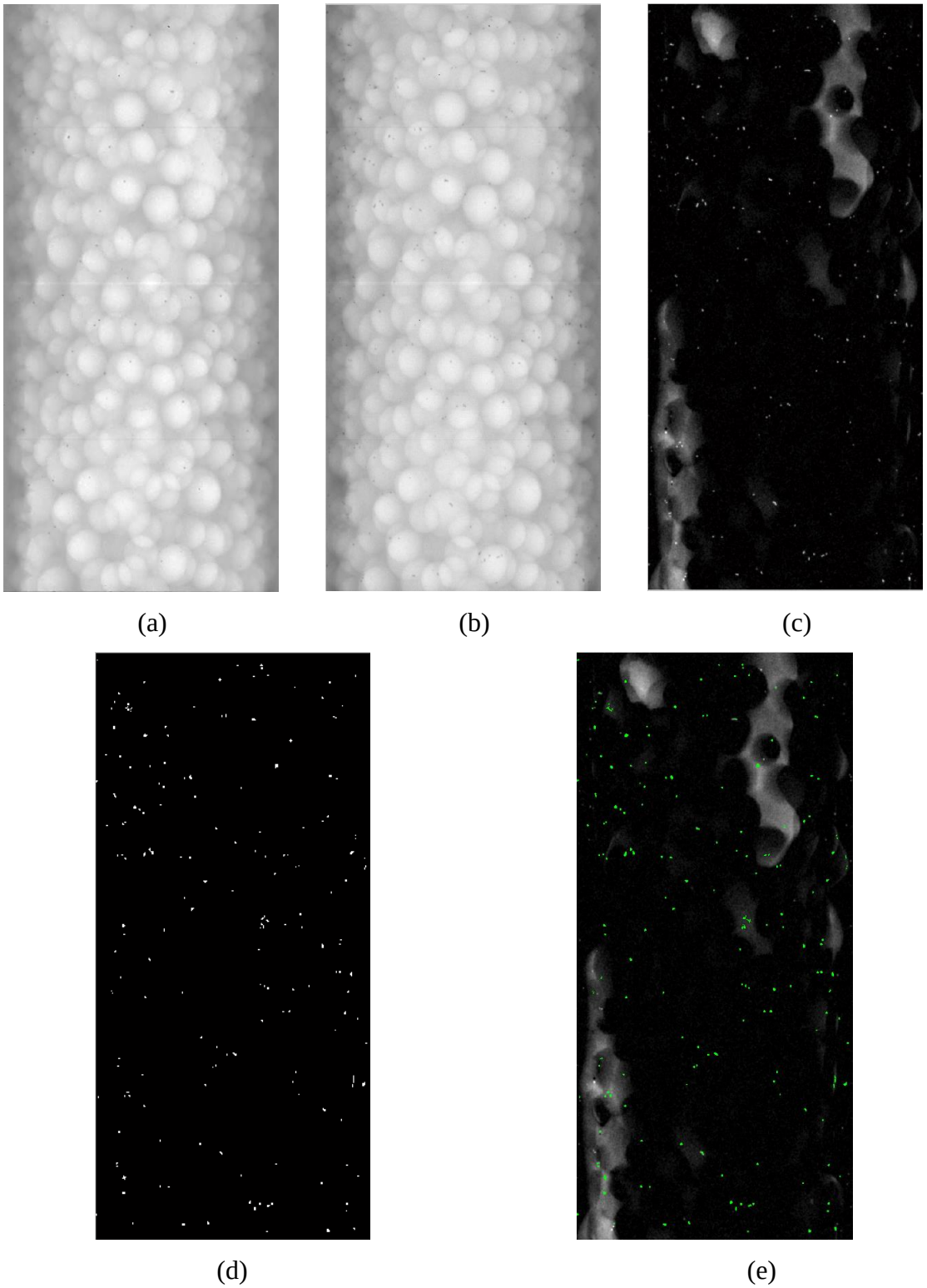

Figure 3.10. Simplified procedure for the particles isolation. (a) Background image (pre-mixture flow) (b) $I_{t=1}$ (c) I_{diff} (d) Identified tracer particle (e) Masked identified particles on I_{diff}

4. VALIDATION

4.1. PARTICLE DETECTION TEST IN TWO CONSECUTIVE ARTIFICIAL IMAGE FRAMES

Two artificial images, assumed to be consecutive, were used to test the tracking algorithm used in this experiment. Each image contained 20 and 2000 artificial particles and has a size of 586 pixels x 939 pixels. The artificial tracer particles in both images had a size range of 16.45% difference (106 μm to 125 μm) to mimic the actual tracer particles used in this study. Figure 4.1 presents the created artificial images that contained the artificial tracer particles moving in a circular direction. These 8-bit images were created by adding Gaussian noise. Figure 4.1 (a) and Figure 4.1 (b) include images that contain 20 artificial particles (5 max pixel displacements). Figure 4.1 (c) and Figure 4.1 (d) include images with 2000 artificial particles (10 max pixel displacements).

The algorithm used, highlighted in Section 2.4, was successfully applied to show the intended movement of artificial tracer particles. The movement vectors for both artificial tracer particles on each artificial image were plotted in Figure 4.2. The velocity fields corresponded well to the intended random, circular motion, particularly in Figure 4.2 (b). The vector was clearly defined and plotted on both artificial images. The length of each vector corresponds to the magnitude of pixel displacement.

4.2. PROCEDURE TEST ON KNOWN VELOCITY

After the successful particle detection test, the entire procedure, highlighted in Section 3.3, was further tested by measuring a known velocity. In this test, a syringe, filled with a liquid-tracer particle mixture, was connected to a tube with an internal diameter of 4.25 mm.

This tube was placed in front of an X-ray detector so that radiographic images (9.45 mm x 34.3 mm) could be acquired (see Figure 4.3). The X-ray penetrating energy and current were 40 kVp and 2 mA, respectively; the SDD was set to 650 mm. A

syringe pump was used to pump the mixture with a constant superficial liquid velocity at 0.0587 ± 1% cm/s.

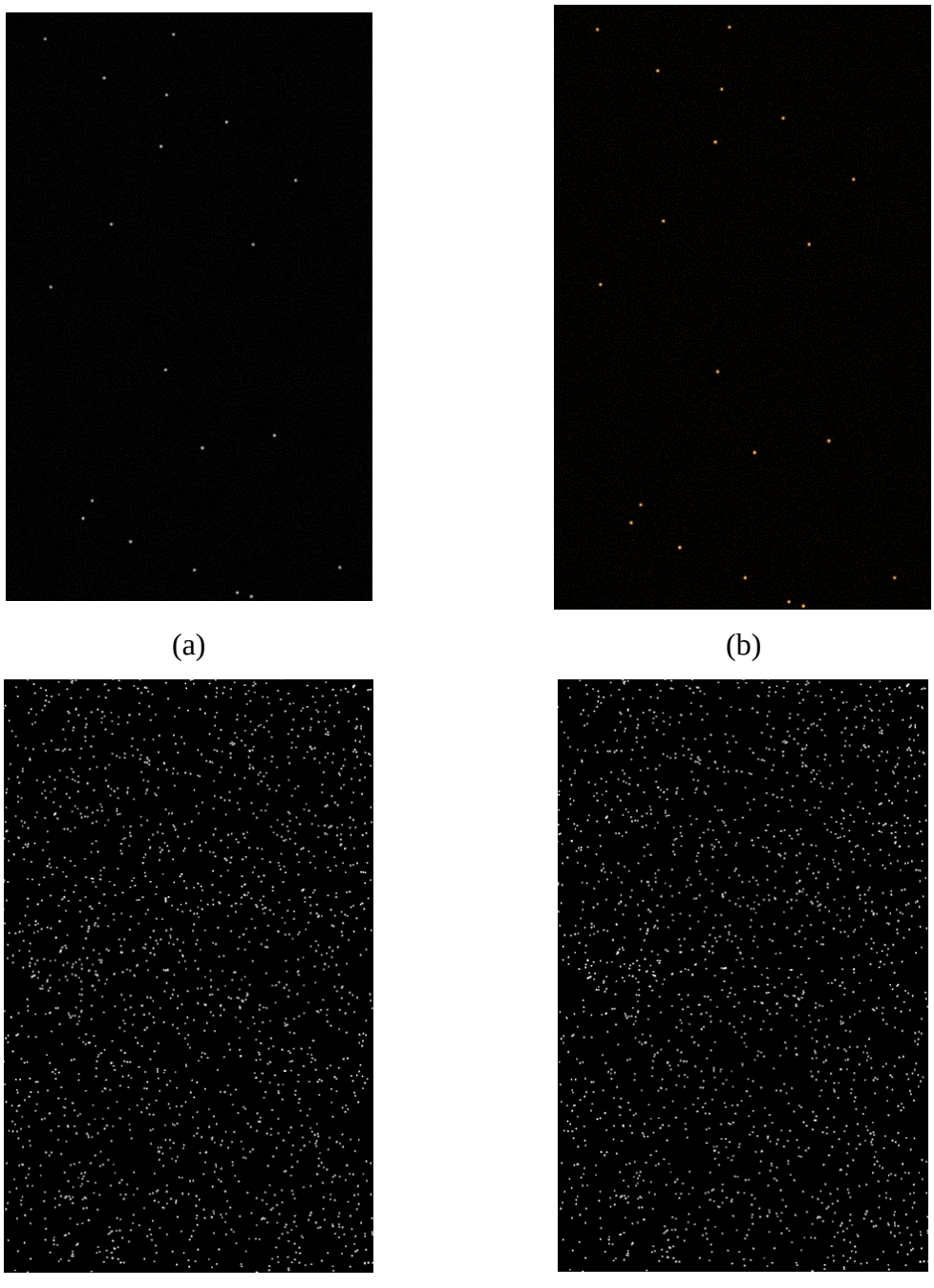

(a) (b)

(c) (d)

Figure 4.1. Images of 586 pixels x 939 pixels. Images a) and b) contain 20 artificial particles. Images c) – d) contain 2000 particles

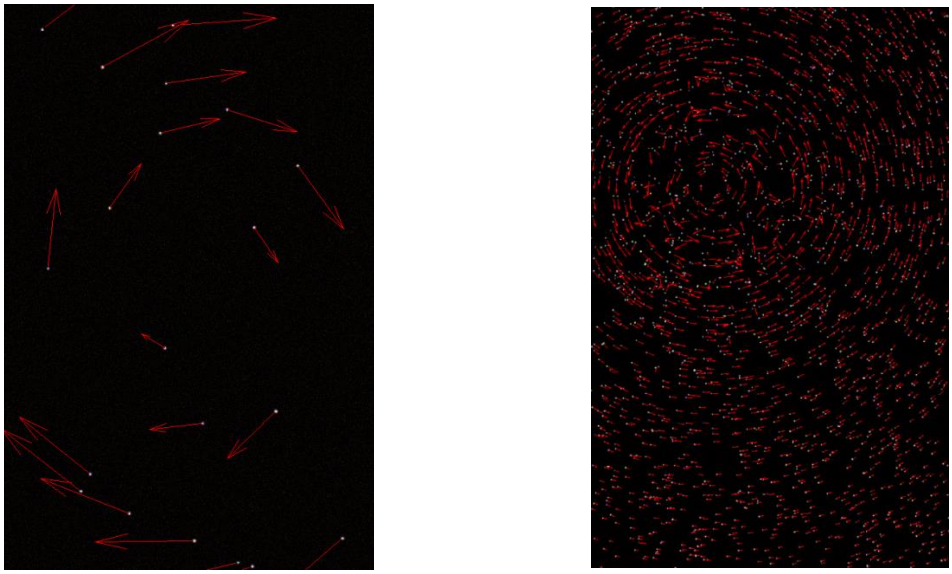

(a) (b)

Figure 4.2. Plotted vectors for: (a) 20 artificial particles with 5 pixel displacement and (b) 2000 particles with 10 pixel displacement

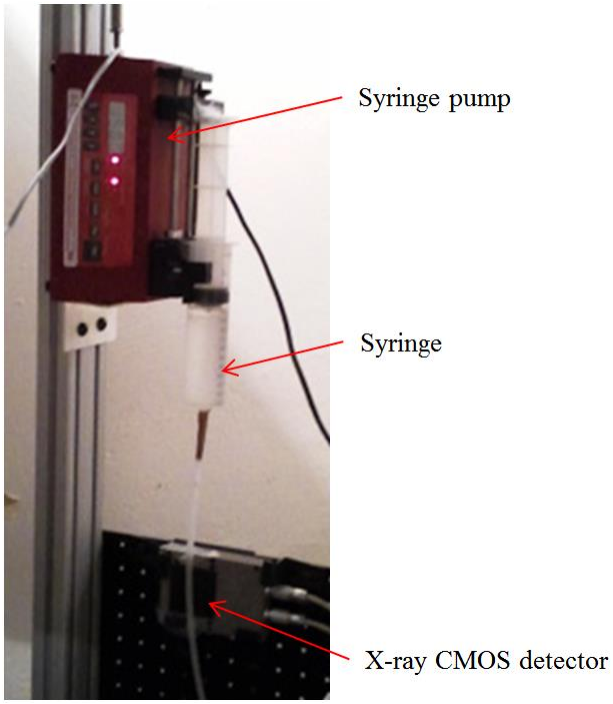

Figure 4.3. Syringe containing liquid-tracer particle mixture, syringe pump, and X-ray CMOS detector

Figure 4.4 is an image of the obtained particle path line that traveled with the liquid, inside an empty tube. The color bar indicates the scale of the particle velocity (which was expected to resemble the travelling liquid velocity). The measured velocity suggests that the proposed procedure produces a difference (either increased or decreased) between the measured velocity and the superficial liquid velocity of at most 16.7% (maximum).

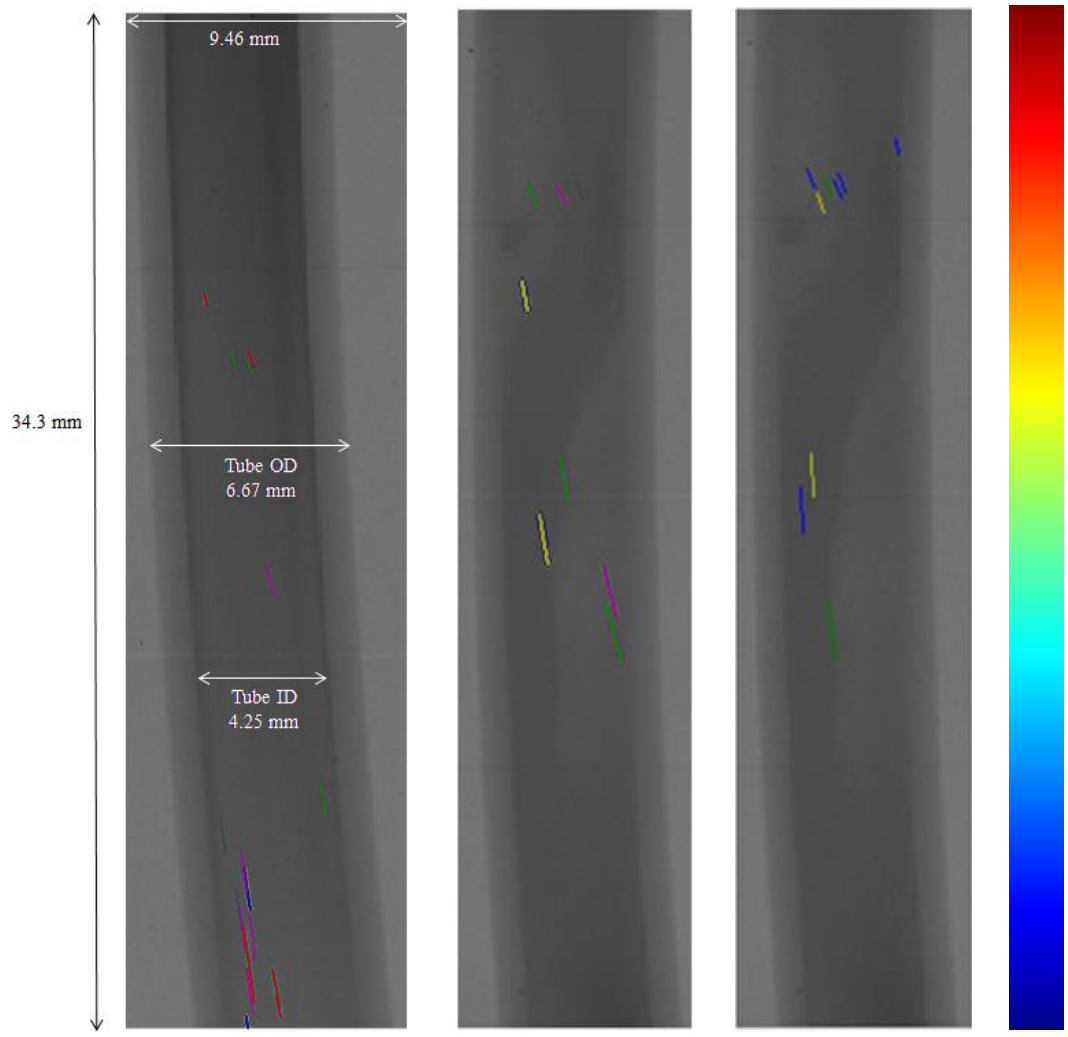

(a) (b) (c)

Figure 4.4. Three replications of measured velocity [cm/s] inside the tube. (a) 0.049 – 0.067, (b) 0.052 – 0.064, and (c) 0.048 – 0.067

Figure 4.5 shows the frequency distribution of the measured particle velocity inside the tube. All radiation exposure works were performed in the Missouri University of Science & Technology Reactor (MSTR). Table 4.1 simplified the measured result with the superficial liquid velocity.

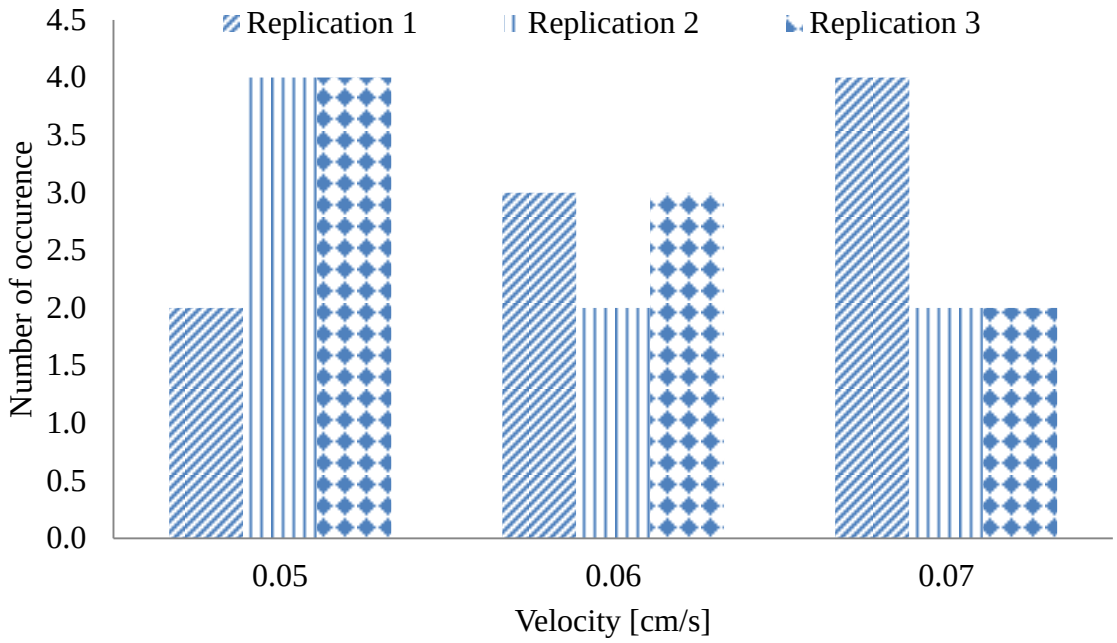

Figure 4.5. Number of occurrence of the measured velocity for all replications (T_{test}) with V_{SL} = 0.06 ± 1% cm/s

Table 4.1. Measured results from three replications

Superficial liquid velocity (cm/s)	Replication	Measured liquid velocity range (cm/s)
0.059 ± 1%	a	0.049 – 0.067
	b	0.052 – 0.064
	c	0.048 – 0.067

4.3. TWO-POINT OPTICAL PROBE FOR LIQUID VELOCITY ($V_{LL|OPT}$) MEASUREMENT

The concept of a two-point probe was applied to measure both bubble velocity and bubble behavior in a multiphase system (Park, et al., 1969; Rigby, et al., 1970). Wu & Ishii (1999) sucessfully used this probe to measure the local interfacial area concentration within a bubbly flow. Magaud et al. (2001) used the dual optical probe technique to detect the local, instantaneous presence of either a liquid or a gas inside a rectangular-type gas-liquid bed.

Conceptually, the measurement technique that uses an optical probe was successfully used to measure the bubble dynamics of a bubble column at Washington University in Saint Louis and Missouri University of Science and Technology (Xue, 2004; Xue, et al., 2008; Kagumba, 2013). The probe has never been used to measure the V_{LL} inside TBRs.

At Missouri University of Science and Technology and part of other PhD dissertation (Abdul Rahman, 2014), two point optical fiber probe has been developed to measure, for the first time, local liquid and gas velocities, their holdup, and their related time series functions.

In this work, the new optical fiber probe technique has been used to compare its measurement with the measured values of V_{LL} using our newly developed technique (combination of DIR and PTV). This is considered as additional assessment or validation to what has been discussed earlier (Section 4.1 and Section 4.2).

The two point optical probe technique for liquid velocity measurement has been developed based on changes in the refractive index of the medium located at the optical probe tip. The two-point optical probe consists of two tips. Each tip is separated with a known distance. The liquid velocity is calculated by dividing the distance between the two tips by the time interval that the liquid takes to pass the two tips.

The probe was manufactured at Missouri University of Science and Technology (Missouri S&T). A 680 nm wave length of light emitted by a Laser Emitting Diode (LED) was transmitted through standard glass fiber connectors and detected by a photodiode.

The validation of newly developed technique (combination of DIR and PTV) with two-point fiber optical probe will mutually validate the measurements of the optical probe in packed beds (Abdul Rahman, 2014).

4.3.1. Flow Pattern Identification. The first steps taken to use two-point optical probe measurement as a validation technique was to identify the flow pattern and measure the V_{LL} of the test bed. In order to that, the new developed combination of particle tracking and DIR technique was applied.

A two-inch diameter test bed with optical probe ports was used in this experiment. This bed was packed with 3 mm EPS beads. The same tracking material outlined in Section 3.3 was used to both visualize and track the flow. The particle identification and algorithm that was successfully used in Section 4.1 and Section 4.2, respectively, was repeated in this experiment, shown in Figure 4.7. The superficial liquid and gas velocities used in this experiment were 0.3 cm/s and 5.2 cm/s, respectively.

The location of the optical probe ports used to measure $V_{LL|OPT}$ was divided into 3 sections. The sections were according to the bed height (Z) and bed diameter (D) ratio (Z/D). These sections (illustrated in Figure 4.6) were Z/D = 3.3, 3.9, and 4.5.

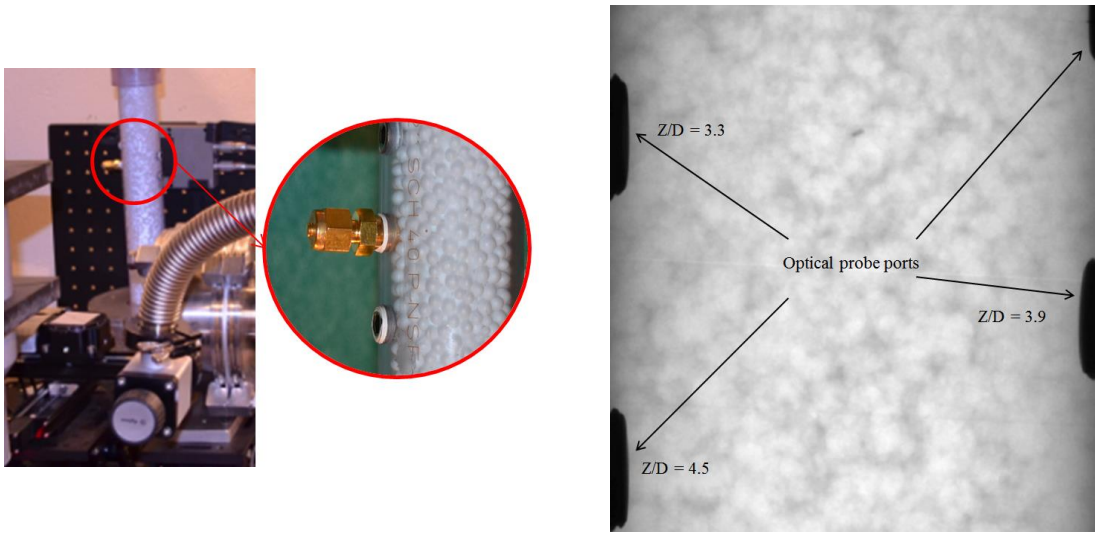

(a) (b)

Figure 4.6. The two-inch TBR setup with (a) fiber optic probe port, and (b) radiographic image with optical probe port located at each Z/D

The sections from three different Z/D were divided into 3 smaller sections. These sections were used to position the tip of the optical probe. The center of the smaller sections (indicated by a blue dashed circle in Figure 4.8) was marked to indicate the location of the optical probe measurement points. Figure 4.9 shows histograms of measured V_{LL} with the DIR ($V_{LL|DIR}$).

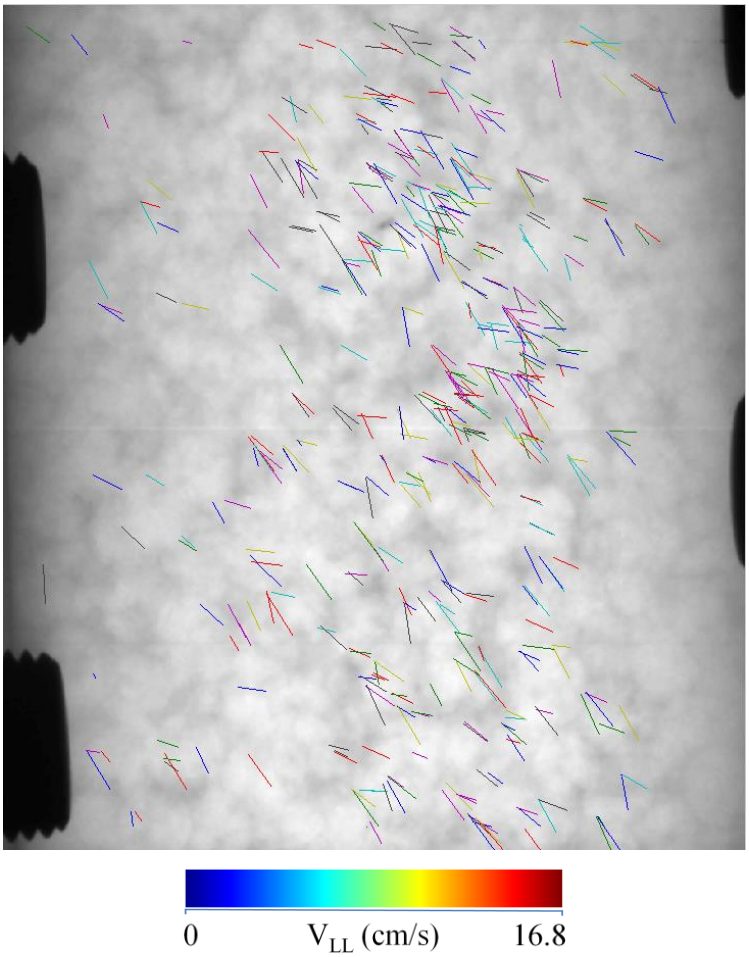

Figure 4.7. Flow patterns that were successfully tracked with the combined technique. The color bar indicates the range of obtained V_{LL}

Table 4.2 list the mean, standard deviation (σ), and variance of measured $V_{LL|DIR}$ in a two-inch TBR (inside the blue dashed circle).

4.3.2. Two Point Optical Probe Measurement ($V_{LL|OPT}$). The optical probe used in this study (see Figure 4.10) was an advanced version of the probe originally developed and employed by Frijlink (1987) at the Technical University of Delft in the Netherlands (Kagumba, 2013).

The advanced probe consisted of two tips each with the same length and diameter. Each fiber consisted of three layers: a quartz glass core having a refraction index of 1.45 and a diameter of 200 μm, a silicon cladding that increased the diameter to 380 μm, and a further protective layer of Teflon, increasing the overall diameter to 600 μm.

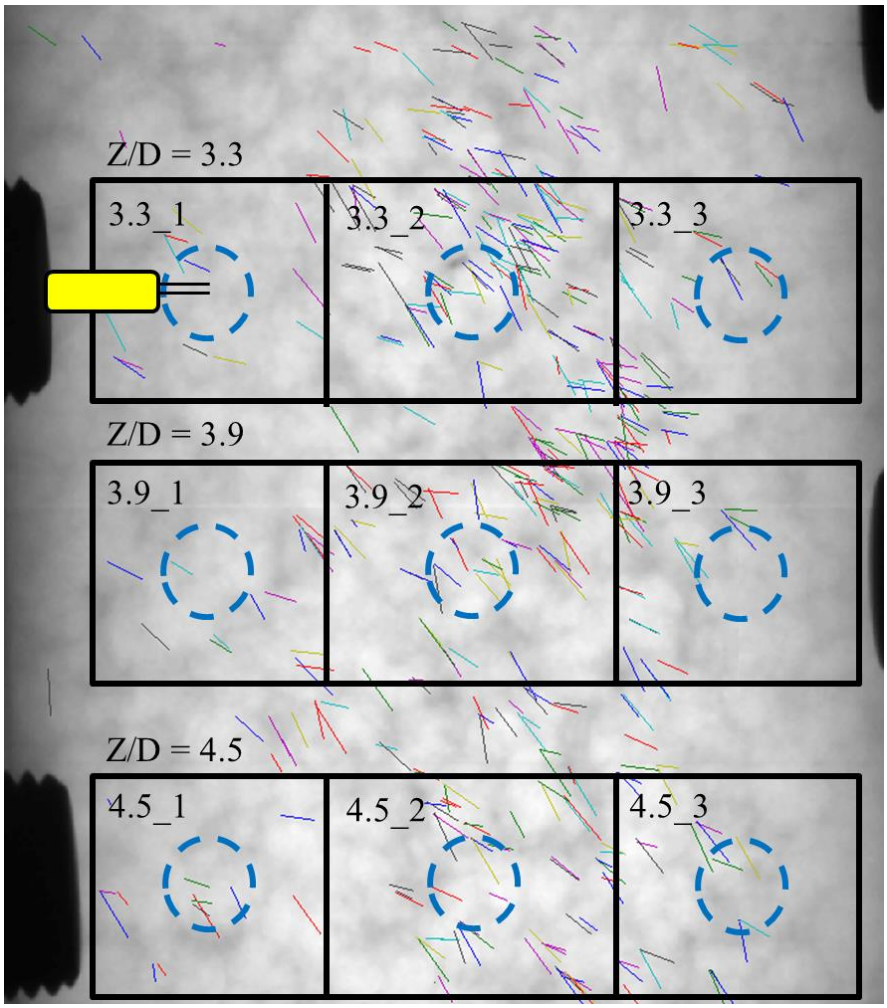

Figure 4.8. Localized position for the optical probe (blue dashed circle)

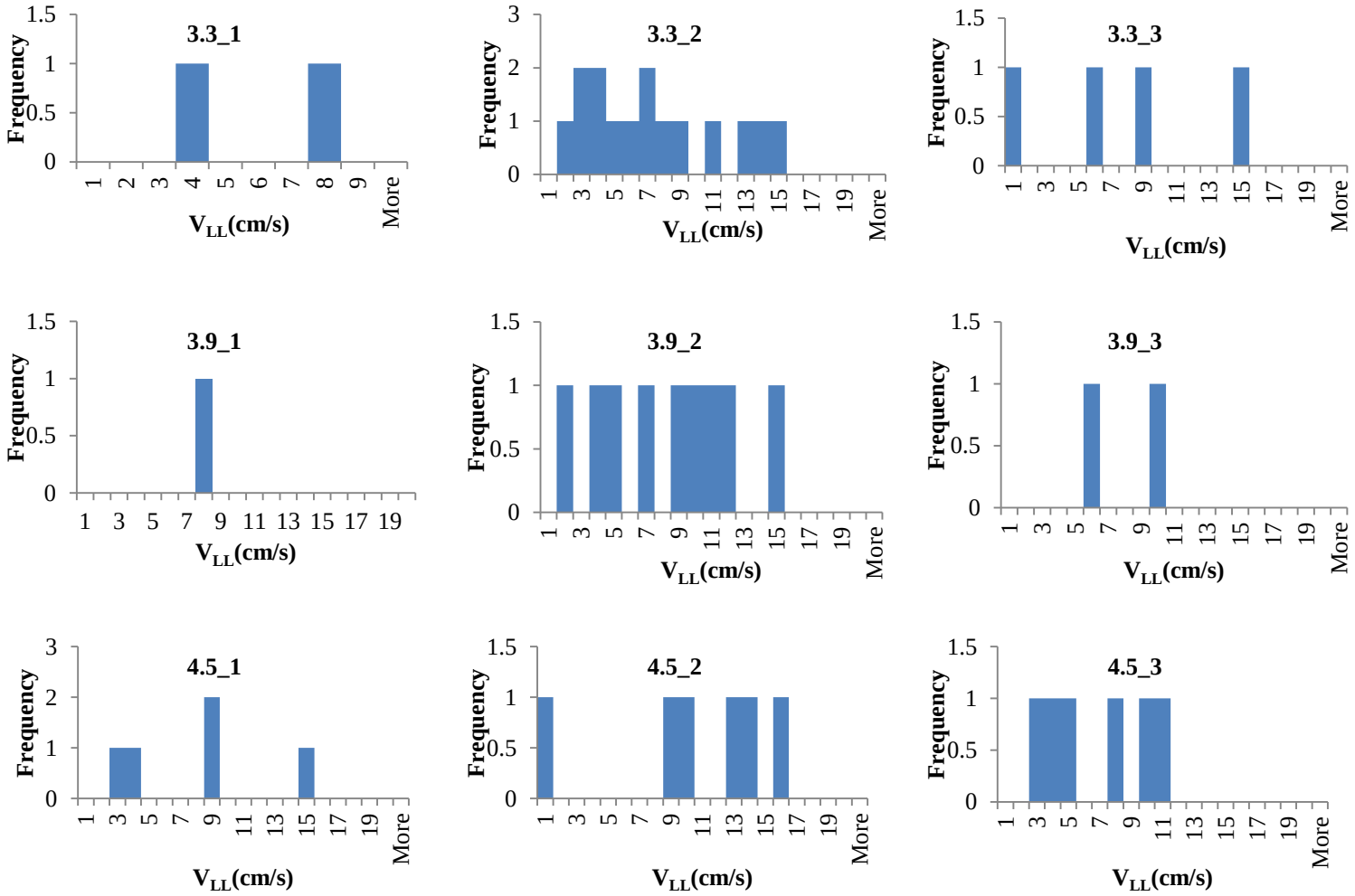

Figure 4.9. Histograms of measured $V_{LL|DIR}$ for each corresponding, localized position (dashed blue circle) listed in Figure 4.8

Table 4.2. The mean, standard deviation (σ), and variance of measured $V_{LL|DIR}$ in a two-inch TBR (inside the blue dashed circle)

Location (blue dashed circle)	Mean	σ	Variance
Z/D = 3.3			
3.3_1	5.49	1.64	2.67
3.3_2	6.97	4.05	16.4
3.3_3	7.46	5.27	27.8
Z/D = 3.9			
3.9_1	8.12	0	0
3.9_2	8.04	4.08	16.7
3.9_3	7.85	1.97	3.86
Z/D = 4.5			
4.5_1	7.45	4.6	21.2
4.5_2	9.98	5.06	25.6
4.5_3	6.39	2.97	8.82

The entire probe was manufactured in the chemical engineering laboratory at Missouri University of Science and Technology (Missouri S&T). Standard glass fiber connectors were used to send a wavelength of 680 nm through a Laser Emitting Diode (LED). This wavelength was then detected by a photodiode.

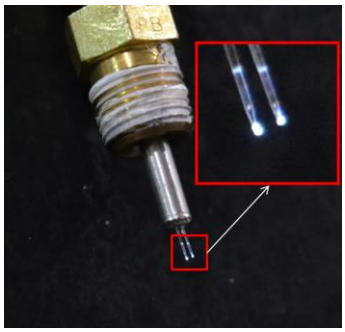

Figure 4.10. The fiber optical probe used in this experiment

According to Kagumba (2013), due to the difference in refractive index between liquid and the gas phase, when the fiber tip is in a liquid medium, most of the light is refracted into the liquid and very little light is sent back up the fiber. However, when the tip is in the gas bubble, most of the light is reflected, travelling back into the coupler. This coupler then channeled approximately 50% of the reflected light into a photodiode, which finally transformed the light photons into a voltage.

The voltage signals (see Figure 4.11) were collected by a data acquisition board (PowerDAQ PD2- MFS-8-1M/12) at a sampling frequency of 40 kHz. The data acquisition board was purchased from United Electronics Industries.

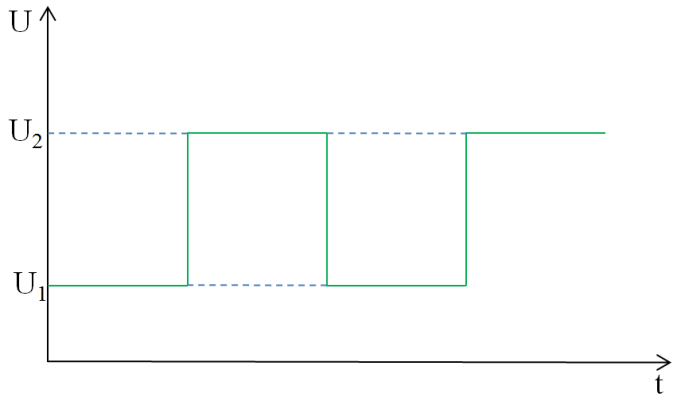

Figure 4.11. Time series of a single fiber (U_1 – liquid phase and U_2 – gas phase) (Meitzner, 2011)

If the liquid is assumed to be constantly flowing in a stable state, the liquid velocity ($V_{LL|OPT}$) can be calculated as

$$V_{LL|OPT} = L/\Delta t \tag{31}$$

where L is the distance between two fiber optics and Δt is the time taken by the liquid to hit fiber optic 1 and fiber optic 2 (see Figure 4.12).

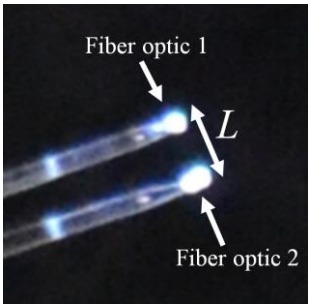

Figure 4.12. The distance, *L* between fiber optic 1 and fiber optic 2

4.3.3. Local Liquid Velocity Result With Optical Probe ($V_{LL\ |OPT}$). The optical probe was successfully used to measure the local liquid velocity ($V_{LL|OPT}$) inside the two inch TBR and the other performed work (Abdul Rahman, 2014).

The length of the fiber optic probe was carefully measured before it was placed in approximately, the center of the blue dashed circle. Based on the measured $V_{LL|DIR}$, the tracked liquid is assumed to be the same liquid that hit the fiber optic probe.

The superficial liquid and gas velocities used in this experiment were the same as that used in Section 4.3.1. Table 4.3 tabulates the measured $V_{LL|OPT}$. Three replications were made in every location for proper sampling. Table 4.4 lists the basic statistical analysis performed on the measured $V_{LL|OPT}$.

Table 4.3. Average local liquid velocity measured with an optical probe ($V_{LL|OPT}$) at different Z/D levels

Z/D	Position								
	1			2			3		
	$V_{LL\text{-}Avg}$ (cm/s)								
	Rep 1	Rep 2	Rep 3	Rep 1	Rep 2	Rep 3	Rep 1	Rep 2	Rep 3
3.3	7.55	7.35	7.1	9.3	8.9	8.95	8.7	8.55	8.25
3.9	6.7	6.7	6.45	8.65	8.7	9.35	8.45	8.6	8.25
4.5	8.35	8.1	7.75	6.4	6.9	6.45	8.1	8.05	7.95

Table 4.4. The mean, standard deviation (σ), and variance of measured $V_{LL|OPT}$ in a two-inch TBR (inside the blue dashed circle)

Location	Mean (cm/s)	σ	Variance
Z/D = 3.3			
3.3_1	7.33	0.18	0.03
3.3_2	9.05	0.18	0.03
3.3_3	8.50	0.19	0.03
Z/D = 3.9			
3.9_1	6.62	0.12	0.01
3.9_2	8.90	0.32	0.10
3.9_3	8.43	0.14	0.02
Z/D = 4.5			
4.5_1	8.07	0.25	0.06
4.5_2	6.58	0.22	0.05
4.5_3	8.03	0.06	0.00

4.3.4. Hypothesis Test (*t*-test With *p*-value < 0.05). Both measurement results were tested with statistical analysis (*t*-test) to determine their significance levels.

The *t*-test or Student's *t*-test (Wilcox, 2012), equivalent to one-way analysis of variance (ANOVA) with two groups, is a statistical tool to test the difference between means, involving a comparison of a test statistic to the *t* distribution (*t*-value) to determine the probability of that statistic (*p*-value) if the study's null hypothesis (H_o) is true (Boslaugh, 2012; Cabral & Rangayyan, 2012). Conversely, the other hypothesis is known as the alternative hypothesis (H_a).

The H_o is either the subject or the technique being referred to or compared to when a new technique is tested. It is a statistical hypothesis that is tested for possible rejection under the assumption that either it is true or it (typically) corresponds to either a general or a default position (Cabral & Rangayyan, 2012).

The *p*-value is often chosen by its significance level (α). If the *p*-value is smaller than α ($p < \alpha$), the H_o can be rejected at the α% significance level. A smaller *p*-

value provides convincing evidence that H_o is false. A *p*-value larger α, does not provide enough statistical evidence to reject H_o, it means that there is no enough difference within the samples to conclude a difference (samples are from the same group).

Conventionally, the *p*-value is set to be less than 0.05 (α = 0.05) driving the H_a to a statistically significant confidence level of 95% (Albright, et al., 2006).

In this validation procedure, the H_o is treated as $V_{LL|OPT}$ while the $V_{LL|DIR}$ as $H_{a.}$ Statistical analysis software (SAS) was used to perform a *t*-test on both results ($V_{LL|OPT}$ and $V_{LL|DIR}$).

The results collected from this *t*-Test result are listed in Table 4.5 (with $p < 0.05$ to reject H_o). They suggest that H_o cannot be rejected for most of the measured values when $p < 0.05$. They also reveal an insignificant trend between the measured $V_{LL|OPT}$ and $V_{LL|DIR}$. Of the nine measured locations, only location 3.9_1 was found to have $p < 0.05$. This occurred primarily because only one tracked particle was present in the blue dashed circle. Thus not enough information was gathered to generate more statistical data.

Results in Table 4.5 suggest that, through hypothesis testing, the measured $V_{LL|DIR}$ had more than a 5% chance categorized in the $V_{LL|OPT}$ group.

4.4. COMPARISON OF MEASURED $V_{LL|DIR}$ AND $V_{LL|OPT}$ WITH THE TURTOSITY OF FIXED BED

In order to have better accuracy of measured $V_{LL|DIR,}$ a rejection criterion is established based on the concept of tortuosity (τ). The τ highlighted in Section 2.3, gives the actual length (L_ε) of the streamline over the measured length of the streamline (L_{meas}). The τ values from 1.38 to 1.71 (see Figure 4.13) were chosen based on the previous comparison made by Lanfrey et al. (2010) and the porosity values of this work (0.38), highlighted in Section 3.1.1. Assuming that the liquid is moving on the uniform spherical bead of radius *R* that packed the bed with an angle of β and ε is 0.38, the τ can traditionally is defined as (Lanfrey, et al., 2010; Comiti & Renaud, 1989)

$$\tau = L_\varepsilon / \mathrm{R} \tag{32}$$

where L_ε is the actual length traveled by the liquid. The calculated actual length, L_ε travelled by the liquid around the constant spherical shape of the packing with radius R, is tabulated in Table 4.6. The velocity in accordance to the chosen τ (Vτ) was calculated based on the frame rate of the CMOS detector. Based on the L_ε, the liquids travelled from 2.07 mm to 2.57 mm, not more than one diameter size of the packing beads i.e. 3 mm. The calculated Vτ suggested that the liquid would not travelled more than 0.7 cm/s.

Table 4.5. Comparison between the mean, standard deviation (σ), variance, degree of freedom (*df*), *t*-value, and *p*-value (α level 0.05) generated by SAS between the measured $V_{LL|OPT}$ and $V_{LL|DIR}$ in a two-inch TBR

	$V_{LL\|OPT}$			$V_{LL\|DIR}$			*t*-Test		
Location	Mean (cm/s)	σ	Variance	Mean (cm/s)	σ	Variance	*df*	*t*	*p*
Z/D = 3.3									
3.3_1	7.33	0.18	0.03	5.49	1.64	2.67	3	1.5	0.23
3.3_2	9.05	0.18	0.03	6.97	4.05	16.4	16	0.84	0.41
3.3_3	8.50	0.19	0.03	7.46	5.27	27.8	5	0.29	0.78
Z/D = 3.9									
3.9_1	6.62	0.12	0.01	8.12	0	0	2	9.02	0.01
3.9_2	8.90	0.32	0.10	8.04	4.08	16.7	10	0.33	0.75
3.9_3	8.43	0.14	0.02	7.85	1.97	3.86	6	0.2	0.85
Z/D = 4.5									
4.5_1	8.07	0.25	0.06	7.45	4.6	21.2	3	0.4	0.72
4.5_2	6.58	0.22	0.05	9.98	5.06	25.6	7	1.02	0.34
4.5_3	8.03	0.06	0.00	6.39	2.97	8.82	7	0.84	0.43

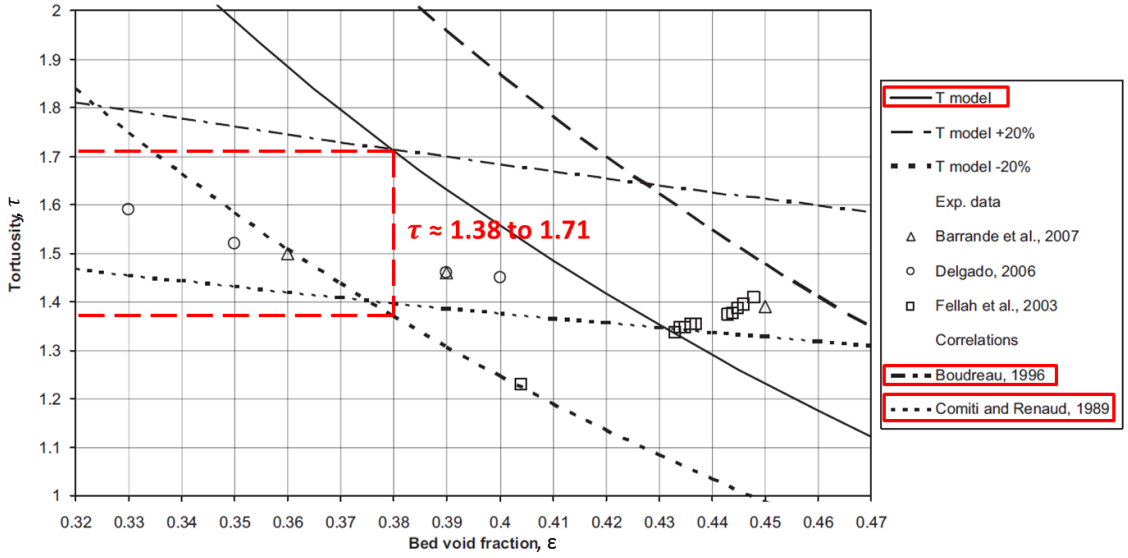

Figure 4.13. Range of τ used to compare the obtained tracer particles path length with correlations and obtained models (Lanfrey, et al., 2010)

Table 4.6. The actual length, L_ε travelled by the liquid in packed bed with ε = 0.38 and R = 1.5 mm

Tortuosity, τ	Porosity, ε	Particle radius, R (mm)	L_ε (mm)	V_τ (cm/s)
1.38	0.38	1.5	2.07	0.56
1.4			2.1	0.57
1.5			2.25	0.61
1.6			2.4	0.65
1.71			2.57	0.69

Figure 4.14 to Figure 4.16 depicts the comparisons between $V_{LL|DIR}$, $V_{LL|OPT}$, $V_{\tau=1.38}$ and $V_{\tau=1.71}$ for three different Z/D (3.3, 3.9 and 4.5). By comparing the percentage difference between the Vτ (either τ=1.38 or τ=1.71) and individually obtained $V_{LL|DIR}$ and $V_{LL|OPT}$ (Section 4.3.4), it shows that none of the techniques, either DIR or optical fiber probe, have closer values to the Vτ. The existence of V_{SL} and V_{SG} has changed the number of τ by introducing the gas flow inertia that induced the liquid film curvature (Boyer & Fanget, 2002; Narasimhan, et al., 2002).

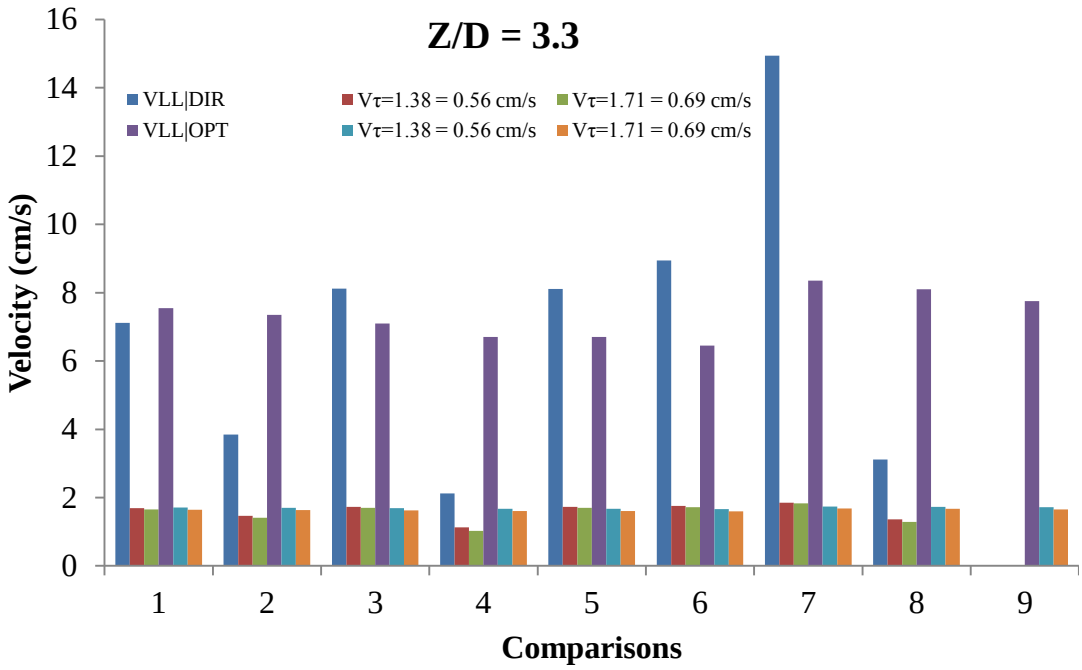

Figure 4.14. Comparisons between $V_{LL|DIR}$ and $V_{LL|OPT}$ with $V_{\tau=1.38}$ and $V_{\tau=1.71}$ for Z/D = 3.3

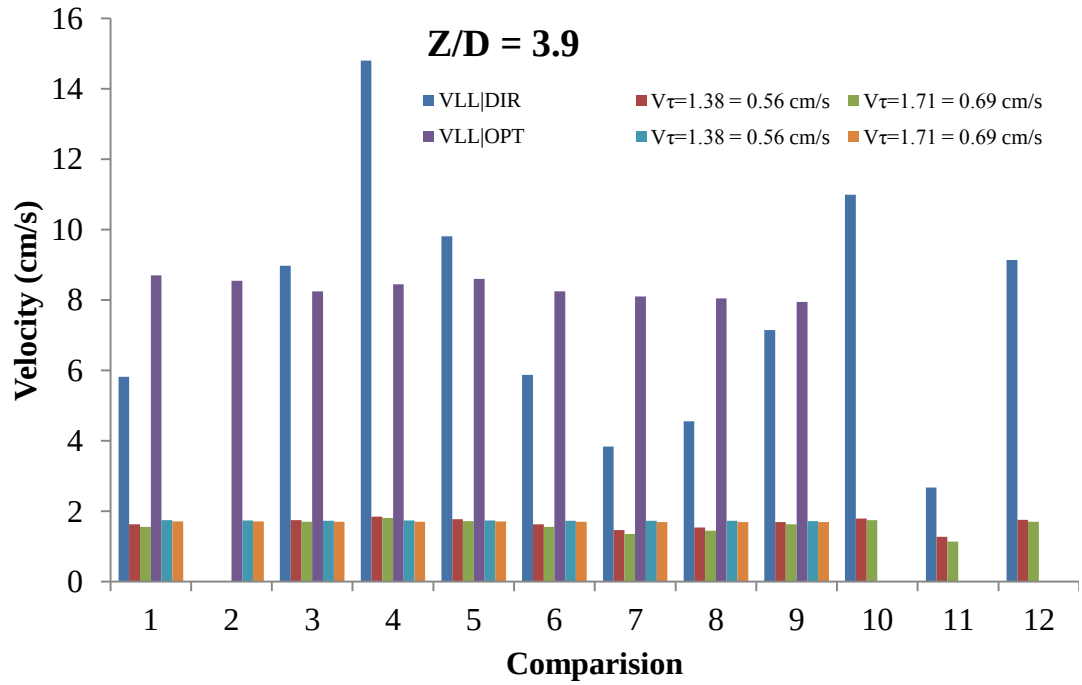

Figure 4.15. Comparisons between $V_{LL|DIR}$ and $V_{LL|OPT}$ with $V_{\tau=1.38}$ and $V_{\tau=1.71}$ for Z/D = 3.9

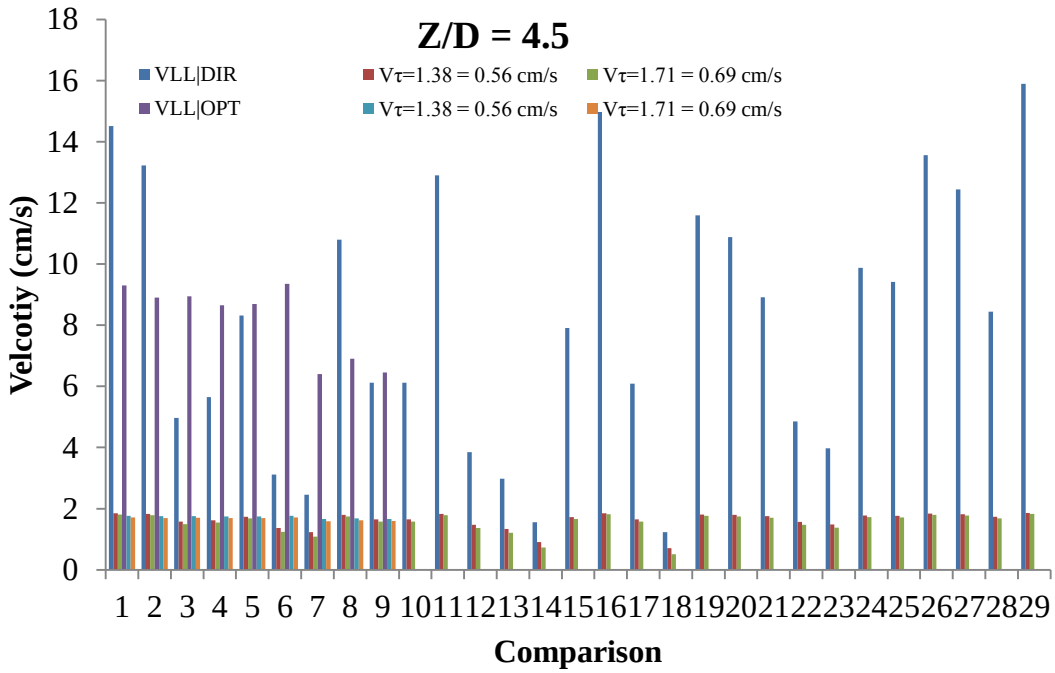

Figure 4.16. Comparisons between $V_{LL|DIR}$ and $V_{LL|OPT}$ with $V_{\tau=1.38}$ and $V_{\tau=1.71}$ for Z/D = 4.5

5. RESULTS FOR PARTICLE TRACKING VELOCIMETRY USING DIR

5.1. MEASURED LOCAL LIQUID VELOCITY (V_{LL})

5.1.1. Tube With a 22.5 mm Diameter. Figures 5.1 to 5.3 illustrate the 2D path of the tracing particles that represent the trickling liquid. The path lines are plotted on top of the original X-ray image taken of the TBR.

The bed was operated at a V_{SL} of 0.42 ± 2% cm/s (Figure 5.1), 0.84 ± 2% cm/s (Figure 5.2), and 1.11 ± 2% cm/s (Figure 5.3). Four replications were completed with fresh packing for every V_{SL} and any outliers were removed using one sigma test. Each of these figures illustrates both the random movements and the frequency distributions of the local liquid velocities, for all particles, in each replication. In several places, the particles moved at a higher speed; in others, movement was static. As the V_{SL} increased, the maximum measured V_{LL} also increased. All replications displayed a limit on the maximum ($V_{LL\text{-}Max}$) values for every $V_{SL.}$ Table 5.1 lists the maximum measured velocity of each V_{SL}. The $V_{LL\text{-}Max}$ was approximately 1.7 – 1.9 times higher when V_{SL} = 0.42 ± 2% cm/s. It was approximately 3.6 – 4.0 times higher when V_{SL} = 0.84 ± 2% cm/s. The $V_{LL\text{-}Max}$ was approximately 4.3 – 4.8 times higher when V_{SL} = 1.11 ± 2% cm/s.

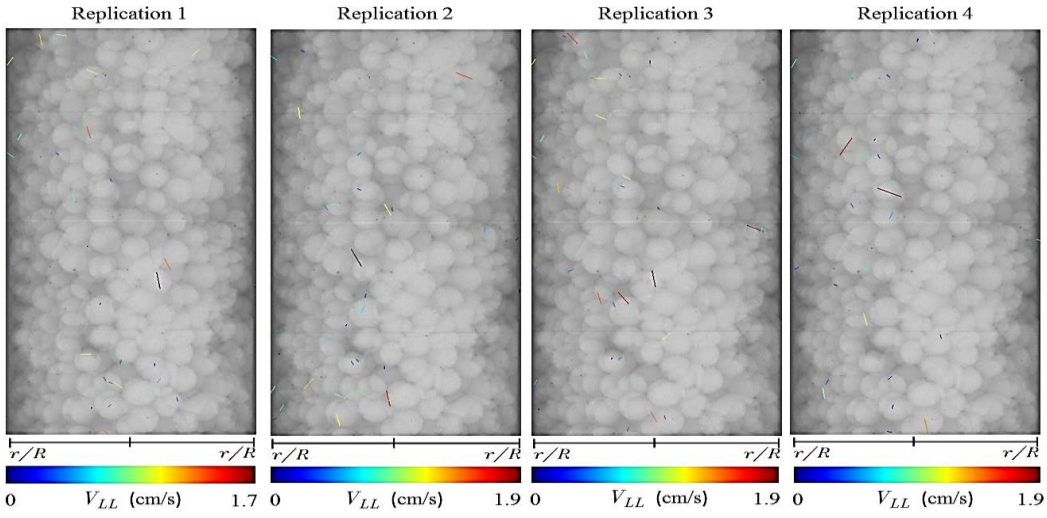

Figure 5.1. The identified 2D particle paths, V_{LL} in every replication, and color bars for V_{SL} = 0.42 ± 2% cm/s

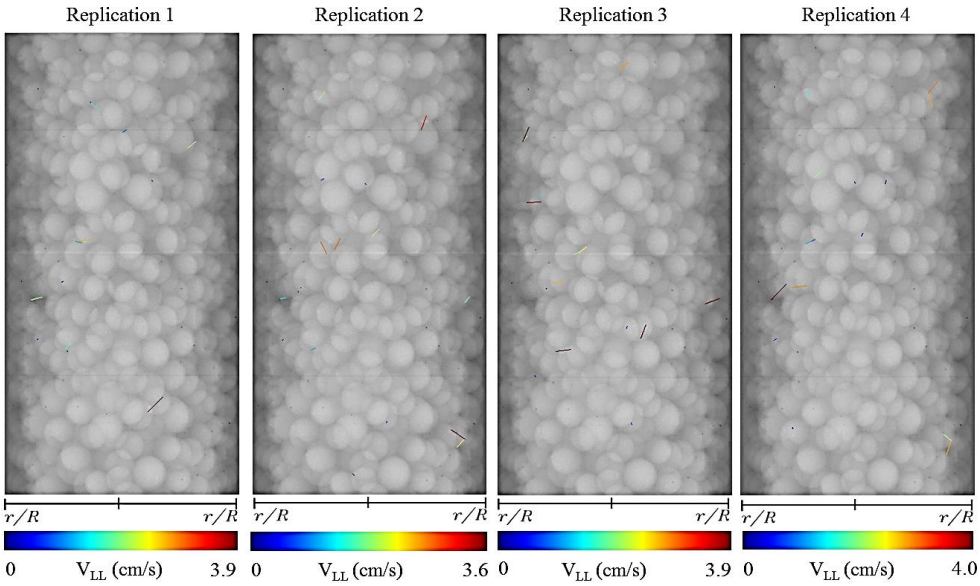

Figure 5.2. The identified 2D particle paths, V_{LL} in every replication, and color bars for V_{SL} = 0.84 ± 2% cm/s

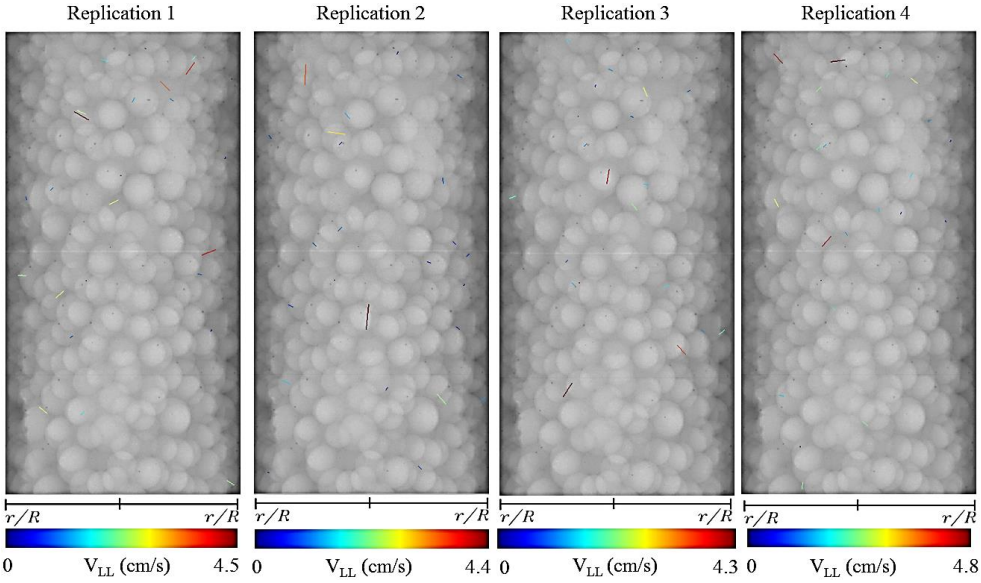

Figure 5.3. The identified 2D particle paths, V_{LL} in every replication, and color bars for V_{SL} = 1.11 ± 2% cm/s

Figures 5.4 to 5.6 illustrates the histogram of measured V_{LL} inside the tube with 22.5 cm diameter, with all the replications (Rep.).

Table 5.1. Maximum measured local liquid velocity ($V_{LL\text{-}Max}$) for a 22.5 mm diameter tube

Phase	Superficial liquid velocity (V_{SL}) (± 2% cm/s)	Superficial gas velocity (V_{SG}) (± 2% cm/s)	Maximum measured local liquid velocity ($V_{LL\text{-}Max}$) (cm/s)			
			1	2	3	4
Single	0.42	No gas	1.7	1.9	1.9	1.9
	0.84		3.9	3.6	3.9	4.0
	1.11		4.5	4.4	4.3	4.8

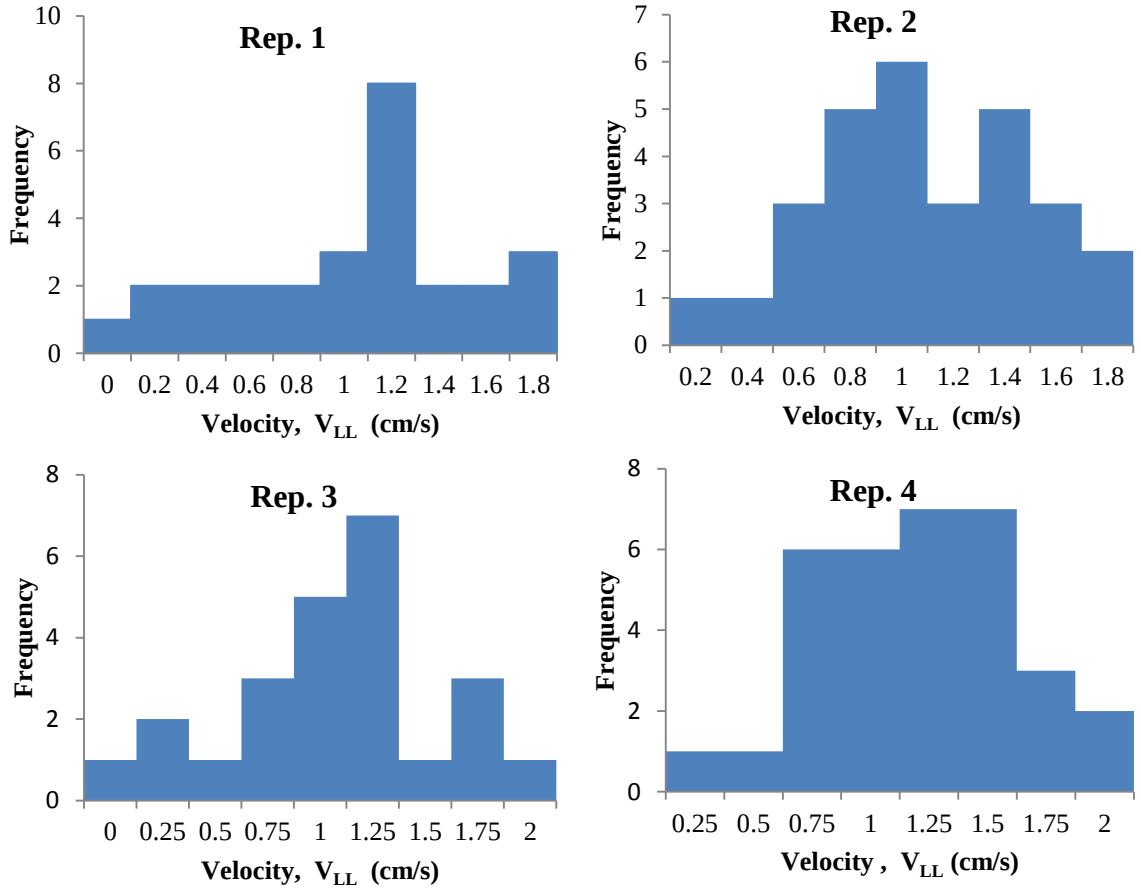

Figure 5.4. Histogram of $V_{LL,}$ in every replication, for V_{SL} = 0.42 ± 2% cm/s

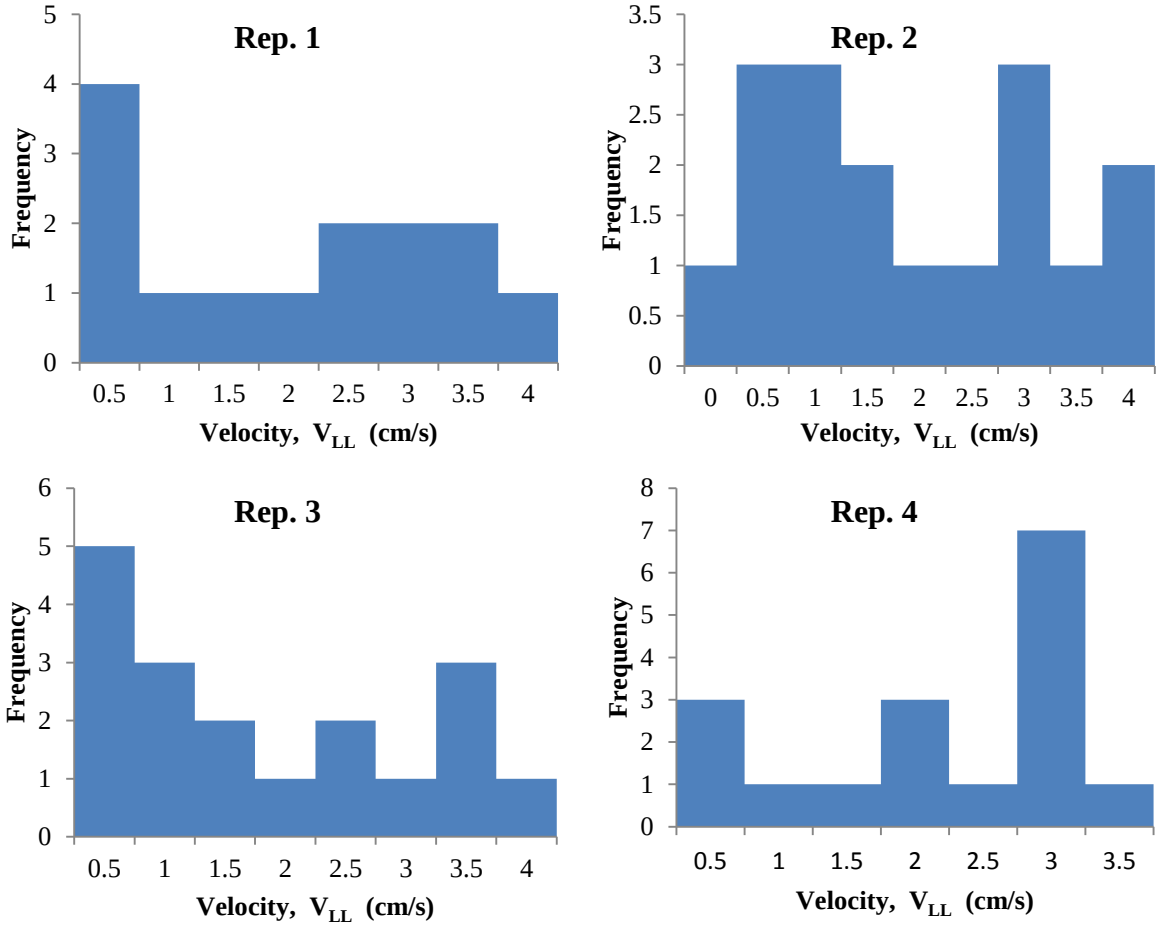

Figure 5.5. Histogram of $V_{LL,}$ in every replication, for V_{SL} = 0.84 ± 2% cm/s

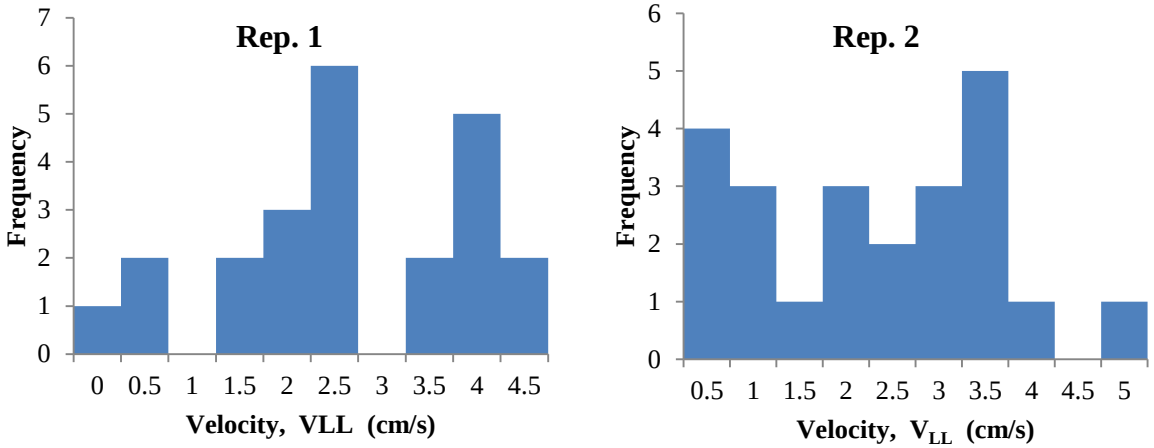

Figure 5.6. Histogram of $V_{LL,}$ in every replication, for V_{SL} = 1.11 ± 2% cm/s

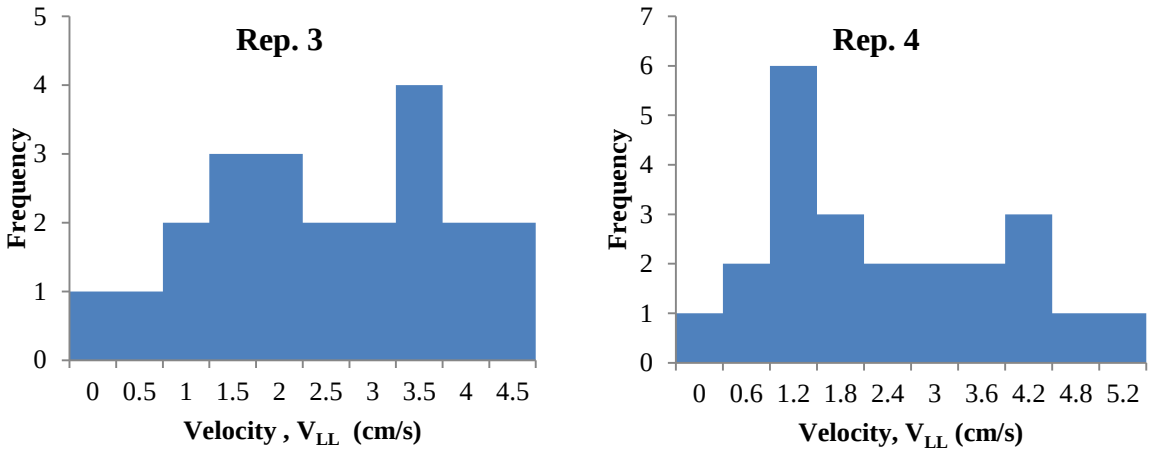

Figure 5.6. Histogram of $V_{LL,}$ in every replication, for V_{SL} = 1.11 ± 2% cm/s (Cont.)

5.1.2. Tube With a 40 mm Diameter (Constant V_{SG} = 1.05 ± 2% cm/s). Figures 5.7 – 5.9 illustrate the 2D path of the tracing particles that represent the trickling liquid. The path lines are plotted on top of the original TBR X-ray image.

The bed was operated at a V_{SL} of 0.13 ± 2% cm/s (Figure 5.7), 0.27 cm/s ± 2% (Figure 5.8), and 0.39 cm/s ± 2% (Figure 5.9). Four replications were completed with fresh packing for every V_{SL} and outliers were removed using one sigma test. As in Section 5.1.1, all figures illustrate both the random movements and the frequency distributions of the local liquid velocities, for all particles, in each replication. In several places, the particles moved at a higher speed; in others, movement was static. As the V_{SL} increased, the maximum measured V_{LL} also increased. All replications displayed a limit on the maximum ($V_{LL\text{-}Max}$) values for every $V_{SL.}$ Figures 5.10 – 5.12 are histograms of the measured V_{LL} inside the tube with a 40 cm diameter, with all the replications (Rep.).

Table 5.2 lists the maximum measured velocity of each V_{SL}. The $V_{LL\text{-}Max}$ was approximately 48 - 51 times higher for V_{SL} = 0.13 ± 2% cm/s. It was approximately 30 - 35 times higher for V_{SL} = 0.27 ± 2% cm/s. The $V_{LL\text{-}Max}$ was approximately 35.5 - 39.8 times higher for V_{SL} = 0.39 ± 2% cm/s.

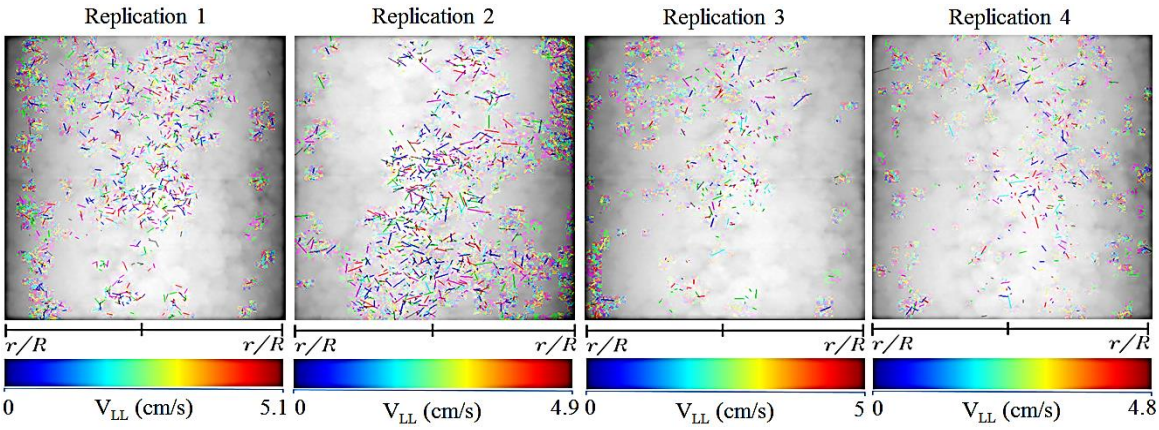

Figure 5.7. The identified 2D particle path, V_{LL} in every replication, and color bars for V_{SL} = 0.13 ± 2% cm/s

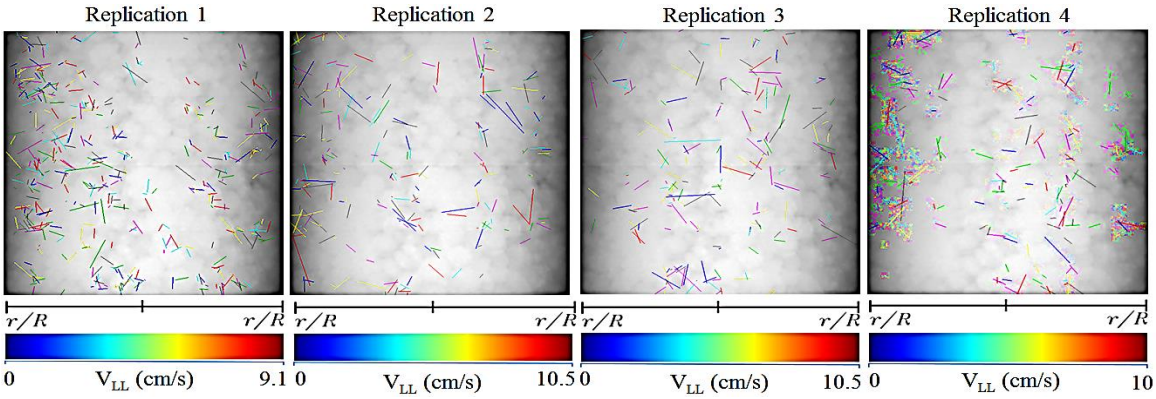

Figure 5.8. The identified 2D particle path, V_{LL} in every replication, and color bars for V_{SL} = 0.27 ± 2% cm/s

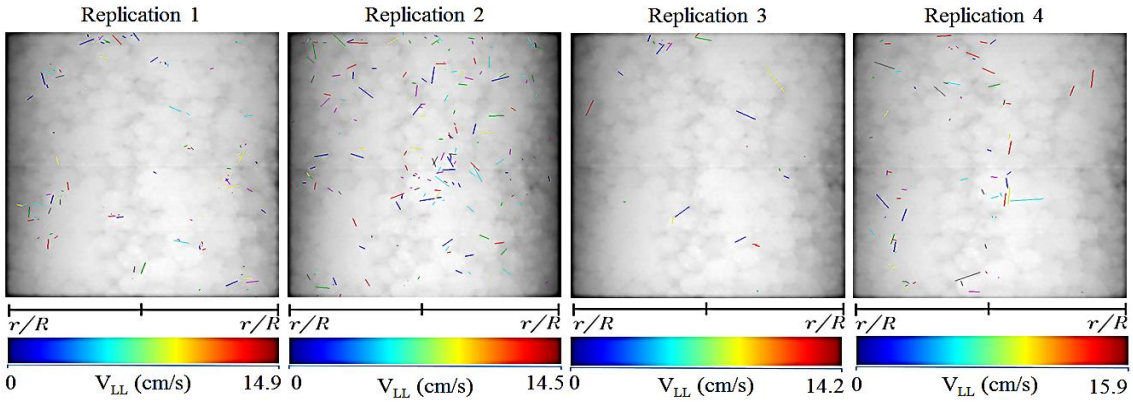

Figure 5.9. The identified 2D particle path, V_{LL} in every replication, and color bars for V_{SL} = 0.39 ± 2% cm/s

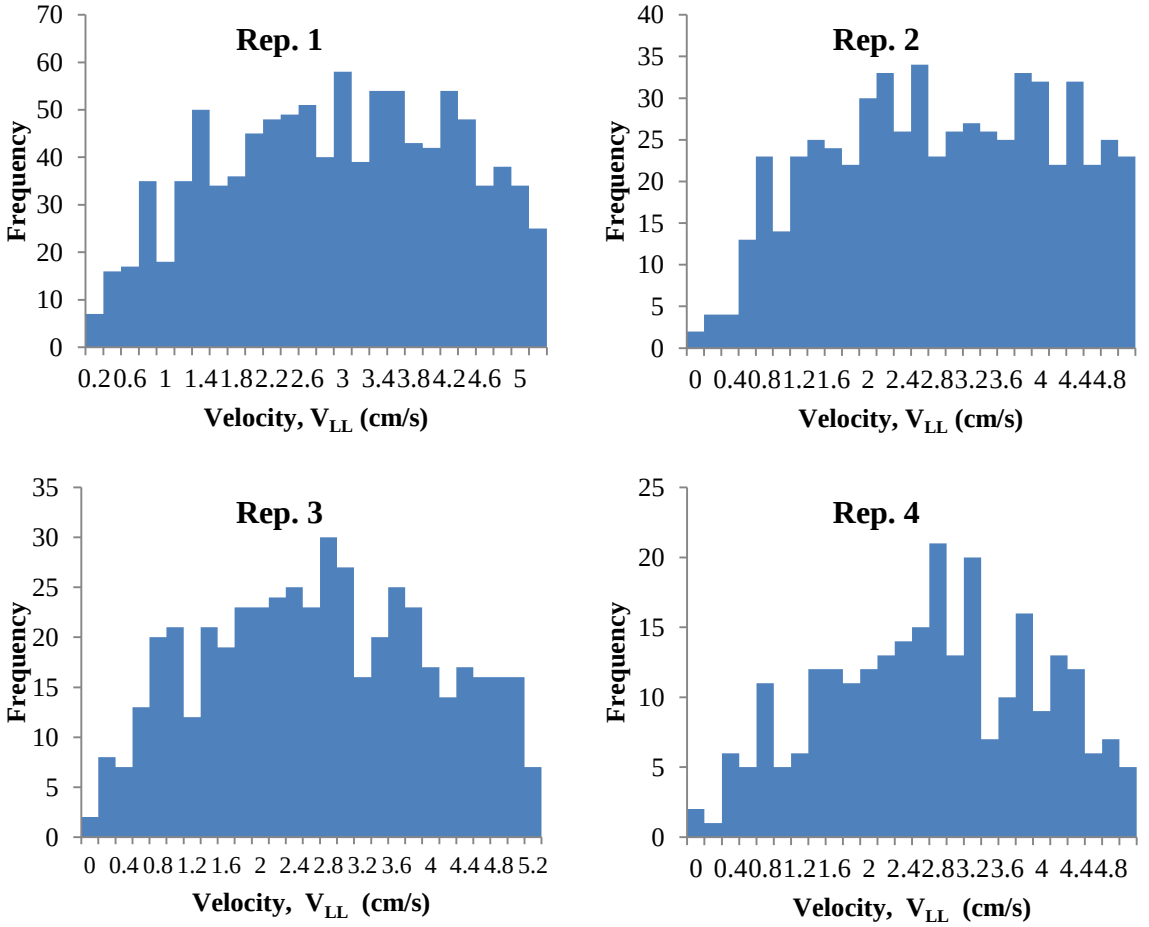

Figure 5.10. Histogram of $V_{LL,}$ in every replication, for V_{SL} = 0.13 ± 2% cm/s

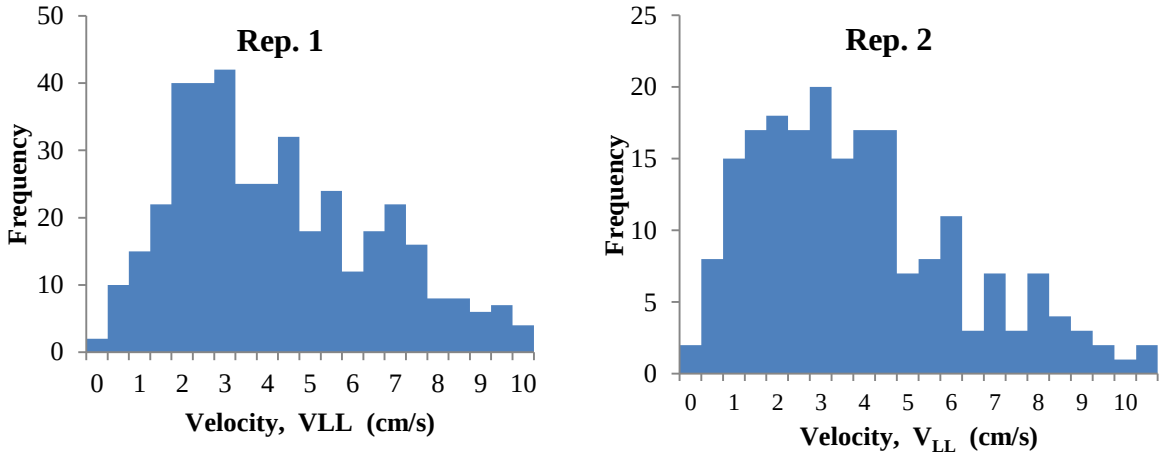

Figure 5.11. Histogram of $V_{LL,}$ in every replication, for V_{SL} = 0.27 ± 2% cm/s

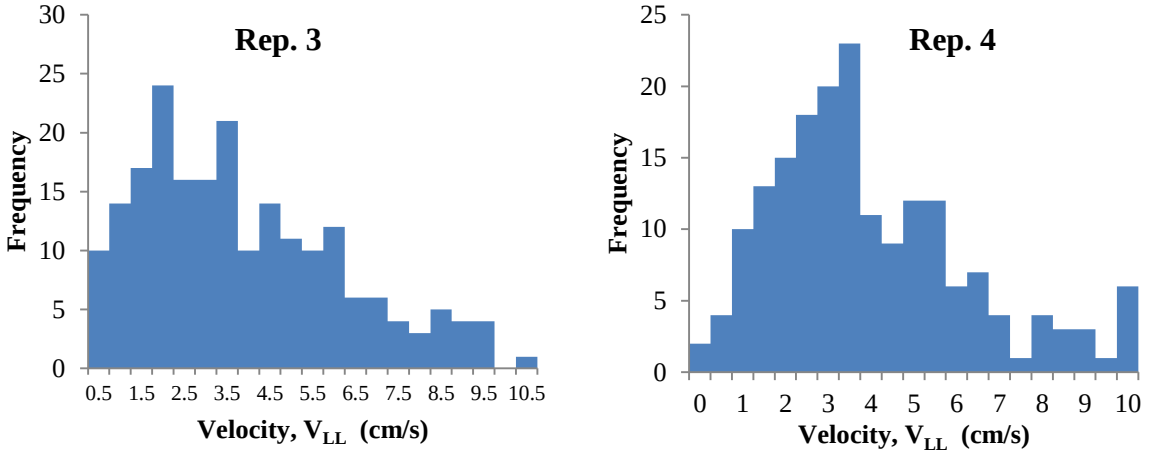

Figure 5.11. Histogram of $V_{LL,}$ in every replication, for V_{SL} = 0.27 ± 2% cm/s (Cont.)

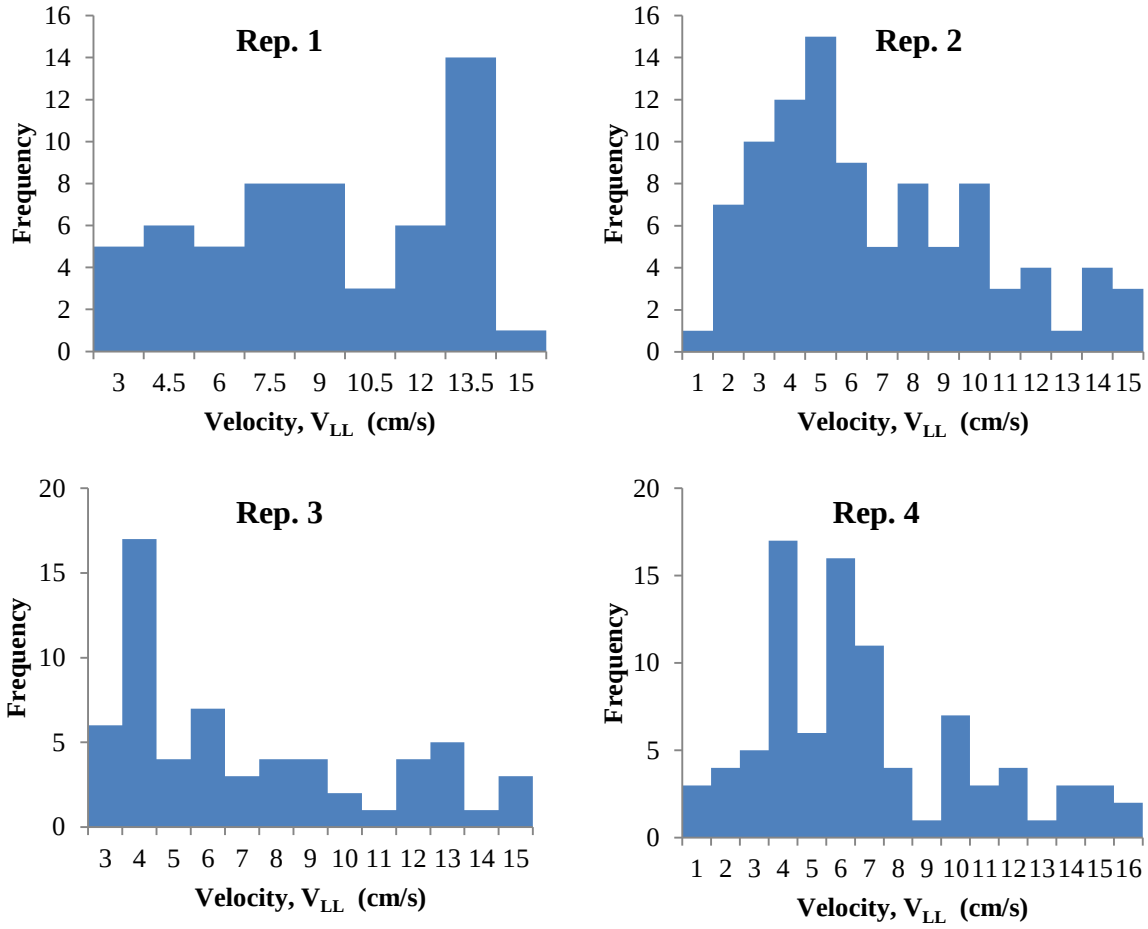

Figure 5.12. Histogram of $V_{LL,}$ in every replication, for V_{SL} = 0.39 ± 2% cm/s

Table 5.2. Maximum measured local liquid velocity ($V_{LL\text{-}Max}$) for a 40 mm diameter tube

Phase	Superficial liquid velocity (± 2% V_{SL}) (cm/s)	Superficial gas velocity (V_{SG}) (± 2% cm/s)	Maximum measured local liquid velocity ($V_{LL\text{-}Max}$) (cm/s)			
			1	2	3	4
Multi	0.13	1.05	5.1	4.9	5	4.8
	0.27		9.1	10.5	10.5	10
	0.39		14.9	14.5	14.2	15.9

The number of particles that were tracked in Sections 5.1.1 and 5.1.2 was not consistent throughout the analysis. This inconsistency caused no repeatable V_{LL} measured in every replication (irreproducibility in getting the same V_{LL} values). The process, however is stochastic, thus it is expected that the local velocity is not going to repeat itself when the measurement is repeated. Hence, statistical analysis based on the mean, variance, and skewness of the histogram distribution should be considered. The inconsistency is primarily attributed to three reasons. The first resulted from the packing randomness each time fresh packing was used; new liquid channels were introduced every time the tube was packed with fresh packing. Secondly, the applied threshold value, highlighted in Section 0, that was either decreased or increased in the analysis procedure to avoid noise coming from the packing, the tube, and the liquid. The threshold value was not constantly applied in all replications, even with the same V_{SL}. Noise or blobs coming from either liquid or packing beads, respectively were visually compared to the I_{diff} image. The third reason is that, as the V_{SL} increased, the tracking particles tended to be pushed away from the region of interest; the tracer particles became fewer as the V_{SL} increased.

Table 5.3 tabulates the mean (over the number of measured velocities), the standard deviation (σ), the variance (σ^2), and the percentage difference (means) for the measured V_{LL} of all replications in each V_{SL} (both 22.5 mm diameter and 40 mm diameter tubes). In both cases, the mean for each V_{LL} increased as the V_{SL} increased; the σ became wider as the V_{SL} increased.

Table 5.3. Mean percent different (from average mean), standard deviation (σ) and variance of histograms for V_{SL} (± 2% cm/s) = 0.13, 0.27, and 0.39 in 40 mm diameter tube and V_{SL} (± 2% cm/s) = 0.42, 0.84 and 1.11 in 22.5 mm diameter tube

Superficial liquid velocity (V_{SL}) [± 2% cm/s]	Measurement 1				Measurement 2				Measurement 3				Measurement 4			
	Mean	$\%_{Diff}$	σ	σ^2	Mean	$\%_{Diff}$	σ	σ^2	Mean	$\%_{Diff}$	σ	σ^2	Mean	$\%_{Diff}$	σ	σ^2
Tube with 40 mm diameter (constant V_{SG} = 1.05 cm/s)																
0.13	2.9	10%	1.3	1.69	2.9	10%	1.3	1.69	2.7	10%	1.3	1.69	2.7	10%	1.2	1.44
0.27	4.0	5%	2.4	5.76	3.9	5%	2.3	5.29	3.9	5%	2.3	5.29	4.0	5%	2.2	4.84
0.39	8.9	73%	3.6	12.96	7.8	38%	3.5	12.25	7.9	28%	3.7	13.69	8.1	8%	3.6	12.96
Tube with 22.5 mm diameter																
0.42	1.2	10%	0.4	0.16	1.1	0%	0.4	0.16	1	10%	0.5	0.25	1.1	0%	0.5	0.25
0.84	2.1	10%	1.2	1.44	1.9	10%	1.3	1.69	1.9	10%	1.2	1.44	2.1	10%	1.1	1.21
1.11	2.7	25%	1.3	1.69	2.3	15%	1.3	1.69	2.4	5%	1.3	1.69	2.4	5%	1.5	2.25

The percent difference for the means show consistent results (10% difference and 5% difference) for V_{SL} of 0.13 ± 2% cm/s and 0.27 ± 2% cm/s which shows repeatability of the measurements. However, there is some evidence to suggest that the experiments can be performed consistently, as indicated by the consistent variances for all V_{SL} replications (both 22.5 mm diameter and 40 mm diameter tubes).

6. CONCLUSIONS AND RECOMMENDATION FOR FUTURE WORK

6.1. CONCLUSIONS

This work, highlighted in Figure 6.1, was designed to introduce a novel technique for Local Liquid Velocity (V_{LL}) measurement in Trickle Bed Reactor (TBR). The novel technique is non-invasive, applicable to trickle bed reactor laboratory scale setup, does not have diffraction and deflection problems, it is comparable to other technique, and has a bigger interrogation size. The proposed new technique, in 2D, which combined Digital Industrial Radiography (DIR) technique and Particle Tracking Velocimetry (PTV) technique, has been successfully:

(a) designed,

(b) evaluated, and

(c) found to be suitable for V_{LL} measurement.

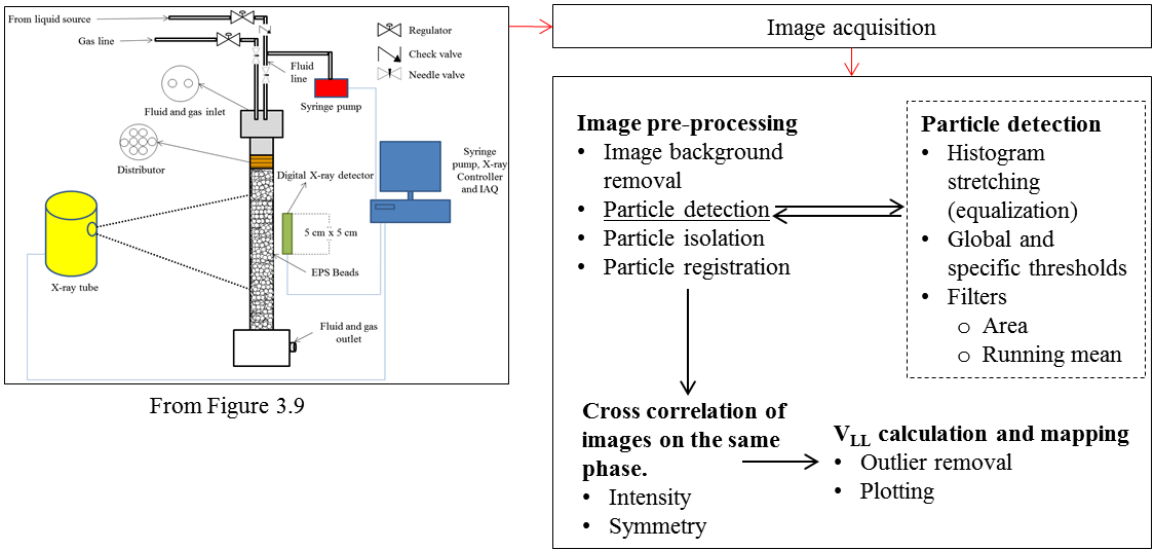

Figure 6.1. Simplified diagram that illustrates the process successfully performed in this work

The proposed research objectives were accomplished by performing experimental investigations on two small beds (22.5 mm and 40 mm diameter) that

were packed with a low density material. Both the accomplishments of the completed work and conclusions drawn from the finding are briefly summarized as follows:

6.1.1. Identification of the Most Suitable Tracking Particles to Be Used For Tracking with A DIR Technique. The tracer particles (material and size) that were used in this work were chosen based on the mass attenuation coefficient of the material and the capability of the Complementary Metal Oxide Semiconductor (CMOS) radiation detector.

The tracer particle is distinguishable from other materials in an X-ray image. A good subject contrast (highlighted in Section 2.1.2) is used to determine the tracer particle material's suitability. Meanwhile, the size of the tracer particle is determined based on the Modulation Transfer Function (MTF) of the complementary metal oxide semiconductor x-ray detector at a particular energy range.

Experiments based on the identified energy range and the measured modulation transfer functions were performed to confirm the identified size range. The identified tracer particles' size range is used throughout the experiment (1.9 refractive index barium titanate [between 106 μm and 125 μm size range]).

6.1.2. Particle Tracking Technique Suitable For the Setup Condition. The particle tracking technique was applied based on the geometrical constraint of the particle (i.e. radial profile).

It was applied based on the Gaussian model of every image, which was detected using the Point Spread Function (PSF) of the seeding particle. The intensity distribution of each particle provided specific point spread function according to the particle's radial symmetry. The particle's central location was localized based on the lattice midpoints of the tracer particle's image. This was validated through series of test which will be highlighted next.

6.1.3. Validating the New Technique Using Experimental Base Approaches. Three types of validation approaches were applied to validate the newly developed technique.

Artificial images containing 20 and 2000 artificial particles of different sizes were used in this experiment. Particles movement occurred in a circular motion. The

newly developed technique successfully identified and tracked each particle's movement.

A syringe pump was set to a specific known velocity (0.06 ± 1% cm/s). A mixture of liquid and tracer particles was injected into a small tube while it was irradiated with X-ray. The newly developed particle identification and particle tracing procedures were applied to measure the local liquid velocity inside the small tube. The proposed procedure produced a difference (either increased or decreased) between the measured velocity and the superficial liquid velocity of at most 16.7% (maximum). Through three replications, the measured velocities were in between 0.048 cm/s and 0.067 cm/s.

The third approach was achieved with a two-point fiber optical probe developed by Abdul Rahman (2014). The newly developed technique and fiber optical probe technique were compared by measuring the local liquid velocity inside the same region of interest. The results were evaluated under the student *t*-test method with *p*-value < 0.05. This evaluation revealed that the measured local liquid velocity that was determined by fiber optical probe ($V_{LL|OPT}$) was in the same group as the measured velocity that was determined by combination of digital industrial radiography and particle tracking velocimetry ($V_{LL|DIR}$). The P values for most cases are found to be more then 0.05. These techniques are found to be complementing each other. The validation procedure proved that the newly developed technique can distinguish, identify, locate, and track the moving seed particles inside the packed bed. Taken together, these findings suggest that the newly developed technique is applicable.

6.1.4. Identifying and Evaluating the Behavior of the Liquid Flow Located Between the Packing Materials. The tracer particles exhibited a specific behavior when they moved in between the packing material.

It indicates that in some parts, the liquid moved with a higher speed. For gas-liquid system, the local liquid velocity can reach up to almost 5 times of its superficial liquid velocity while for gas-liquid-solid system; the local liquid velocity can reach up to nearly 51 times of its superficial liquid velocity. The tracer particle was found to be static in some parts of the bed. The increasing local liquid velocity with respect to the superficial liquid velocity was expected as the liquid was trickling between smaller

spaces (packing porosity). The length travelled by the liquid inside the packed bed was observed to be more than the calculated length given by the tortuosity value (2.07 mm to 2.57 mm). This effect was due to the existence of both Superficial Liquid And Gas Velocities ($V_{S[L\&G]}$).

6.1.5. Evaluating and Comparing the Measured Results With Additional Results Obtained From Published Techniques. This newly developed technique provided velocity values that are consistent with studies conducted by Sankey et al. (2009).

They found that the measured local liquid velocity for a multi-phase trickle bed reactor (liquid-solid-gas) increased ~50 times of superficial liquid velocity and ~5 times of superficial liquid velocity for liquid-solid system. The randomness of the packing structure from every replication suggests no similarity did exist between multiple V_{LL} measurements (as highlighted in Section 5.1.2). Through statistical analysis and experimental observations, these results suggest that such a technique is applicable to trickle bed reactor's local liquid velocity measurements.

Faster, larger digital industrial radiography detector can be utilized. The image resolution however will be lower than that generated by the current detector. This work can contribute to the existing knowledge of trickle bed reactor velocity measurements by providing another optional, non-intrusive method. The increasing local liquid velocity, with respect to superficial liquid velocity, is expected as the liquid trickled between the smaller spaces (packing porosity).

6.2. RECOMMENDATION OF FUTURE WORK: MEASURING THE V_{LL} IN THREE-DIMENSIONAL (3D) ENVIRONMENT

The measurement of V_{LL} can be further investigated in a 3D format by utilizing two sets of X-ray sources as well as DIR detectors.

Figure 6.2 illustrates the recommended experimental setup with two X-ray sources (same exposure parameters) and two DIR detectors. The purple box is the interrogation area. The X-ray beams were directed through the TBRs where the images

of the moving tracer particles were acquired. The identified tracer particles were pointed and registered in detector 1 and detector 2 (P_{R1} and P_{R2}), respectively.

After all of the particles were registered (see Section 0), the implemented identifying algorithm (highlighted in Section 0) was implemented to identify the resembling particles in a subsequent image (Sequence 2). Immediately after each identified particle in P_{R1} was identified, the resembling particle in P_{R2} was tracked according to the shift tolerance threshold.

Figure 6.3 illustrates the recommendation processes that can be applied to identify the matching tracer particles in DIR detector 2. The third tracer particle dimension was identified at this stage. The tolerance should be set according to the principal of the stereoscopic measurement. That is, in the depth of the tracer particle from the DIR detector 2 focal plane (Mrovlje & Vrancic, 2008; Yadav & Mohite-Patil , 2012; Devasenathipathy, et al., 2003; Guezennec, et al., 1994; Adrian, 2005; Nishino, et al., 1989).

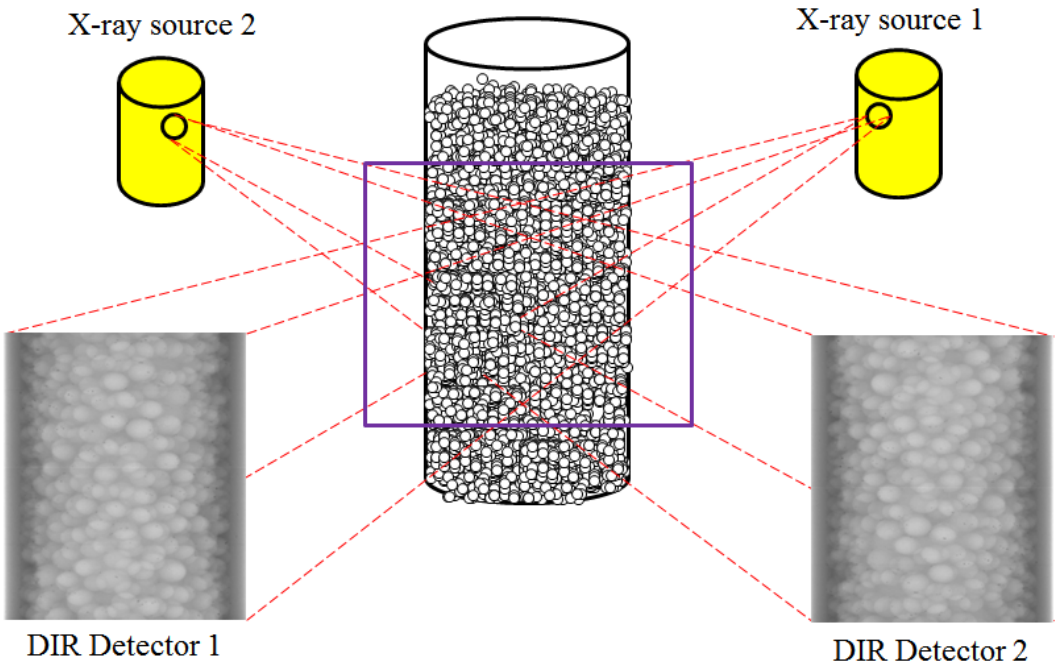

Figure 6.2. Recommended experimental setup with two sources generating and directing the X-rays through the TBRs

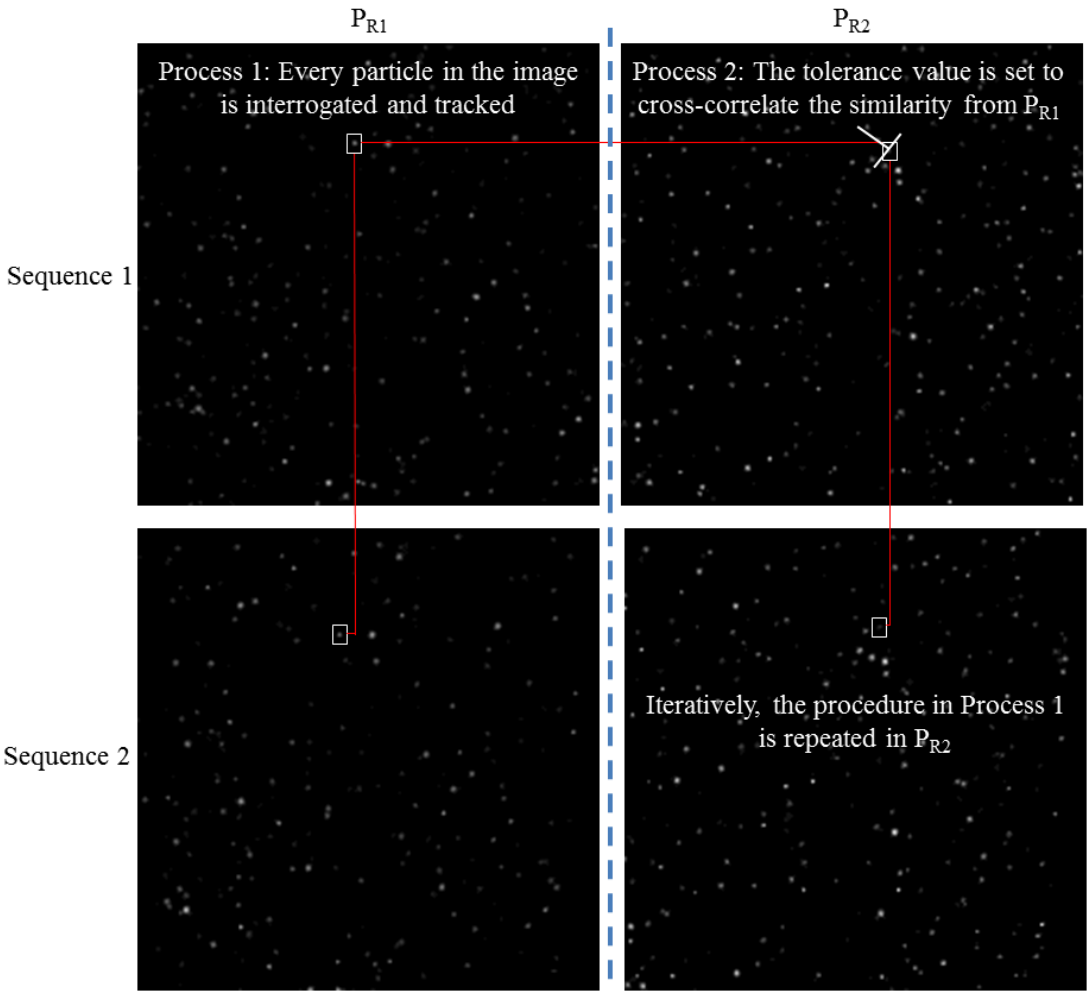

Figure 6.3. Recommended processes for identifying tracer particles in both PR1 and PR2. The tolerance value should be set so that unique matches can be found and matched

The recommended extra procedure is the reconstruction of 2D particle into 3D particle points with a Direct Linear Transform (DLT). This DLT allows for the determination of 3D coordinates of a point by using two or more 2D image views. DIT is also well known for its flexibility in detector set-up (Pourcelot, et al., 2000; Hansen, 1999). This technique has been applied by researchers to study the field flow using conventional PTV technique (Tsao, et al., 1995; Engelmann, et al., 1998). But we are the first to suggest that such an approach be applied to TBRs. Figure 6.4 illustrates the additional procedure (the DLT) that can be incorporated into the previous process and Appendix D explains the procedure in performing it.

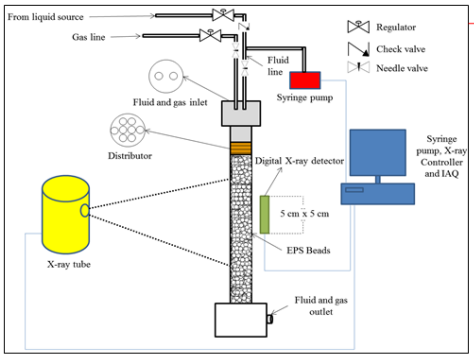

From Figure 3.9

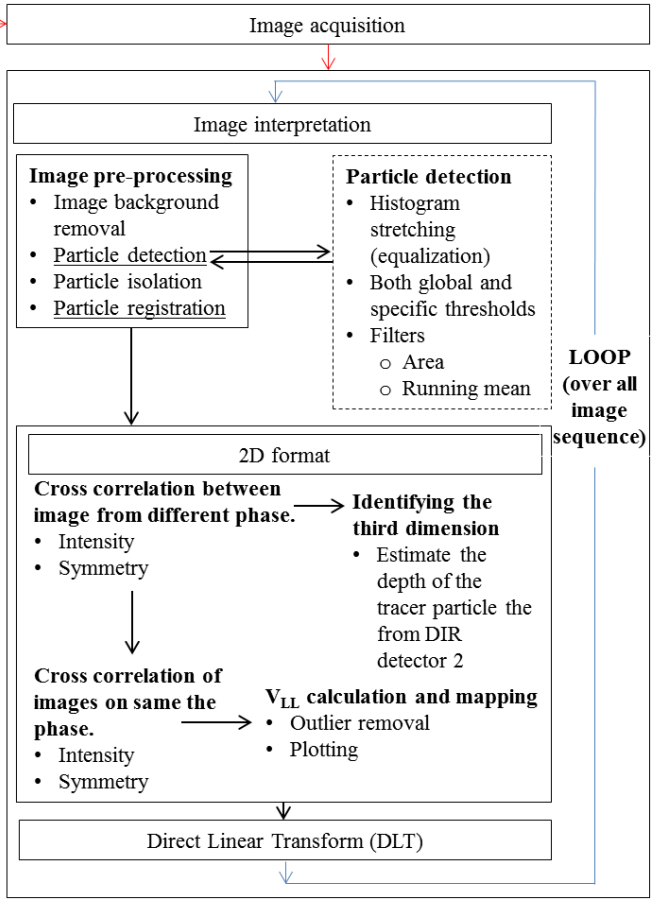

Figure 6.4. Process flow, with an additional procedure, that can be used to create three-dimensional formats

APPENDIX A.

DUPLEX WIRE IMAGE QUALITY INDICATOR (IQI)

10.24.081 EN 462-5 Duplex IQI

For measuring image unsharpness, it is a particularly useful tool for establishing and monitoring the performance of radioscopic (real-time) systems. The proposed CEN standard, prEN 13068 will make its use mandatory in certain cases. The IQI consists of 13 wire pairs embedded in rigid plastic. The wires of platinum and tungsten and are exactly spaced to correspond to the diameter of each pair. The degree of unsharpness is indicated by the number of wire pairs that can be seen. As unsharpness increases, the wires merge to form a single image. Each IQI is engraved with a unique serial number and is supplied with a Declaration of Conformity together with instructions in a storage box.

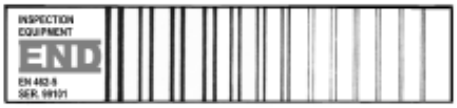

The EN 462-5 model is an exact replacement for the old BS 3971 model IIIA, itself identical to CERL B. This is the only model of duplex IQI in the EN 462 series.

The lead identification reads END (this identification has been submitted to the Technical Committee CEN/TC 138 for approval).

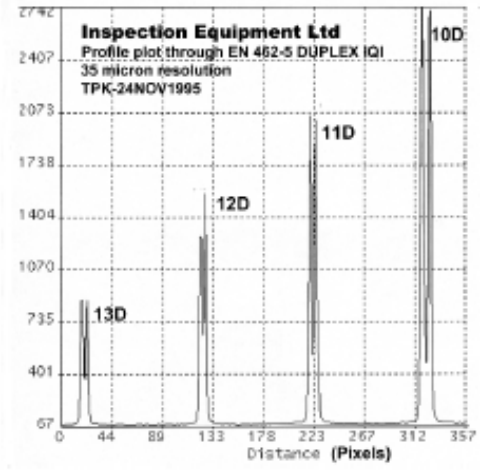

Element No. (D=Duplex)	Corresponding unsharpness	Wire Ø and spacing, mm
13D	0,10	0,050
12D	0,13	0,063
11D	0,16	0,080
10D	0,20	0,100
9D	0,26	0,130
8D	0,32	0,160
7D	0,40	0,200
6D	0,50	0,250
5D	0,64	0,320
4D	0,80	0,400
3D	1,00	0,500
2D	1,26	0,630
1D	1,60	0,800

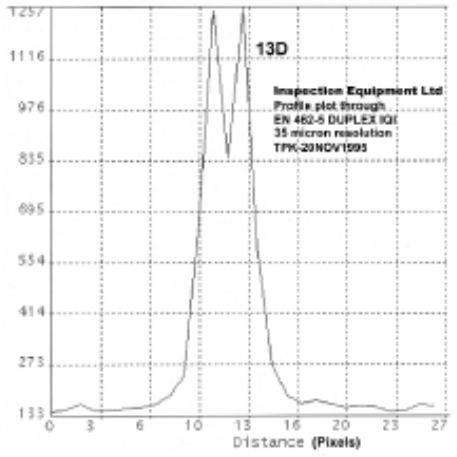

APPENDIX B.

WORKING MATLAB CODE TO PRE-PROCESS THE IMAGE (STATED IN SECTION 2.4.1)

```
%%Written by Khairul Anuar Mohd Salleh. This code is a working example on pre-
processing procedure to eliminate the background (liquid, PVC tube structure
and packed bed) from the tracer particles.

%% Pre-processing (Particle identification) - IMAGE SUBTRACTION & THRESHOLDING

echo off %Display statements during function execution
clc; %Clear Command Window
close all; %Remove all figures
imtool close all;  % Close all imtool figures.
clear all;  % Erase & remove all existing variables workspace (freeing up
system memory)
workspace;  % Make sure the workspace panel is showing.

%% Values for thresholding, CropSize
CropSize = [7.24670571010256 169.167642752562 962.530014641288
487.262079062957];
ThreshValue = 0.001;

%% Read all images
fileFolder = fullfile('GET YOUR FILE');
dirOutput = dir(fullfile(fileFolder,'Image*.tif'));
fileNames = {dirOutput.name}'; % A cell
numFrames = numel(fileNames); % Numbers

K=imread('BackGround.tif');
h = waitbar(0,'Process #1: Creating frame sequence array.  Please wait
Khairul...');
for u=1:numFrames
    outputBaseFileName = sprintf('BG%3.3d.tif', u);
    imwrite(K, outputBaseFileName, 'tif');
    waitbar(u/numFrames)
end
close(h)

dirOutput2 = dir(fullfile(fileFolder,'BG*.tif'));
fileNames2 = {dirOutput2.name}';
numFrames2 = numel(fileNames2);

I = imread(fileNames{1});
L = imread((fileNames2{1}));

% I = im2double(imread(fileNames{1}));
% L = im2double(imread((fileNames2{1})));


%% Preallocate the array
sequence = zeros([size(I) numFrames],class(I));
sequence (:,:,1)= I;
sequence2 = zeros([size(L) numFrames2],class(L));
sequence2(:,:,1) = L;
maxRow=zeros([numFrames 1]);
maxCol=zeros([numFrames 1]);

%% Create image sequence array
h = waitbar(0,'Process #2: Creating frame sequence array.  Please wait
Khairul...');
for p = 1:numFrames
    sequence(:,:,p) = imread(fileNames{p});
    seqcrop(:,:,p) = imcrop(sequence(:,:,p),CropSize);
    seqcroprot(:,:,p) = imrotate(seqcrop(:,:,p),90);
```

```
    waitbar(p/numFrames)
end
close(h)
 %% Substraction technique
h = waitbar(0,'Process #3: Creating background image sequence array.  Please
wait Khairul...');
for n = 1:numFrames2
    sequence2(:,:,n) = imread(fileNames2{n});
    seq2crop(:,:,n) = imcrop(sequence2(:,:,n),CropSize);
    seq2croprot(:,:,n) = imrotate(seq2crop(:,:,n),90);
    waitbar(n/numFrames2)
end
close(h)

C=imsubtract(seq2croprot, seqcroprot);

h = waitbar(0,'Process #4: Saving subtracted images. Please wait Khairul...');
for m=1:numFrames
    outputBaseFileName1 = sprintf('SubtractedImg%3.3d.tif', m);
    imwrite(C(:,:,m), outputBaseFileName1, 'tif');
    waitbar(m/numFrames)
end
close(h);

SampleImg = imread('Image300.tif');
SampleImgCrop = imcrop(SampleImg,CropSize);
SampleImgCropRot = imrotate (SampleImgCrop,90);
figure, imshow(SampleImgCropRot,[]);

SubTimg = imread ('SubtractedImg006.tif');

figure, imshow(SubTimg,[]);

for i=1:numFrames
    img = C(:,:,i);

    % Histogram stretching
    img = uint8(255*double(img)/double(max(img(:))));
    if 0
        while(1)
           [x y] = ginput(1);
           thresh = img(floor(y), floor(x))
           imshow(img>thresh);

           pause;
           imshow(img);
        end;
    else
        thresh1 = 255*graythresh(img(img>0))
        threshOneImg = img>thresh1;

        % Area filter
        labelImg = bwlabel(threshOneImg);
        props = regionprops(labelImg, 'Area');
        threshTwoImg = ismember(labelImg, find([props.Area]>25));

        % Large blob removal from first mask
        threshOneImg = threshOneImg.*~threshTwoImg;

        % Threshold remaining large blobs
```

```
        thresh2 = 120;
        threshTwoImg = img>thresh2;

        % Combine mask
        particleMask = threshOneImg | threshTwoImg;
        %figure, imshow(particleMask);

        % Area box filter
        labelImg = bwlabel(particleMask);
        props = regionprops(labelImg, 'Area');
        particleMask = ismember(labelImg, find([props.Area]<100 &
[props.Area]>5));

        %Saving the subtracted, thresholded & filtered images
        outputBaseFileName = sprintf('SubThresFilt%3.3d.tif', i);
        imwrite(particleMask, outputBaseFileName, 'tif');
        %figure, imshow(particleMask);

        %Make pretty.
        [row, col] = size(img);
        channelStep = row*col;
        idx = find(particleMask);

        visualizeParticles = repmat(img, [1 1 3]);
        visualizeParticles(idx)               = 0;
        visualizeParticles(idx+channelStep)   = 255;
        visualizeParticles(idx+2*channelStep) = 0;
        figure, imshow(visualizeParticles);

    end;
end;

originalImage = im2double(imread('Image300.tif'));
originalImage=imcrop(originalImage,CropSize);
originalImage=imrotate(originalImage,90);

FilteredImg = imread ('SubThresFilt006.tif');

binaryImage=FilteredImg;

labeledImage = bwlabel(binaryImage, 8);
coloredLabels = label2rgb (labeledImage, 'hsv', 'k', 'shuffle');

%---- THIS PART IS OPTIONAL ---- %%

blobMeasurements = regionprops(labeledImage, originalImage, 'all');
numberOfBlobs = size(blobMeasurements, 1);

figure, imshow(originalImage, []);
title(sprintf('Appended identified particles on the original image (Subtracted
& thresholded)'));
hold on;
boundaries = bwboundaries(binaryImage);
numberOfBoundaries = size(boundaries);

for k = 1:numberOfBoundaries
    thisBoundary = boundaries{k};
    plot(thisBoundary(:,2), thisBoundary(:,1), 'g', 'LineWidth', 2);
end
hold off;
```

```
%%
fontSize = 7;
labelShiftX = -7;
blobECD = zeros(1, numberOfBlobs);
fprintf(1,'Blob #      Mean Intensity  Area   Perimeter    Centroid
Diameter\n');
h = waitbar(0,'Process #5: Drawing and labelling the blobs.  Please wait
Khairul...');
for m = 1:numberOfBlobs
    thisBlobsPixels = blobMeasurements(m).PixelIdxList;
    meanGL = mean(originalImage(thisBlobsPixels));
    blobArea = blobMeasurements(m).Area;
    blobPerimeter = blobMeasurements(m).Perimeter;
    blobCentroid = blobMeasurements(m).Centroid;
    blobECD(k) = sqrt(4 * blobArea / pi);
    fprintf(1,'#%2d %17.1f %11.1f %8.1f %8.1f %8.1f % 8.1f\n', m, meanGL,
blobArea, blobPerimeter, blobCentroid, blobECD(m));
    text(blobCentroid(1) + labelShiftX, blobCentroid(2), num2str(m),
'FontSize', fontSize, 'FontWeight', 'Bold');
    waitbar(m/numberOfBlobs)
end
close(h)
```

APPENDIX C.

WORKING MATLAB CODE TO PLOT THE MOVEMENT OF TRACER PARTICLES

```
%%Written by Khairul Anuar Mohd Salleh. This code is a working example how to
plot the %%distance of two tracer particles. The .csv code shall be obtained
from the code which recently published by Parthasarathy (2012).

echo off %Display statements during function execution
clc; %Clear Command Window
close all; %Remove all figures
imtool close all;  % Close all imtool figures.
clear all;  % Erase & remove all existing variables workspace (freeing up
system memory)
workspace;  % Make sure the workspace panel is showing.
dbstop if error

%---- This part will read csv file format (displacment file)----
DataForLine = csvread('.csv generated from the displacement file');
%-----------------------------------------------------------------

%---- This part will form the background to plot the tracked lines
%(optional) ----
CropSize = ['YOUR CROP VALUE']; %Crop value
B = imread('YOUR BACKGROUND IMAGE'); %Image to place the tracked lines
(optional)
B = imcrop(B,CropSize);
B = imrotate (B, YOUR ROTATE VALUE);
B = repmat(B, [YOUR IMAGE ADJUSTMENST VALUE]);
%-------------------------------------------------------------------------

NUM_OF_COLORS = 1024;
myColorMap = colormap(lines(NUM_OF_COLORS));

imtool (B);
figure, imshow(B);

myColorBar = flipud(myColorMap);
myColorBar = reshape(myColorBar, [NUM_OF_COLORS, 1, 3]);
myColorBar = repmat(myColorBar, [1, 32, 1]);

velocities = sqrt(DataForLine(:,3).^2 + DataForLine(:,4).^2);
maxVelocity = sort(velocities, 'descend');
maxVelocity = maxVelocity(1);
scaledVelocityIdx = floor(velocities/maxVelocity*(NUM_OF_COLORS-1))+1;

% Attempt to randomize color selection
idx = randi(numel(scaledVelocityIdx), 1, numel(scaledVelocityIdx));
scaledVelocityIdx = scaledVelocityIdx(idx);

scale = YOUR SCALLING FACTOR; (OPTIONAL)

hold on;
for j=1:size(DataForLine,1)
    x1 = DataForLine(j,1);
    y1 = DataForLine(j,2);
    x2 = x1+scale*DataForLine(j,3);
    y2 = y1+scale*DataForLine(j,4);

     line([x1 x2], ...
         [y1 y2], ...
         'Color', myColorMap(scaledVelocityIdx(j),:));
end
hold off;
axis equal;
```

APPENDIX D.

PERFORMING THREE DIMENSIONAL (3D) LOCAL LIQUID VELOCITY (V_{LL}) MEASUREMENT USING DIGITAL INDUSTRIAL RADIOGRAPHY (DIR) AND PARTICLE TRACKING VELOCIMETRY (PTV) TECHNIQUES

D.1. Introduction

In this work, combined techniques namely Digital Industrial Radiography (DIR) and Particle Tracking Velocimetry (PTV) will be used to obtain a Three Dimensional (3D) Local Liquid Velocity (VLL) measurement. The following section outlines the sequence of operation as well as the technical information for such measurement.

D.2. Tracer particles

- Tracer particles' materials are identified through mass attenuation coefficient of components used.
    - Good radiographic contrast of the tracer particle should be obtained from the image (see Section 2.1.2).
- Tracer particles' size is identified using the spatial resolution test of the X-ray digital detector (see Section 3.2.1).
    - Higher X-ray detector's spatial resolution will distinguish smaller size tracer particle
- The identified tracer particles' size and material should then be confirmed through experiments (as in Section 3.2.2), Stokes number and available literatures.

D.3. Digital Industrial X-ray Radiography (DIR) setup

- The setup, shown in Figure 3.9, is extended to the suggested setup shown in Figure 6.2.
- Both X-ray sources and detectors are aligned with 90^{o} offset
- Table D1 lists the suggestion of specification for both X-ray and detector that is most suitable to be used in the future.

D.4. Particle tracer identification

- Separate the tracer particle identification from both detectors.
- Perform the pre-processing (highlighted in Section Figure 2.4) on the images.
- Identify the particle in both images from P_{R1} and P_{R2}.
- Any resemblance between the particle in P_{R1} and P_{R2} is identified according the shift tolerance threshold.
- The shift tolerance threshold is set according to the principal of the stereoscopic measurement.

- The identified tracer particle from Detector 2 will be the depth (z-component) of the particle.

D.5. Mixture of tracer particle inside the syringe

- The mixture of the liquid-tracer particles are inserted into the syringe.
- The syringe is fixed into the syringe pump and is set to facing downward to avoid clogging.

Table D1. Suggested specification for both X-ray source and X-ray detector

X-ray (unipolar type)	
Penetrating energy (kVp)	160 or 220
Applicable current (mA)	3-5
Beam type	Directional
Detector	
Semiconductor type	Complementary metal oxide semi-conductor (CMOS)
Pixel pitch (μm)	50 or less
Frame rate (fps)	3 or less

BIBLIOGRAPHY

1. Abdul Rahman, M. F., 2014. *Hydrodynamic study of trickle bed reactor,* PhD Dissertation. Rolla: Missouri University of Science and Technology.

2. Adrian, R. J., 1991. Particle-Imaging Techniques for Experimental Fluid Mechanics. *Annu. Rev. Fluid Mech,* Volume 23, pp. 261-304.

3. Adrian, R. J., 2005. Twenty years of particle image velocimetry. *Experiments in Fluids,* Volume 39, pp. 159-169.

4. Aguet, F., Van De Ville, D. & Unser, M., 2005. A maximum-likelihood formalism for sub-resolution axial localization of fluorescent nanoparticles. *Optics Express,* 13(26), pp. 10503 - 10522.

5. Ahmed, S. N., 2007. *Physics and Engineering of Radiation Detection.* London: Elsevier.

6. Albright, S. C., Winston, W. L. & Zappe, C., 2006. *Data analysis and decision making.* 3rd ed. Mason: Thomson Higher Education.

7. Al-Dahhan, M. H., 1993. *Effects Of High Pressure And Fines On The Hydrodynamics Of Trickle-Bed Reactors,* PhD Dissertation. St. Louis: Washington University in St. Louis.

8. Al-Dahhan, M. H. & Dudukovic, M. P., 1995. Catalyst wetting efficiency in trickle bed reactors at high pressure. *Chemical Engineering Science,* 50(15), pp. 2377-2389.

9. Al-Dahhan, M. H., Larachi, F., Dudukovic, M. P. & Laurent, A., 1997. High-Pressure Trickle-Bed Reactors: A Review. *Ind. Eng. Chem. Res.,* Volume 36, pp. 3292-3314.

10. Alekseychuk, A., 2006. *Detection of crack-like indications in digital radiography by global optimisation of probabilistic estimations function,* Dresden: Technische Universitat Dresden.

11. Al-Naimi, S. A., Al-Sudani, F. T. J. & Halabia, E. K., 2011. Hydrodynamics and flow regime transition study of trickle bed reactor at elevated temperature and pressure. *Chemical Engineering Research and Design,* Volume 89, pp. 930-939.

12. American Society for Metals, 1997. *Nondestructive evaluation and quality control.* s.l.:ASM International.

13. Basavaraj, M. G., Gupta, G. S. & Naveen, K., 2005. Local Liquid Holdups and Hysteresis in a 2-D Packed Bed Using X-ray Radiography. *Particle Technology and Fluidization,* 51(8), pp. 2178-2189.

14. Boslaugh, S., 2012. *Statistics in a Nutshell.* 2nd ed. s.l.:O'Reilly Media.

15. Boudreau, B. P., 1996. The diffusive tortuosity of fine-grained unlithified sediments. *Geochimica et Cosmochimica Acta,* 60(16), pp. 3139-3142.

16. Boyer, C. & Fanget, B., 2002. Measurement of liquid flow distribution in trickle bed reactor of large diameter with a new gamma-ray tomographic system. *Chemical Engineering Science,* Volume 57, p. 1079–1089.

17. Boyer, C., Volpi, C. & Ferschneider, G., 2007. Hydrodynamics of trickle bed reactors at high pressure: Two-phase flow model for pressure drop and liquid holdup, formulation and experimental validation. *Chemical Engineering Science,* Issue 62, p. 7026 – 7032.

18. Brady, M. R., 2006. *Subpixel Resolution Schemes for Multiphase Flow.* MS Thesis, Blacksburg: Virginia Polytechnic Institute and State University.

19. Brevis, W., Nino, Y. & Jirka, G. H., 2011. Integrating cross-correlation and relaxation algorithms for particle tracking velocimetry. *Exp Fluids,* Volume 50, pp. 135-147.

20. Bushberg, J. T., Seibert, J. A., Leidholdt, E. M. & Boone, J. M., 1994. *The Essential Physics of Medical Imaging.* Baltimore: Williams and Wilkins.

21. Cabral, T. M. & Rangayyan, R. M., 2012. *Fractal Analysis of Breast Masses in Mammograms.* s.l.:Morgan & Claypool Publishers.

22. Chaouki, J., Larachi, F. & Dudukovic, M. P., 1997. Noninvasive Tomographic and Velocimetric Monitoring of Multiphase Flows. *Ind. Eng. Chem. Res.*, Issue 36, pp. 4476-4503.

23. Comiti, J. & Renaud, M., 1989. A new model for determining mean structure parameters of fixed beds from pressure drop measurements: Application to beds packed with parallelepipedal particles. *Chemical Engineering Science,* 44(7), pp. 1539-1545.

24. Cowen, A. R., 1991. Digital X-ray imaging. *Meas. Sci. Tehnol.,* Volume 2, pp. 691-707.

25. Cushman, J. H. & Moroni, M., 2001. Statistical mechanics with three-dimensional particle tracking velocimetry experiments in the study of anomalous dispersion. I. Theory. *Physics of Fluid,* 13(1), pp. 75-80.

26. Dainty, J. C. & Shaw, R., 1974. *Image Science.* London: Academic Press.

27. Delgado, J. P., 2006. A Simple Experimental Technique to Measure Tortuosity in Packed Beds. *The Canadian Journal of Chemical Engineering,* 84(6), pp. 651-655.

28. Devasenathipathy, S., Santiago, J. G., Wereley, S. T. & Meinhart, C. D., 2003. Particle imaging techniques for microfabricated fluidic systems. *Experiments in Fluids,* Volume 34, pp. 504-514.

29. Dobbins III, J. T., 2000. Image Quality Metrics for Digital Systems. In: J. Beutel, H. L. Kundel & R. L. Van Metter, eds. *Handbook of Medical Imaging.* Bellingham: SPIE Press, pp. 163-219.

30. Dudukovic, M., 2000. Opaque Multiphase Reactors: Experimentation, Modeling and Troubleshooting. *Oil & Gas Science and Technology - Rev. IFP,* 55(2), pp. 135-158.

31. Dudukovic, M. P., Larachi, F. & Mills, P. L., 1999. Multiphase reactors - revisited. *Chemical Engineering Science,* Volume 54, pp. 1975-1995.

32. Elkins, C. J. & Alley, M. T., 2007. Magnetic resonance velocimetry: applications of magnetic resonance imaging in the measurement of fluid motion. *Exp Fluids,* Volume 43, pp. 823-858.

33. Engelmann, D. et al., 1998. *Stereo particle tracking.* Sorrento, Springer Link, pp. 240.1 - 240.10.

34. Ewert, U., Zscherpel, U. & Bavendiek, K., 2004. *Film replacement by digital X-ray detectors - the correct procedure and equipment.* Montreal.

35. Germain, A. H., Lefebvre, A. G. & L'homme, G. A., 1974. Experimental Study of a Catalytic Trickle Bed Reactor. *Adv. Chem. Ser.,* Volume 133, pp. 164-180.

36. Gonzalez, R. C. & Woods, R. E., 2002. *Digital Image Processing.* 2nd ed. New Jersey: Prentice-Hall.

37. Guezennec, Y. G., Brodkey, R. S., Trigui, N. & Kent, J. C., 1994. Algorithms for fullyautomated three-dimensional particle tracking velocimetry. *Experiments in Fluids,* Volume 17, pp. 209-219.

38. Halmshaw, R., 1991. *Non-Destructive Testing.* London: Edward Arnold.

39. Hansen, J. F., 1999. *On Chromatic and Geometrical Calibration,* Lyngby.

40. Hassan, Y. A., Blanchet, T. K. & Seeley Jr, C. H., 1992. PIV flow visualization using particle tracking techniques. *Meas. Sci. Technol.,* Volume 3, pp. 633-642.

41. Hassan, Y. A. & Ontiveros, E. D., 2008. Flow visualization in a pebble bed reactor experiment using PIV and refractive index matching techniques. *Nuclear Engineering and Design,* Issue 238, pp. 3080-3085.

42. Heindel, T. J., 2011. A Review of X-ray Flow Visualization With Applications to Multiphase Flows. *Journal of Fluids Engineering,* July.Volume 133.

43. Huang, A. Y. L., Huang, M. Y. F., Capart, H. & Chen, R.-H., 2008. Optical measurements of pore geometry and fluid velocity in a bed of irregularly packed spheres. *Exp Fluids,* Volume 45, pp. 309-321.

44. Jaffe, S. B., 1976. Hot Spot Simulation in Commercial Hydrogenation Processes. *Ind. Eng. Chem. Process Des. Dev.,* 15(3), pp. 410-416.

45. Johnston, W. & Dybbs, A., 1975. Measurement of fluid velocity inside porous media with a laser anemometer. *Physics of Fluid,* 18(7), pp. 913-914.

46. Kagumba, M. O. O., 2013. *Heat Transfer and Bubble Dynamics In Bubble And Slurry Bubble Columns With Internals For Fischer-Tropsch Synthesis Of Clean Alternative Fuels And Chemicals,* Rolla: Missouri University of Science and Technology.

47. Kantzas, A., 1994. Computation of holdups in fluidized and trickle beds by computer-assisted tomography. *AIChE,* 40(7), pp. 1254-1261.

48. Kertzscher, U., Seeger, A., Affeld, K. & Goubergrits, L., 2004. X-ray based particle tracking velocimetry - a measurement technique for multi phase flows and flows without optical access. *Flow Measurement and Instrumentation,* Volume 15, pp. 199-206.

49. Lanfrey, P. -Y., Kuzeljevic, Z. V. & Dudukovic, M. P., 2010. Tortuosity model for fixed beds randomly packed with identical particles. *Chemical Engineering Science,* Volume 65, pp. 1891-1896.

50. Lee, J.-Y. & Lee, S.-Y., 2009. Flow Visualization in the Scaled Up Pebble Bed of High Temperature Gas-Cooled Reactor Using Particle Image Velocimetry Method. *Engineering for Gas Turbines and Power,* 131(6), pp. 1-4.

51. Lee, S. J. & Kim, G. B., 2003. X-ray particle image velocimetry for measuring quantitative flow information inside opaque objects. 94(5).

52. Lee, S. J. & Kim, G. B., 2003. X-ray particle image velocimetry for measuring quantitative flow information inside opaque objects. *Journal of Applied Physics,* 1 September.94(5).

53. Liu, C. & Tao, L., 2007. Two-Dimensional Digital Particle Tracking Velocimetry Algorithm Based on the Image of Particle Trace. *Journal of Coastal Research,* Volume 50, pp. 415-419.

54. Lutran, P. G., Ng, K. M. & Delikat, E. P., 1991. Liquid Distribution in Trickle Beds. An Experimental Study Using Computer-Assisted Tomography. *Ind. Eng. Chem. Res,* 30(6), pp. 1270-1280.

55. Magaud, F., Souhar, M., Wild, G. & Boisson, N., 2001. Experimental study of bubble column hydrodynamics. *Chemical Engineering Science,* Volume 56, pp. 4597-4607.

56. Ma, H., Long, F., Zeng, S. & Huang, Z.-L., 2012. Fast and precise algorithm based on maximum radial symmetry for single molecule localization. *Optics Letters,* 37(13), pp. 2481-2483.

57. Marcandelli, C., Wild, G., Lamine, A. S. & Bernard, J. R., 1999. Measurement of local particle-fluid heat transfer coefficient in trickle-bed reactors. *Chemical Engineering Science,* Volume 54, pp. 4997-5002.

58. Meitzner, C., 2011. *Investigation of structured solid bed catalysts,* Dresden: TU Dresden.

59. Merwe, v. d. W., Nicol, W. & Beer, d. F., 2007. Trickle flow distribution and stability by X-ray radiography. *Chemical Engineering Journal,* August , Volume 132, pp. 47-59.

60. Merwe, v. d. W., Nicol, W. & Beer, d. F., 2007. Trickle flow distribution and stability by X-ray radiography. *Chemical Engineering Journal,* August , Volume 132, pp. 47-59.

61. Moroni, M. & Cushman, J. H., 2001. Statistical mechanics with three-dimensional particle tracking velocimetry experiments in the study of anomalous dispersion. II. Experiments. *Phys. Fluids,* 13(1), pp. 81-91.

62. Mota, M., Teixeira, J. A. & Yelshin, A., 1998. *Tortuosity in Bioseparations and its Application to Food Processes.* Porto, Bioprocesses for Food Production, pp. 93-98.

63. Mrovlje, J. & Vrancic, D., 2008. *Distance measuring based on stereoscopic pictures.* Ljubljana.

64. Narasimhan, C. S. L., Verma, R. P., Kundu, A. & Nigam, K. D. P., 2002. Modeling Hydrodynamics of Trickle-Bed Reactors at High Pressure. *AIChE Journal,* 48(11), pp. 2459 - 2474.

65. Nishino, K., Kasagi, N. & Hirata, M., 1989. Three-Dimensional Particle Tracking Velocimetry Based on Automated Digital Image Processing. *Journal of Fluids Engineering,* 111(4), pp. 384-391.

66. NIST, 2011. *Element/Compound/Mixture Selection.* [Online] Available at: http://physics.nist.gov/PhysRefData/Xcom/html/xcom1-t.html [Accessed 23 August 2013].

67. Northrup, M. A., Kulp, T. J. & Angel, S. M., 1993. Direct measurement of interstitial velocity field variations in a porous medium using fluorescent-particle image velocimetry. *Chemical Engineering Science,* 48(1), pp. 13-21.

68. Ohmi, K. & Li, H.-Y., 2000. Particle-tracking velocimetry with new algorithms. *Meas. Sci. Technol.,* Volume 11, pp. 603-616.

69. Ohmi, K. & Li, H.-Y., 2000. Particle-tracking velocimetry with new algorithms. *Meas. Sci. Technol.,* Volume 11, pp. 603-616.

70. Park, J.-K.et al., 2004. *High-Resolution Phosphors as X-ray Detectors for Synchrotron Radiation Experiments.* s.l., pp. 4690-4694.

71. Park, W. H., Kang, W. K., Capes, C. E. & Osberg, G. L., 1969. The properties of bubbles in fluidized beds of conducting particles as measured by an electroresistivity probe. *Chemical Engineering Science,* 24(5), pp. 851-865.

72. Parthasarathy, R., 2012. Rapid, accurate particle tracking by calculation of radial symmetry centers. *Nature Methods,* Volume 9, pp. 724-726.

73. Peurrung, L. M., Rashidi, M. & Kulp, T. J., 1995. Measurement of porous medium velocity fields and their volumetric averaging characterisitics using particle tracking velocimetry. *Chemical Engineering Science,* 50(14), pp. 2243-2253.

74. Pourcelot, P., Audigie, F., Degueurce, C. & Geiger, D., 2000. A method to synchronise cameras using the direct linear transformation technique. *Journal of Biomechanics,* Volume 33, pp. 1751-1754.

75. Prasad, A. K., 2000. Particle image velocimetry. *Current Science,* 10 July, 79(1), pp. 51-60.

76. Pratt, W. K., 1991. *Digital Image Processing.* 2nd ed. s.l.:John, Wiley and Sons.

77. Pushnov, A. S., 2006. Calculation of Average Bed Porosity. *Chemical and Petroleum Engineering,* Volume 42, pp. 14-17.

78. Rigby, G. R., van Blockland, G. P., Park, W. H. & Capes, C. E., 1970. Properties of bubbles in three phase fluidized beds as measured by an electroresistivity probe. *Chemical Engineering Science,* 25(11), pp. 1729-1741.

79. Rowlands, J. A. & Yorkston, J., 2000. Flat panel detectors for digital radiography. In: J. Beutel, H. L. Kundel & R. L. Van Metter, eds. *Handbook of Medical Imaging - Volume 1. Physics and Psychophysics.* Bellingham: SPIE Press, pp. 225-313.

80. Russ, J. C., 2002. *Image Processing Handbook.* 4th ed. Florida: CRC Press.

81. Saleh, S., Thovert, J. F. & Adler, P. M., 1992. Measurement of two-dimensional velocity fields in porous media by particle image displacement velocimetry. *Experiments in Fluids,* Volume 12, pp. 210-212.

82. Samei, E., 2008. *Application of the ILO International Classification of Radiographs of Pneumoconioses to Digital Chest Radiographic Images.* [Online]
Available at: http://www.cdc.gov/niosh/docs/2008-139/manuscript-samei-acquisition.html
[Accessed 8 January 2013].

83. Sankey, M. H., Holland, D. J., Sederman, A. J. & Gladden, L. F., 2009. Magnetic resonance velocity imaging of liquid and gas two-phase flow in packed beds. *Magnetic Resonance,* Volume 196, pp. 142-148.

84. Satterfield, C. N., 1975. Trickle-Bed Reactors. *AIChE,* 21(2), pp. 209-228.

85. Schubert, M., Khetan, A., da Silva, M. J. & Kryk, H., 2010. Spatially resolved inline measurement of liquid velocity in trickle bed reactors. *Chemical Engineering Journal,* Issue 158, p. 623–632.

86. Schurbet, M., Hessel, G., Zippe, C. & Lange, R., 2008. Liquid flow texture analysis in trickle bed reactors using high-resolution gamma ray tomography. *Chemical Engineering Journal,* Volume 140, p. 332–340.

87. Sederman, A. J. & Gladden, L. F., 2001. Magnetic resonance imaging as a quantitative probe of gas-liquid distribution and wetting efficiency in trickle-bed reactors. *Chemical Engineering Science,* Issue 56, pp. 2615-2628.

88. Sederman, A. J. & Gladden, L. F., 2001. Magnetic resonance visualisation of single- and two-phase flow in porous media. *Magnetic Resonance Imaging,* Volume 19, pp. 339-343.

89. Seeger, A., Affeld, K., Goubergrits, L. & Kertzscher, U., 2001. X-ray-based assessment of the three-dimensional velocity of the liquid phase in a bubble column. *Experiments in Fluids,* Issue 31, pp. 193-201.

90. Seeger, A., Kertzscher, U., Affeld, K. & Wellnhofer, E., 2003. Measurement of the local velocity of the solid phase and the local solid hold-up in a three-phase flow by X-ray based particle tracking velocimetry (XPTV). *Chemical Engineering Science,* Issue 58, p. 1721 – 1729.

91. Shultis, J. K. & Faw, R. E., 2002. *Fundamentals of Nuclear Science And Engineering.* New York: Marcel Dekker.

92. Siemens, 2013. *Simulation of X-ray Spectra.* [Online] Available at: https://w9.siemens.com/cms/oemproducts/Home/X-rayToolbox/Pages/X-rayToolbox.aspx [Accessed 8 August 2013].

93. Sie, S. T. & Krishna, R., 1998. Process development and scale up: III. Scale-up and scale-down of trickle bed processes. *Reviews in Chemical Engineering,* 14(3), pp. 203-252.

94. Sinha, V., Srivastava, A., Lee, H. K. & Liu, X., 2013. *Performance Evaluation of a Combined Neutron and X-ray Digital Imaging System.* San Diego, Proc. SPIE 8694.

95. Solomon, C. & Breckon, T., 2011. *Fundamentals of Digital Image Processing: A Practical Approach with Examples in Matlab.* Noida: John Wiley & Sons, Ltd.

96. Tapia, H. S., Aragon, J. A. G., Hernandez, D. M. & Garcia, B. B., 2006. *Particle Tracking Velocimetry (PTV) Algorithm for Non-uniform and Nonspherical particles.* Cuernavaca, IEEE, pp. 325-330.

97. Teledyne Rad-icon Imaging Corp, 2013. *Shad-o-Box™ X-Ray Cameras.* [Online]
Available at: http://www.rad-icon.com/pdf/Shad-o-Box%20Datasheet.pdf [Accessed 7 July 2013].

98. Theunissen, R., 2003. *Improvements in Hybrid PIV/PTV algorithms and droplet sizing,* Delft: TU Delft.

99. Tsao, R., Giddens, D. P., Jones, S. A. & Zarins, C. K., 1995. An Automated Three-Dimensional Particle Tracking Technique for the Study of Modeled Arterial Flow Fields. *Journal of Biomechanical Engineering,* Volume 117, pp. 211-218.

100. Tsoulfanidis, N., 1995. *Measurement and detection of radiation.* Washington, DC: Taylor & Francis.

101. Wangjiraniran, W. et al., 2003. Intrusive Effect of Wire Mesh Tomography on Gas–liquid Flow Measurement. *Journal of Nuclear Science and Techbology,* 40(11), pp. 932-940.

102. Westerweel, J., 1993. *Digital Particle Image Velocimetry - Theory and Application,* Delft: Delft University Press.

103. Wilcox, R. R., 2012. *Introduction to Robust Estimation and Hypothesis Testing.* 3rd ed. s.l.:Academic Press.

104. Wolbrast, A. B., 2005. *Physics of Radiology.* 2nd ed. Madison: Medical Physics Publishing.

105. Wu, Q. & Ishii, M., 1999. Sensitivity study on double-sensor conductivity probe for the measurement of interfacial area concentration in bubbly flow. *International Journal of Multiphase Flow,* Volume 25, pp. 155-173.

106. Xue, J., 2004. *Bubble velocity, size and interfacial area measurements in bubble columns,* Saint Louis: Washington University in St. Louis.

107. Xue, J., Al-Dahhan, M., Dudukovic, M. P. & Mudde, R. F., 2008. Four-point optical probe for measurement of bubble dynamics: Validation of the technique. *Flow Measurement and Instrumentation,* Volume 19, pp. 293-300.

108. Yadav, A. & Mohite-Patil , T. B., 2012. Distance Measurement with Active & Passive Method. *International Journal of Computer Science and Network ,* 1(4), pp. 6-9.

109. Yaffe, M. J. & Rowlands, J. A., 1997. X-ray detectors for digital radiography. *Phys. Med. Biol.,* Volume 42, pp. 1-39.

110. Yagi, N., Yamamoto, M., Uesugi, K. & Inoue, K., 2004. *CMOS Imaging Detectors as X-ray Detectors for Synchrotron Radiation Experiments*. San Francisco, American Institute of Physics, pp. 885-888.

111. Yamada, H., Naruse, T. & Goto, S., 1999. Trickle bed reactor diluted with one particles and coiled tubular flow-type reactor for kinetic measurements without external effects. *Catalysis Today,* Volume 48, pp. 301-306.

112. Yin, F., Afacan, A., Nandakumar, K. & Chuang, K. T., 2002. Liquid holdup distribution in packed columns: gamma ray tomography and CFD simulation. *Chemical Engineering and Processing,* Volume 41, pp. 473-483.

VITA

Khairul Anuar B. Mohd Salleh was born in Johor, Malaysia. He grew up in Pontian, Johor and went to Sekolah Menengah Datuk Penggawa Barat (SDPB), Pontian where he graduated from high school in 1995. He was enrolled in the science matriculation program in Sekolah Menengah Sains Muar (SMS Muar) between 1996 and 1998. Between 1998 and 2001, he studied physics with electronics (BSc with Honors) at the Universiti Malaysia Sabah (UMS) in Kota Kinabalu, Malaysia.

Khairul Anuar became an intern in Flextronics Malaysia Sdn. Bhd. (Senai) and was later hired as a test engineer at the Venture Mfg. Sdn. Bhd. in Kempas, Johor. In 2002, he joined the Malaysian civil service as a researcher in the Malaysian Nuclear Agency. While there, he became a member of the Non-Destructive Testing (NDT) group. He is also a qualified Radiation Protection Officer (RPO), a radiographer (Level III), and an Eddy Current technique (Level II) operator and instructor. In 2009, he obtained his masters degree in physics (MSc) from the Universiti Teknologi Malaysia (UTM) in Skudai, Johor.

Khairul Anuar joined the Missouri University of Science and Technology (Missouri S&T) in 2011. During this time, he worked as a graduate assistant in Radiation Measurement & Spectroscopy Laboratory.

He defended his research on March 19th, 2014. He was awarded a PhD in Nuclear Engineering during the summer 2014. His dissertation established a novel technique in measuring local liquid velocity in trickle bed reactor by combining X-ray digital industrial radiography and particle tracking techniques.

While at Missouri S&T, Khairul Anuar published two peer-reviewed article in the *Institute of Physics (IOP)* and the *American Institute of Physcis (AIP)*. He has also submitted three more manuscripts for peer-review. He also presented his work at two conferences, the 2013 American Nuclear Society (ANS) Winter Meeting and Nuclear Technology Expo (Washington D.C.) and the 2013 American Institute of Chemical Engineers (AIChE) Annual Meeting (San Francisco).